



Master's Thesis

GUOZHEN MA

A Complete CENSUS of Quasars

Cosmic Dawn Center

Niels Bohr Institute

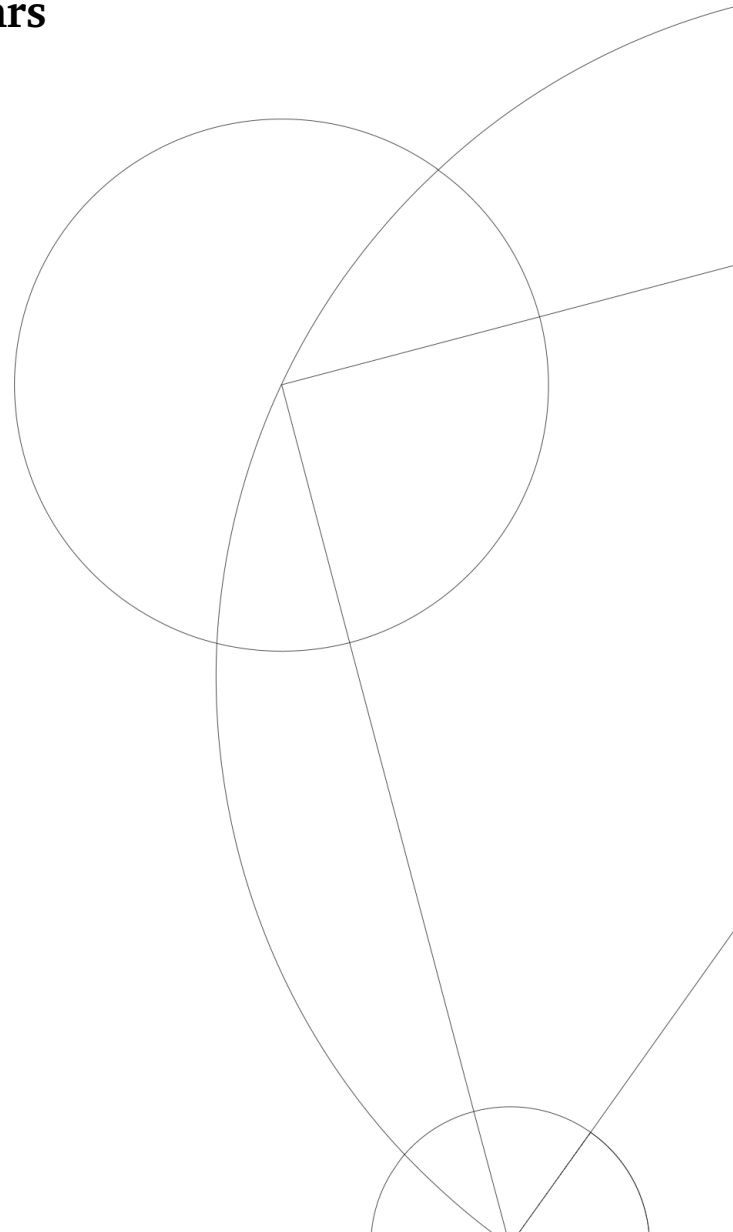
University of Copenhagen

Supervisor:

Johan Peter Uldall Fynbo

Handed in on:

20-05-2022



Abstract

The investigations of quasi-stellar objects (quasars) have suffered from selection effects of different color criteria for a long time, due to the limited samples to produce color criteria and inevitable imprecision caused by the degeneracy of spectral information in photometry. Here we point out the necessity and importance of a pure spectroscopic selection of quasars for a complete census of them and hence for a better view of the galaxy evolution and the universe, which is also feasible with the help of the forthcoming 4-metre Multi-Object Spectroscopic Telescope ([4MOST](#)).

We observe 50 quasar candidates (mainly red quasar candidates) with abnormal colors which make them unlikely to be regarded as quasars by common color criteria focusing on blue point sources, and find out that 45 of them are indeed quasars, including 23 normal quasars, 18 BAL quasars, 2 detached BAL quasars, and 2 peculiar quasars. The other 5 objects are expected to be stars as we simply select them close to the stellar locus. Such large quasar populations in the point sources with uncommon colors, especially in those which have red $g - r$ and $J - K$ colors, indicate that many quasars may be red or have peculiar colors and they have been overlooked by normal color criteria.

We elaborate our observation process, spectral reduction procedures, and spectral analysis methods in Chapter 2, Chapter 3, and Chapter 4 respectively. In Chapter 5, we present all the spectra we have analyzed and explain in detail how we determine their redshifts and amount of dust extinction. Besides, the overall results are displayed to highlight the incompleteness of quasar populations selected by color criteria.

In the end, we propose a quantitative way to measure the redshifts of the detached BAL quasars that don't have any high ionization emission lines in their spectra. Moreover, we suggest a detailed dusty wind model including the required inner structure of the outflows to interpret the peculiar spectral features of the detached BAL quasars.

Acknowledgements

This is a quite emotional moment when I will finish my two-year master's study at the Niels Bohr Institute very soon. My gratitude to all the professors and friends I met along the journey is beyond words.

First of all, I want to thank Johan, my greatest master's thesis supervisor who is very reliable, for his irreplaceable role in my very first real research in astronomy and for his patient guidance on my way to pursuing my childhood dream. Without his wonderful help and enlightening advice, I can't have had such a smooth and lovely start in academia. I will never forget the precious experience we worked together and all the pleasant talks we had in the past year, which I benefit a lot. I truly appreciate you, Johan, for leading me into the marvelous world of quasars, the most powerful objects in the universe.

Besides, I'm also extremely grateful for the time I shared with the excellent astrophysicists and fellow astronomers at the Cosmic Dawn Center. The vibe in the office is very relaxing and delightful. I'm so thankful for all the friends I met in Copenhagen. You're especially amazing and the great time we had is very unforgettable. Hope all of you guys can get a position successfully either in industry or academia after graduation. I really cherish our friendships.

In addition, special thanks to all the professors who have taught me different courses in the first year of my master's study. I will forever remember the colorful fields of astronomy shown by Prof. Lise Bech Christensen, Prof. Martin Elias Pessah, Prof. Troels Haugbølle, Prof. Darach Jafar Watson, Prof. Jes Kristian Jørgensen, Prof. Uffe Gråe Jørgensen, Prof. Steen Harle Hansen, and Prof. Lars Egstrøm Kristensen.

Moreover, I'd like to give a big shout-out to one of my best friends, Shangcheng Yan, who is now a medical student in China. He is very busy but still helped me with creating the beautiful illustration of a new dusty wind model we propose in this work. Wish him all the best and he will definitely be an outstanding doctor in the future. Hope we can

have fun together soon.

Last but definitely not least, I really appreciate the unconditional support from my parents to help me chase my passions. I hope they can feel relieved after my graduation and enjoy their life. Don't worry about me and I will take care of myself perfectly. Be happy and keep in good health! We haven't seen each other for almost two years. I really miss you and I truly hope the way back home can be much easier in the near future.

Contents

Abstract	i
Acknowledgements	iii
1 Introduction	1
1.1 Background	1
1.1.1 Discovery of quasars	2
1.1.2 Redshift	4
1.1.3 Properties of quasars	5
1.1.4 Unified model	8
1.1.5 Quasar subtypes	11
1.1.6 Treasures of quasars	13
1.2 Color Selection Effects	15
1.2.1 UV excess selection	15
1.2.2 K excess selection	18
1.2.3 Mid-infrared selection	19
1.3 Red quasar candidates	21
2 Data Acquisition	25
2.1 Preparation	25
2.1.1 Target selection	25
2.1.2 Visibility plots	26
2.1.3 Instruments and filters	27
2.1.4 Exposure time	28
2.2 Observation	30
2.2.1 Observation process	30
2.2.2 Observed targets	31
3 Data Processing	33
3.1 Data Reduction	33
3.1.1 Fundamental theory	33

3.1.2	Basic knowledge of CCD astronomy	34
3.1.3	Readout noise	36
3.1.4	Bias frame	37
3.1.5	Flat field frame	39
3.1.6	Dark current	41
3.2	Spectral Calibration	42
3.2.1	Wavelength calibration	43
3.2.2	1D spectra extraction and sky background subtraction	43
3.2.3	Flux calibration	44
3.2.4	Error propagation	46
4	Spectral Analysis	49
4.1	Dust Extinction	49
4.1.1	Absorption	50
4.1.2	Scattering	52
4.1.3	Extinction	52
4.1.4	Standard extinction curves	55
4.1.5	SMC-like quasar extinction curve	58
4.2	Quasar Template	60
4.3	Fitting Procedures	63
5	Results and Discussion	65
5.1	Classifications and Properties of Observed Targets	65
5.2	All Spectra	73
	Notes on Individual Objects	81
5.3	Detached BAL Quasars	98
5.3.1	Quantitative redshift determination	100
5.3.2	Possible interpretation of the peculiar spectra features	104
6	Conclusions and Outlook	111
	Bibliography	113

Chapter 1

Introduction

Quasars, which are also known as 'QSOs' (shorten form of quasi-stellar objects), are very distant objects with extreme luminosity and they are actually one type of tremendously luminous active galactic nuclei (abbreviated AGN). The term 'quasar', the abbreviation of 'quasi-stellar radio source', was first introduced by [Chiu \(1964\)](#) to refer to a kind of point source with strong radio emissions for convenience. However, with more and more observations of this kind of object being taken, scientists found that not all the so-called 'quasars' have strong radio emissions, and actually the radio-loud part only accounts for 10% of the entire quasar population which is concluded by [Peterson \(1997\)](#). Since the radio-quiet counterparts, which have weaker emissions in the radio band, make up the rest 90% of quasars, it was no longer so appropriate to call these objects 'quasar'. The new term 'QSO' was given and used to denote this kind of distant but extremely luminous object, while 'quasar' is still used among papers simply due to historical reasons since it was widely accepted before we found the majority of QSOs are radio-quiet. In this thesis, 'quasar' is used to refer to such extremely bright and distant point sources regardless of their radio properties, for legibility and uniformity.

1.1 Background

In fact, 'quasar' is not an out-of-date name and it can also help us to recall the history of discovering such important objects with a wide range of applications in astrophysics nowadays. From the name 'quasi-stellar radio source', we can tell that quasars were first found as radio sources. Indeed, with the rapid development of radio astronomy in the 1950s, our observations were not only limited to optical bands. Many new objects were found in radio wavelengths, but it was difficult to locate them at first due to the limitation of angular resolution defined as eq. (1.1),

$$\theta \approx 1.22 \frac{\lambda}{D}, \quad (1.1)$$

where θ is the angular resolution (the minimum angle between two objects that can be resolved by detectors), λ is the wavelength of observed radiation, and D denotes the diameter of the telescope's objective. For radio telescopes, if one wants to reach the same angular resolution as optical telescopes, the required diameter can be much larger than that of optical telescopes, since the radio wavelengths (1 mm \sim 10,000 km) are much longer than the wavelengths of optical light (380 nm \sim 750 nm). It was quite hard to build such large radio telescopes during the 1930s, so scientists can only know radio radiations came from some regions, but they couldn't find out which specific targets emitted those radiations. For instance, [Jansky \(1933\)](#) first discovered the radio 'noise' came from outside the solar system, but he could only determine that the origin of radio waves is located at the place with a right ascension of 18 hours \pm 30 minutes and declination of $-10^\circ \pm 30^\circ$. The errors are quite large as we can see, not to mention finding an optical counterpart of the radio source from that.

However, we could actually find radio sources precisely in the following 10 years, while the techniques required to build large radio telescopes cannot improve that fast. What happened? It was that the application of interferometry to radio telescopes boosted radio astronomy. In 1946, [Ryle & Vonberg \(1946\)](#) became the first scientists to publish the utilization of radio interferometry, after which more and more discrete sources were distinguished and even relatively precise positions of them were computed, like the first discovered radio galaxy Cygnus A and supernova remnant Taurus A, by [Bolton \(1948\)](#). It was then possible to match these discrete radio sources with known optical targets to investigate them in more detail.

1.1.1 Discovery of quasars

Surprisingly, some objects were found to be very anomalous among the different radio sources. One couldn't find the optical counterparts of these radio sources other than some faint point sources that resembled distant stars. Moreover, it was quite hard to explain why such 'stars' can emit a large amount of radiation in lots of frequencies. As a result, scientists couldn't really know what this kind of object is for a fairly long time, and just named them as 'quasi-stellar radio sources'. [Matthews & Sandage \(1963\)](#) found the first quasi-stellar radio source, 3C 48, with the first direct plate taken on September 26, 1960. It has properties described above in Section 1.1 with the optical identification of a 'starlike' source, surrounded by faint wisps of nebulosity, which would later be

the first evidence for a quasar with a surrounding galaxy confirmed by [Boroson & Oke \(1982\)](#).

However, the nature of quasars remained elusive at the beginning of the 1960s. Bolton, Matthews, and Sandage reported that 3C 48 was the first discovered radio star in the 107th Meeting of the American Astronomical Society with an unpublished paper (see [Matthews & Sandage 1962](#)), thinking it might be a distant galaxy with a small possibility or a nearby star within our galaxy with the most peculiar properties, which was wrong according to what we know at present. Besides, the spectrum of 3C 48 also defied interpretation, in which several broad emission lines appeared at uncommon wavelengths. Such strange emission lines made this kind of stellar object more mysterious.

The breakthroughs came out during 1962 - 1963, starting from the first precise coordinates of 3C 273 determined by [Hazard et al. \(1963\)](#), using the method of lunar occultation with the 210-ft radio telescope at Parkes in a positional accuracy better than 1 arc second. Lunar occultation is such a method that one can calculate the position of targets from their disappearing and reappearing times from the back of the moon, which can be estimated from the change of flux density at the edge of the geometrical shadow. By observing the full occultation of 3C 273 with both visible immersion and emersion on August 5, 1962, at 136 and 410 MHz, they confirmed that 3C 273 has two components, which are elongated 3C 273A with a representative Class II radio spectrum and 3C 273B with a 'most unusual' flat spectrum, having a central bright core about 0.5 arc second wide, contributing most of its flux. They pointed out that the position of a 'star' with 13th magnitude was very close to that of component B, which was possible to be the optical counterpart of 3C 273B. Besides, they agreed that this 'star' and its associated nebulosity can be very presumably the radio emission source.

Just a few months after that, one of the most important progress in the discovery of quasars was made by Dr. M. Schmidt in late December 1962. By using a 200-inch telescope, [Schmidt \(1963\)](#) got the spectra of the magnitude 13 'star', which is the only optical object that can be seen near the components of 3C 273. A series of broad emission lines at unfamiliar wavelengths on a fairly blue continuum was found, which are different from those features of 3C 48 with multiple emission and absorption lines and a strong ultraviolet (UV) excess, but both showed no signs to be ordinary stars. After noticing that there were four emission lines at wavelengths 5632 Å, 5032 Å, 4753 Å and 4595 Å, with decreasing strength toward the blue, Schmidt supposed them as Balmer lines of hydrogen (corresponding H β , H γ , H δ , and H ϵ) and determined a redshift of 0.158. Such assumption in turn helped him to identify Mg II λ 2798 at 3239 Å and a forbidden line of [O III] λ 5007 at 5792 Å, which confirmed the validity of the redshift

$z = 0.158$. More evidence from [Oke \(1963\)](#) supported this result. Oke observed 3C 273 with the 100-inch telescope at Mount Wilson both in visible and infrared bands. By adopting the proposed redshift of 0.158, a strong emission feature near 7600 \AA was in great agreement with the expected wavelength of $H\alpha$.

With the proven 0.158 redshifts of a star-like object, it was the first time for people to consider it not as a star within our galaxy, but as another kind of object and somewhat convinced. From the stellar appearance of 3C 273 and its corresponding large observed redshift, [Oke & Schmidt \(1963\)](#) suggested that it was most likely to be the luminous nucleus of a galaxy, which would be located at a distance of 500 Mpc away. Although another guess was given that it could be a star with a large gravitational redshift, like a neutron star. While the occurrence of both permitted and forbidden lines at the single redshift, with the breadths of only 1 to 2% of the corresponding wavelength of lines, makes it extremely improbable. Besides, it's extremely unlikely that it was only due to the physical motion of the object, which may indicate that 3C 273 was moving away from us at about 47000 km/s. If people still insisted that it was a star within our galaxy, then there was nothing to do with the expansion of space, and it was impossible for a star to recede at such high speed because of its own motion.

Moreover, the 0.158 redshifts of 3C 273 gave the possibility for high redshifts (at that time) of the objects with stellar appearance. [Greenstein & Matthews \(1963\)](#) derived the redshift of the first discovered quasar 3C 48 very soon by accepting the principle that it had a high redshift. After recognizing the Mg II line near 3832 \AA with the highest intensity in the spectrum, the redshift of 3C 48 was figured out as 0.3675. Thereafter, the riddle of quasar spectra was finally solved and the completely new object, quasar, was discovered and confirmed.

1.1.2 Redshift

As we mentioned the redshift in the previous Sect. [1.1.1](#), it's a good time to explain what the redshift is in astronomy. A redshift (denoted by z) is a measure of the increase in the wavelength of radiation emitted from an object moving away from us, demonstrated by eq. [\(1.2\)](#), caused by the Doppler effect.

$$z = \frac{\lambda - \lambda_0}{\lambda_0} = \frac{\lambda}{\lambda_0} - 1 \quad (1.2)$$

In eq. [\(1.2\)](#), λ refers to the observed wavelength of a certain line in the received spectrum by us on the Earth, and λ_0 is the intrinsic or rest wavelength of the same line

which is measured in the laboratory, which can represent the original wavelength of radiation when it's emitted from the object. Eq. (1.2) can be easily transformed to be expressed with frequency by substituting $\lambda = c/f$ into it, where c is the speed of light (approximately 3×10^5 km/s) and f represents frequency. The redshift is a natural consequence of the fact that the universe is expanding faster and faster (Riess et al. 1998; Perlmutter et al. 1999), indicating that any two gravitationally unbound objects in the universe are moving away from each other with time.

The redshift usually acts as the distance indicator in astronomy, based on the accelerating expansion of the universe. According to the Hubble's law, $v = H_0 D$, where v denotes the speed of separation, H_0 is the Hubble constant, with a value of roughly 70 (km/s)/Mpc, and D is the proper distance between two objects in the universe, changing over time, from the perspective of us on the Earth. The further an object is from us, the faster it recedes. Such receding motion is reflected in the increase of radiation's wavelength, or the redshift in other words. Therefore, in the case of low velocity ($v \ll c$) and the local universe ($D \ll \frac{c}{H_0}$), the redshift is related to the distance in the following manner, as shown in eq. (1.3). Thus, the object further from us has a larger redshift.

$$z \approx \frac{H_0 D}{c} \quad (1.3)$$

On the contrary, if an object is moving towards us, the wavelength of its radiation will decrease, according to the Doppler effect as well, which is described by the blueshift. The appearance of the blueshift can always help us to identify the outflows or the rotational motion of an object.

1.1.3 Properties of quasars

More and more scientists started to accept that quasars are outside our galaxy, although there were still many conclusions that seemed implausible, and people really struggled with them for a long time. For instance, if the 'large' redshift of a quasar is due to the expansion of the universe, then the target must be very distant. According to eq. (1.4),

$$L = F * 4\pi D^2 \quad (1.4)$$

where L denotes the luminosity, F denotes the flux density and D refers to the distance from the observer to the target, with the total flux integrated over all wavelength ranges

of used filter bands and an extreme distance, the luminosity of quasars can be extraordinarily high. The fact that they emit much more radiation than other galaxies cannot be interpreted by any widely accepted mechanism.

Take the target 3C 273 we mentioned previously for example, [Greenstein & Schmidt \(1964\)](#) found that it has an apparent magnitude of +12.6, while it has an absolute visual magnitude of -26. Apparent magnitude demonstrates the brightness of an object observed from Earth, which depends on its distance to Earth, its inherent luminosity, and any extinction from the dust along the line of sight. However, absolute magnitude is a measure of an object's intrinsic luminosity, regardless of the distance and extinction. It's defined as the value of an object's apparent magnitude if we put the object 10 parsecs (roughly 33 light-years) away, while it's not diminished by the interstellar medium. It's a kind of standard measurement that we can directly compare the luminosity of different objects by hypothetically placing them at the same distance. Both of the values are on an inverse logarithmic astronomical magnitude scale, which is unitless and defined such that every time the magnitude changes by 1, the object's brightness changes by a factor of the fifth root of 100 (about 2.512), as described by eq. (1.5),

$$m_1 - m_2 = -2.5 \log_{10} \frac{I_1}{I_2} \quad (1.5)$$

in which m_1 and m_2 refer to the magnitude of the object 1 and 2, plus I_1 and I_2 refer to intensities in units of power per unit area which are measured from Earth. Thus, it shows that the lower value of an object's magnitude has, the brighter it will appear. In this way, we can also know that the absolute magnitude can be calculated as follows.

$$m - M = 2.5 \log_{10} \left(\frac{d}{10} \right)^2 = 5(\log_{10} d - 1) \quad (1.6)$$

In eq. (1.6), m is the apparent magnitude of an object, M is its absolute magnitude and d is the distance to it in parsecs, derived from eq. (1.5) using the inverse-square law on the basis that intensity decreases proportionally to distance squared.

Although the apparent magnitude of 3C 273 seems to be a little low, with the fact of its enormous distance from us, it actually has a very high intrinsic luminosity, demonstrated by its -26 absolute visual magnitude, and can be more or less felt if one imagines that a 'star' is shining brightly as our Sun from 33 light-years away. [Greenstein & Schmidt \(1964\)](#) also calculated that the visual luminosity of 3C 273 is 4×10^{45} erg/sec, which is about 10^{12} times that of our Sun (with luminosity of 3.8×10^{33} erg/sec). It was quite

unbelievable for scientists at that time, because in spite of possibly even higher luminosity of supernovae, they only emit for dozens of days or hundred days at most, while a quasar can keep shining for at least 10^6 years.

How can quasars generate so much energy? It remained vague for several dozen years. But one thing was clear, quasars are extremely bright and distant objects with a small apparent size outside our galaxy, which was confirmed by [Greenstein & Schmidt \(1964\)](#), excluding other two alternatives to the interpretation of large redshifts of quasars, with one to be the Doppler effect of a high-velocity star and the other to be gravitational redshift, based on the similar reasons that were discussed by [Oke & Schmidt \(1963\)](#). There must be an unknown mechanism that drives such 'anomalous' progress, although now we know that quasars are very common in the universe and most galaxies, including our Milky Way, have possibly experienced such a period that they have active galactic nuclei in the galactic center, which may appear as a quasar.

Although the new and actually correct interpretation of the possible energy source of quasars was suggested very soon by [Salpeter \(1964\)](#) and [Zel'dovich & Novikov \(1967\)](#) independently, no one really attaches importance to it. They proposed that there are massive black holes in the center of quasars, and the accretion of gas and other materials into the central black holes gives a large amount of radiation in the form of accretion luminosity. The accretion luminosity can be simply expressed as,

$$L_{acc} = \epsilon \dot{M} c^2 \quad (1.7)$$

in which \dot{M} means the accretion rate, or more explicitly how much mass is accreted by an object per unit time, c is the speed of light and ϵ denotes the fraction of rest-mass energy converted to the emitted luminosity. It also can be understood as the efficiency of this kind of conversion. From what we know nowadays, [Lambourne \(2010\)](#) gives that the efficiency can vary from 5.7% to 32%, which is related to the rotation rate of black holes. The lowest case is for a non-rotating Schwarzschild black hole and the highest case is for a Kerr black hole that rotates very fast. It's actually quite high efficiency, especially compared to the p-p chain nuclear fusion of hydrogen that produces the energy of Sun-like stars. However, what's happening can be more complex. Not only can the gravitational energy of infalling mass be converted to luminosity, but also the immense friction between the materials in the accretion disk can contribute to the very high luminosity.

Besides, [Salpeter \(1964\)](#) also impressively suggested a correct solution to the issue of

depletion of angular momentum in the accretion process, which was thought to be realized via the turbulent viscosity, and it's also the widely accepted interpretation at present.

Now we know that quasars are a kind of active galaxy nuclei, with extremely high luminosity and small apparent size, powered by black holes occupying the center of them, but what do they really look like? What are their inner structures? All these questions can be answered by the unified model of AGN.

1.1.4 Unified model

There are different kinds of AGN, e.g., blazars, Seyfert galaxies (Seyfert I and II), quasars, and so on. They are defined simply from their observed properties, with the most luminous ones classified as quasars. Most of the sub-classes of AGN don't really have any physical differences, and they are just named to be so because of historical differences in their discovery or how they were classified at first, except for radio-loud and radio-quiet AGN. Nevertheless, the only difference between the radio-loud and radio-quiet AGN is that if there is a jet appearing or if there is any jet-related emission contribution in a simplified view, which may be attributed to the properties of the central black holes (e.g. the mass, the accretion rate, the accretion phase, or the black hole spin), but the transition from radio-quiet to radio-loud may in fact be continuous. The other sub-populations can be all classified into these two sub-groups (radio-loud and radio-quiet AGN), and the differences in observed properties of the objects in the same sub-group (radio-loud or radio-quiet AGN) are only due to the orientation of the AGN or how we observe them. In other words, the type of AGN we observed is somewhat determined by the viewing angle (see [Urry & Padovani 1995](#); [Beckmann & Shrader 2012](#)).

One typical example of this statement is that [Antonucci & Miller \(1985\)](#) showed that Seyfert 2 galaxies can actually be the same objects as Seyfert 1 galaxies, although they look so different in spectra that there are no broad lines in those of Seyfert 2 galaxies compared to Seyfert 1 counterparts. The absence of broad lines can be easily attributed to the difference in the physical conditions of these two kinds of galaxies, but it is unfortunately not the case. The fact is that when the Seyfert 1 galaxies are observed 'edge-on', the broad lines will be absorbed by the dusty outer torus surrounding the central black holes and accretion disks, and in this manner, they become Seyfert 2 galaxies. They are classified to be two groups only due to the effect of viewing angle, though it can be expected from the existence of the accretion disk with the rotation axis.

This fact actually makes things a little bit boring because the orientation of AGN can determine the appearance of themselves so significantly that it is the random pointing directions of objects that produce our current classification schemes, rather than the more interesting physical properties. However, this is nature and this is how it is.

A very clear and highly concluded illustration from [Beckmann & Shrader \(2012\)](#) is also presented here as Fig. 1.1.

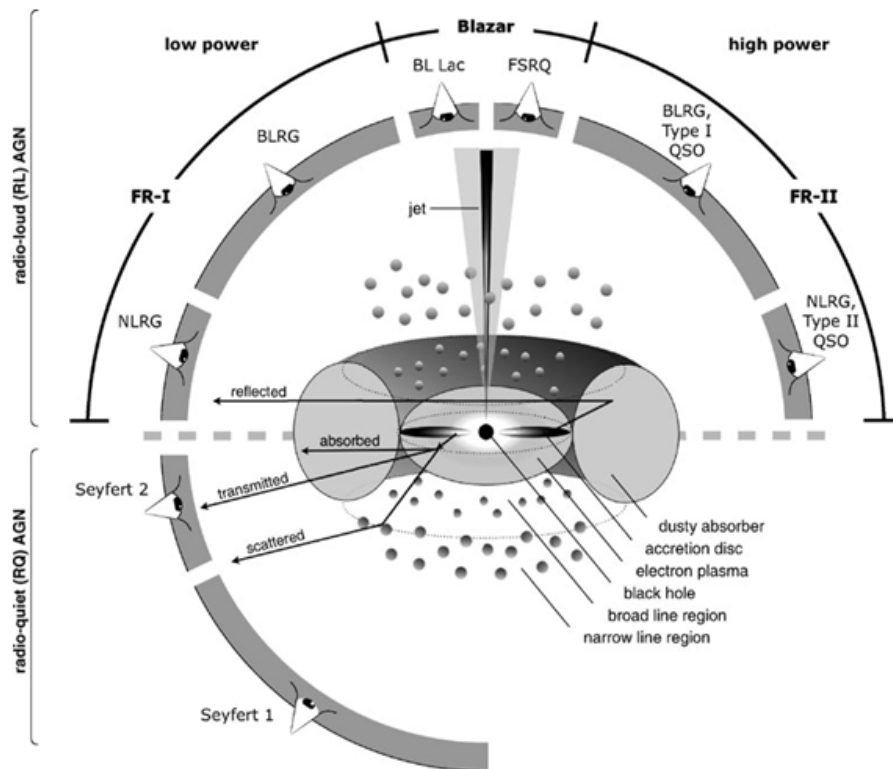


Figure 1.1: A schematic unified model of our understanding of the AGN phenomenon from [Beckmann & Shrader \(2012\)](#), where BLRG and NLRG denote Broad-line and Narrow-line radio galaxy, FSRQ denotes Flat-spectrum radio quasar. Note that although not presented here, the jet emission that appears in the radio-loud AGN are generally thought to be symmetric.

One thing which should be noted is that the radio-quiet AGN can also be observed as quasars, and they are actually much more than radio-loud ones as stated previously. Besides, many sub-types of quasars are also not shown in Fig. 1.1, like the broad absorption-line (BAL) quasars, which may consist of 10% to 40% of radio-quiet quasars ([Turnshek 1984](#); [Gibson et al. 2009](#); [Allen et al. 2011](#)).

However, in general, our interpretation of AGN, as well as quasars, can be easily appreciated based on Fig. 1.1. As we can see, our current paradigm for AGN is that there is a black hole in the center of the object, surrounded by a luminous accretion disk, which is then encircled by a very thick and dusty absorber shaped like a torus in the outer region. The torus and the disk are thought to be on the same plane. Besides, A clump of very hot electron plasma pervades the space in-between them. In addition, there are clouds

containing gas and maybe dust orbiting around the central black hole and disk, which can radiate the broad emission lines that we see in the spectra. The regions where these clouds are located are called broad-line regions (abbreviated as BLR). The broad-line emission can also be produced by the accretion disk itself. On the contrary, there are also clouds inhabiting narrow-line regions (abbreviated as NLR) that are much further away from the black hole or even the torus. They are the origin of narrow lines that appear in the spectra of AGN. Since all the clouds are moving in Keplerian velocities, which can be demonstrated by eq. (1.8),

$$v_K = \sqrt{\frac{GM}{R}} \quad (1.8)$$

where v_K is the Keplerian velocity, G denotes Newton's gravitational constant, M is the mass of the central source (here are the central black hole and accretion disk) and R is the orbiting radius. According to eq. (1.8), the clouds that are closer to the central source will have higher speeds. Moreover, as the black holes are extremely massive and the orbiting radius of the clouds in the broad-line region is relatively small, their orbiting velocity can be very high, which will significantly broaden the emission lines from these clouds due to Doppler broadening. While the narrow-line regions all have much larger distances to the central black hole, they move slowly so the emission lines are narrow.

Because the broad-line regions are closer to the central source, there is also the possibility that broad emissions lines from them will be obscured by the torus in the transverse lines of sight. However, it's also possible for some broad-line emissions and continuum from the inner disk and clouds to be scattered by the hot plasma into these horizontal lines of sight. Sometimes, radio jets with initially relativistic velocity will also appear, producing radio emissions. It's a bit hard to sense the scales of all the different components from just a paradigm. [Urry & Padovani \(1995\)](#) gave a quantitative example that the radius of a black hole with a mass of $10^8 M_\odot$ is around 3×10^{13} cm, the accretion disk emits most of the radiation from a region between $1-30 \times 10^{14}$ cm, and the further one is the broad-line region, which spans from 2×10^{16} cm to 20×10^{16} cm. In addition, the inner radius of the torus is roughly 10^{17} cm, and the narrow-line region expands from 10^{18} cm to 10^{20} cm, while the jets are the objects that can reach the furthest place, which are detected from 10^{17} cm to 10^{24} cm.

1.1.5 Quasar subtypes

As we can see in Fig. 1.1, there are many subtypes of AGN, which are usually originated from different viewing angles. Likewise, when we observe quasars at different inclinations, we can often see distinct features in their spectra, which lead to dissimilar categorization of them, as illustrated in Fig. 1.2.

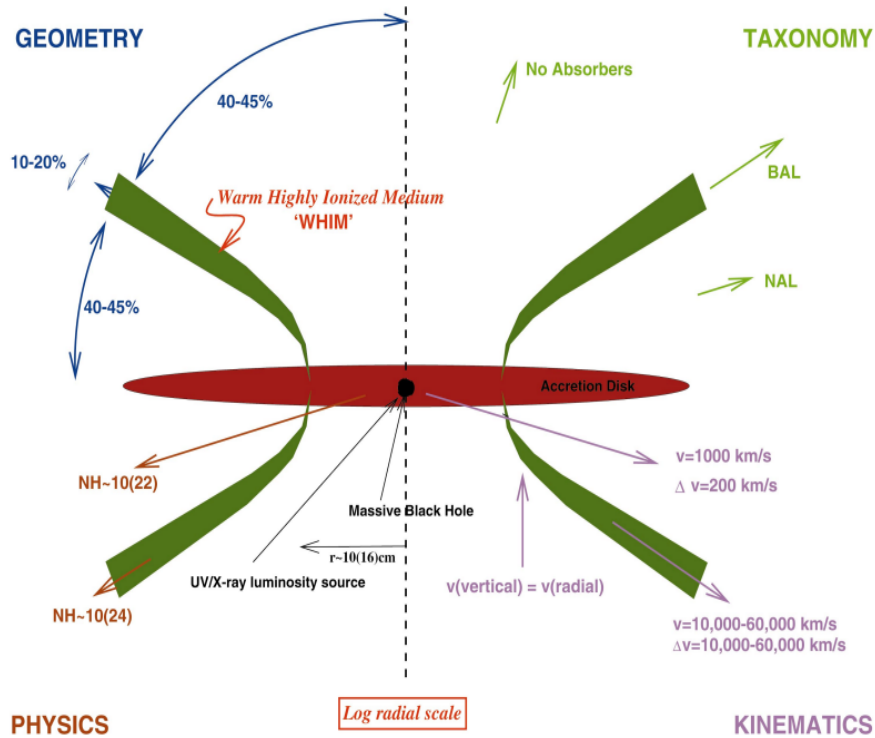


Figure 1.2: The model of the proposed quasar structure from Elvis (2000), with every quadrant showing the geometry (opening angles), taxonomy (spectral characteristics observed at different angles), kinematics (the speed of outflows along dissimilar lines of sight), and physical properties (some typical radii and column densities) respectively.

When observing the quasars at the angles less than 45% degrees to their rotation axes (the axis perpendicular to the plane of the accretion disk, as shown by the dashed line in Fig. 1.2), we can get the spectra of quasars with normal broad emission lines and without any absorption, if we assume there is no intervening material. These quasars are so-called Type 1 quasars or normal quasars, which are the counterparts of Seyfert 1 galaxies.

If there is no disk wind or outflow in the quasars, we can see Type 2 quasars when observing them at lower angles (within 40 degrees) to the accretion disk, whose accretion disk and broad-line regions are entirely shrouded by a large amount of gas and dust in the torus, showing no broad emission lines but only narrow ones (Zakamska et al. 2003). However, if there are outflows in the observed quasars when they are seen at

lower angles to the disk plane, they appear to be Narrow Absorption-Line (NAL) quasars and Broad Absorption-Line (BAL) quasars depending on the viewing angles, as shown in Fig. 1.2. What we are most interested in are the BAL quasars, since they are unique and often found in red quasars.

BAL quasars are thought to be observed through the outflows, which spread around 10 degrees, estimated from the observed population of BAL quasars (10%) compared to the total number of quasars. However, this observed population of BAL quasars may very well be too low due to bias, such as what has been estimated by [Allen et al. \(2011\)](#) that the intrinsic C IV BAL quasar fraction can be up to 40% of the entire quasar population, which is elaborated in Sect. 5.1. The appearance of the outflows generates the blue-shifted absorption lines beside normal emission lines, producing the P-Cygni profiles in the spectra, which is the key feature that helps us to distinguish the BAL quasars. In addition, only the quasars with absorption features showing at least 1000 km/s velocity in the C IV or Mg II absorption regions are usually considered to be BAL quasars ([Trump et al. 2006](#)), because the absorption lines have to be broad.

Besides, BAL quasars can be categorized further into several subclasses, which are High ionization BAL quasars (HiBALs) and Low-ionization BAL quasars (LoBALs). HiBALs are BAL quasars showing broad absorption lines from highly ionized species like C IV, N V, Si IV, and Ly α ([Hall et al. 2002](#)), but the absorption lines from low ionized species like Mg II, Al III, and Al II are not appearing, while LoBALs are those which both have the broad absorption features from highly ionized species and low ionized species mentioned above ([Voit et al. 1993](#)). Furthermore, the LoBALs which have broad absorption lines from Fe II and Fe III are called FeLoBALs, and so on. When the absorption lines are completely detached from the emission lines, indicating an extremely fast outflow, such BAL quasars showing no P-Cygni profiles anymore are called detached BAL quasars, which are especially abnormal and elaborated in Sect. 5.3.

Apart from classifying the quasars according to their inclinations, quasars with different physical properties or at different evolution stages can also show disparate spectroscopic features, such as the radio-loud and radio-quiet quasars mentioned previously, in which the appearance of the jet gives rise to the strong radio-wavelength emission. Moreover, there are also weak lines quasars which strangely show no obvious emission lines in the UV/optical spectrum ([Leighly et al. 2007](#); [Diamond-Stanic et al. 2009](#); [Hryniewicz et al. 2010](#)), and [Hryniewicz et al. 2010](#) proposed that such weak line quasars can be attributed to that the quasar activity has just started, which may help to explain the detached BAL quasars in Sect. 5.3.

We currently have a general impression of quasars, but why are they so engaging? Besides the properties that they are the center and maybe the power engine of galaxies which are the biggest luminous object in the universe, they are also very useful tools for us to investigate the evolution of the universe.

1.1.6 Treasures of quasars

From what we know at the moment, over a million quasars have already been discovered (Secrest et al. 2021), and they are distributed in a redshift range of $z = 0.0421 - 7.64$ (Sanders et al. 1988; Leighly et al. 2016; Yang et al. 2020; Wang et al. 2021). Under such circumstances that quasars widely spread across our universe plus their extraordinarily strong emission, there are probably intergalactic materials, like neutral gas clumps, or galaxies, located on the lines of sight between the quasars and us. In this case, all the emissions from quasars passing through the intergalactic materials can be absorbed partly either by the dust or gas, or both. The induced absorption lines in the quasars' spectra can then be used as powerful probes of the intergalactic medium and the early galaxies to dramatically enhance our understanding of the early universe and its evolution process. There is a big advantage of studying quasar absorption lines since they can help us to detect the faintest galaxies that are very difficult to be examined by their own emissions (Weymann et al. 1981; Rauch 1998; Wolfe et al. 2005).

"Damped Lyman-alpha Absorbers" (abbreviated as DLAs) are classic examples of investigating galaxies with the help of quasar absorption lines (Wolfe et al. 2005). Here is a diagram demonstrating such objects as Fig. 1.3.

The DLAs are identified by their broad damping wings in the Lyman-alpha forest, which is also a very crucial probe of intergalactic gas clouds containing neutral hydrogen atoms in different redshifts (Rauch 1998). The broad wings are produced by the very dense gas clouds in the galaxies between the quasar and us, while a bunch of discrete narrow absorption lines are generated by many separate less dense hydrogen clouds in the intergalactic medium. The very dense clouds in DLAs create very high column densities of atomic hydrogen, which are thought to be larger than $2 \times 10^{20} \text{ cm}^{-2}$ (Wolfe et al. 1986), and it also guarantees that most of the hydrogen atoms must be neutral.

For such dense and cold clouds, it's nearly impossible for us to study them from their emission properties, which makes the investigation into quasar absorption systems the only way to examine such neutral gas clumps (Krogager et al. 2019) with existing facilities. Moreover, neutral atomic gas clouds are very essential for the formation of stars, which are thought to be born in molecular clouds, plus the cold neutral atomic gas

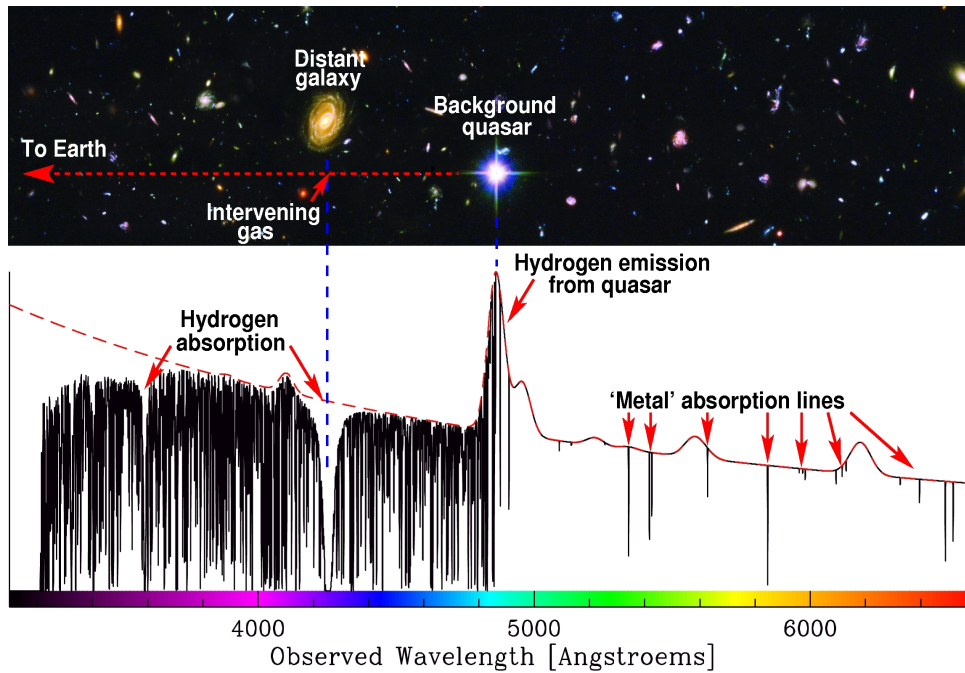


Figure 1.3: An illustration of the DLA, in which the big absorption trough shortwards of the Ly α line indicates the existence of an intervening galaxy. **Credit:** Michael Murphy.

clouds are the predecessors of molecular clouds (Wolfire et al. 2003). In addition, the large column density structures dominate the neutral gas mass density (Prochaska et al. 2005, Noterdaeme et al. 2009). In conclusion, DLAs really play a key role in reserving the neutral gas for star formation and thereafter galaxy formation. Besides, metal absorption lines also appear in the spectra of DLAs, which makes DLAs also a powerful tool to study galaxy evolution. Furthermore, quasars and AGN can also be used to study the chemical properties and evolution of the intergalactic materials (Pettini et al. 1994; Lu et al. 1996; Leighly et al. 2016).

As quasars are so important and indispensable for our understanding of galaxy formation, galaxy evolution, and hence the evolution of the universe, for example, giving us the insight into the Cosmic Reionization (Zhu et al. 2021), we need to find as many of them as we can. It's very crucial to make a complete census of quasars, to not miss every stage of galaxy evolution, not to mention that quasars themselves are also quite charming, which can help with enriching our knowledge of the growth of black holes (Eilers et al. 2017) or giving us the insight to the Cosmic Reionization.

To achieve such a goal, we may need a completely different method to select quasars out of the countless objects in the universe, distinct from the selection criteria we are using now. Since the widely utilized criteria for color selection of quasars at present may induce severe bias on what we can find as quasars.

1.2 Color Selection Effects

In fact, selection effects in searches for quasars have been already noticed since the very first discovery of quasars. As introduced in Sect. 1.1.1, quasars were first found as radio sources, which made the significant radio emission thought to be the intrinsic property of quasars. Hence, people were naturally tempted to look at radio sources for quasars, while Sandage (1965) found very quickly that some objects which have similar optical features to the radio-loud quasars are actually radio-quiet, which are now broadly accepted that the majority of quasars are radio-quiet. That means if we keep using the original radio selection criterion, we would miss 90% quasars that are discovered nowadays. Boroson & Green (1992) highlighted the incompleteness of quasar samples due to the radio selection effect as well.

This was the first time for selection effects to show off in the research of quasars, and they have highly biased our searching process for quasars for many years. They may still keep playing a key role in misleading us on the way to finding the entire quasars population unless we discard the color selection techniques completely. Since if we only try to make the color criteria more and more sophisticated, as what we did in the past years (Richards et al. 2002; Richards et al. 2009; Yèche et al. 2010; Bovy et al. 2011; Kirkpatrick et al. 2011; Stern et al. 2012; Ross et al. 2012), it will cause new problems and bias (Stern et al. 2012; Krogager et al. 2019). Fortunately, it caught some scientists' attention these years (Clowes 1981; Bell & Comeau 2010). In addition, Gavignaud et al. (2006) and Bongiorno et al. (2007) showed that 35% of the faint quasars may be missed because of the color selection and the point source requirement for selecting quasars. Fynbo et al. (2013) presented that part of the missed faint quasar population can be attributed to the dust-reddened quasars, which are our main focus in this thesis.

1.2.1 UV excess selection

Though Sandage (1965) pointed out the selection bias of the radio-selection regime, what he introduced later as the optical selection criterion for quasars, actually instigated another selection effect on the search for quasars to only unobscured ones, as stated by Stern et al. (2012) and Krogager et al. (2019). Sandage (1965) found that most of the quasars discovered at that time were 'blue', based on Fig. 1.4.

As we can see in Fig. 1.4, all the sampled quasars are separated from the track of main-sequence stars, showing the significant UV (Ultraviolet) excess (UVX) of them compared to normal stars. The distinct difference between these two groups then became the feature that was used to select quasars out of stars. That is to say when plotting candidate

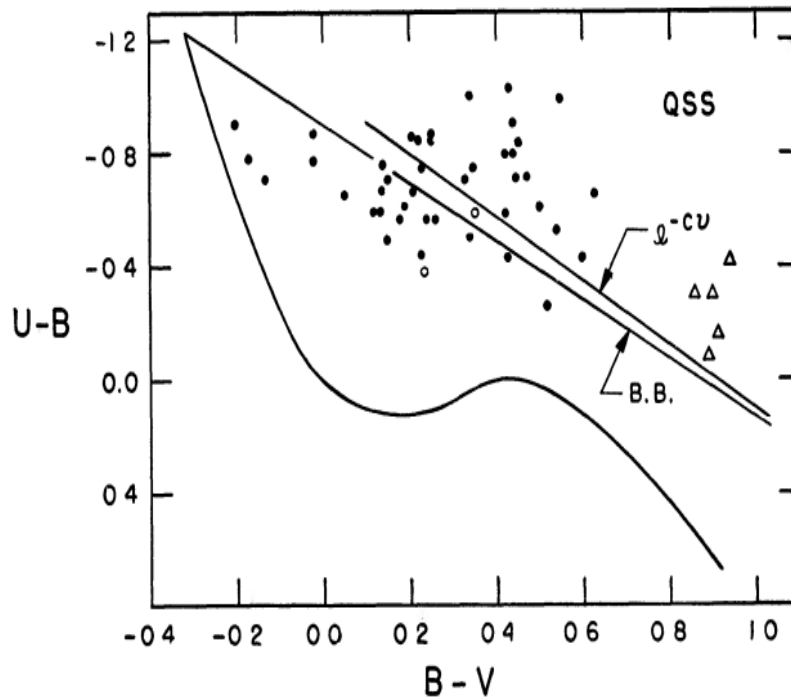


Figure 1.4: The $U - B$, $B - V$ (U: Ultraviolet_365 nm; B: Blue_445 nm; V: Visual_551 nm) color-color diagram of 44 quasars (black dots) and 5 galaxies (triangles) from [Sandage \(1965\)](#), with showing the normal luminosity line of main-sequence stars (class V) and two straight lines indicating the black-body radiation plus the radiation from objects with energy distribution described by eq. (1) in [Sandage \(1965\)](#).

quasars and stars on the same color-color diagram, objects that deviated from the normal stellar track can be considered to be quasars, for their relatively blue colors (i.e., $U - B < 0$).

The reason why we only consider the color difference between quasars and stars is that quasars are so dissimilar to other extended sources, like galaxies, in morphology, and we can very easily distinguish them by imaging without the help of spectroscopy. Only when quasars are contaminated by other point sources, most of which are stars, do we need to do spectroscopy. However, to get spectra of candidate quasars one by one is extremely time-consuming, so making photometric measurements is a good choice and that's why scientists are always trying to find the color differences between quasars and stars to distinguish them.

During past decades, scientists kept improving and refining the color selection criteria. [Schmidt & Green \(1983\)](#) improved the selection method based on the general blue colors of quasars to a single but more specific color criterion $U - B < -0.44$, using samples of 114 objects from the Bright Quasar Survey. In the meantime, the infrared selection criterion was also raised after noticing that the intrinsic hot torus surrounding the black holes in quasars can be traced by its infrared emission, firstly discussed by [Low & Kleinmann \(1968\)](#), while there is no such feature in stars. Besides, looking for

variability can also be considered as a selection technique according to the fact that quasars often display variable brightness (Usher 1978; Usher & Mitchell 1978).

However, as said above, the UVX selection criterion can give rise to a new bias that merely unobscured quasars can be found in such a way, because there is dust everywhere in the universe, which can be present in the torus of quasars themselves, in the quasar host galaxies, and in the intervening medium on the line of sight. Dust is a really efficient absorber for UV and optical radiation, so it can have a crucial influence on the color of quasars (more is introduced in Sect. 4.1). Dust can absorb the UV and optical radiation from quasars, and emit in a longer wavelength, which will then make these dust-obscured quasars appear to be red, which can be neglected by normal UVX selection techniques due to less UV excess (Krawczyk et al. 2015). Moreover, redshift can also significantly affect the color of quasars. Because all the filters have the bandwidth of roughly hundreds of nanometers within which the transmissivity is relatively high as shown in Fig. 1.5, plus the fact that there are many broad emission lines in the quasar spectrum, the magnitude of that specific band can be enhanced dramatically when these emission lines with high intensity happen to be shifted into these photometric bands.

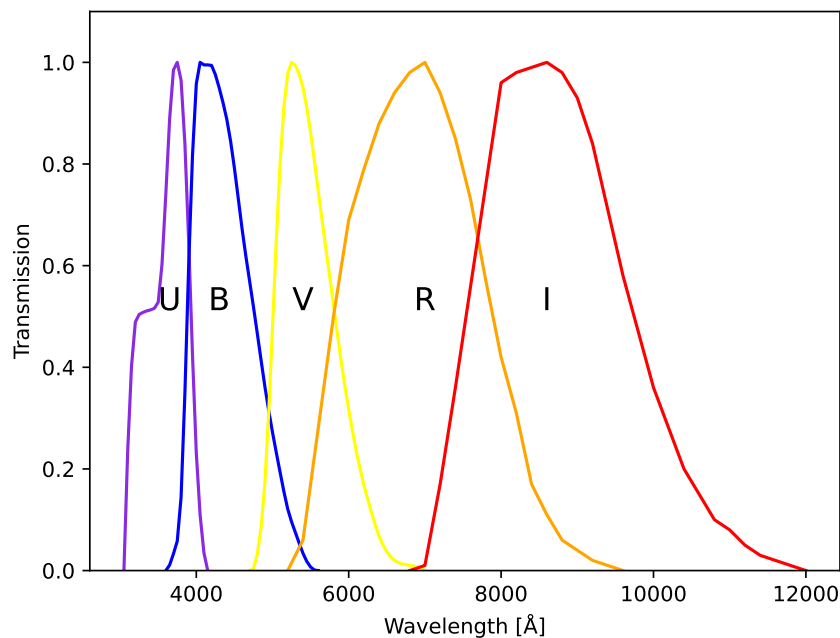


Figure 1.5: Transmission curves of an example of Johnson and Bessel filter-set (U, B, V, R (Red_700 nm), I (Infrared_860 nm)) used in photometric measurement (Johnson & Morgan 1953; Bessell 1990), plotted with the help of the Python package **synphot** developed by STScI Development Team (2018). Note that there are many different filter sets used in different telescopes.

Take the strongest Ly α line (with the wavelength of 1215 Å in the rest frame) in normal quasars for example, and the bandwidth (Full width at half maximum) of the B filter

(centered at 4450 Å) is roughly 940 Å. For quasars with redshifts between 2.3 and 3.0 ($2.3 < z < 3.0$), the Ly α line will be redshifted into the passband of the B filter, making these quasars much brighter in the B band, so they will appear much bluer than others, even resulting in $U - B > 0$. This will cause a strong bias that we can significantly overlook quasars located around $2.3 < z < 3.0$ if we just focus on those objects with UV excess, making our quasar samples at $2.3 < z < 3.0$ extremely incomplete.

Later, more sophisticated color criteria were extended to the optical/near-infrared range, but they still take the UV excess as a prerequisite, such as the SDSS-I and SDSS-II quasar target selection, also called the Legacy Survey Target Selection, based on the i band (7625 Å) color features of quasars (Richards et al. 2002; Richards et al. 2009). However, these selection methods can't get rid of being influenced by the dust extinction (Krogager et al. 2019) and are hampered at some certain redshifts (Stern et al. 2012) since the locus of quasars at the redshift around 2.7 overlaps that of A stars and blue horizontal branch stars in color-color space in the optical/near-infrared bands (Ross et al. 2012; Fan 1999).

1.2.2 K excess selection

For the deficiency of UV excess selection criterion, Warren et al. 2000 introduced a new selection method for quasars based on their brightness excess at the K band ($2.17 \mu\text{m}$). It's according to the difference between the spectra of quasars and stars, because the quasar spectra have a power-law nature, while the star spectra have a convex shape, which makes the radiation from stars have lower intensity at both shorter wavelengths (blue) and longer wavelengths (red). The emission excess at bluer wavelengths of quasars yields the UV excess selection method, so Warren et al. 2000 naturally utilized the fact that quasars are also brighter than stars at redder wavelengths and generated the K excess (KX) selection criterion. Moreover, it has a big advantage over the UV excess method since it works well even for dust-obscured quasars, as illustrated in Fig. 1.6.

In Fig. 1.6, we can notice that the substantial K band excess feature of quasars compared to stars is apparent both in the unreddened and reddened quasars. Warren et al. 2000 gave a tentative selection boundary to be $J - K > 0.36(V - J) + 0.18$. Nevertheless, this method still can't overcome the influence of the redshift and the K excess was presented to be substantial among quasars and stars with a similar $V - J$ color, while in the real selection scenarios, such restriction is hard to be kept as long as we want to derive a complete population and it may be no longer valid between quasars and stars with distinct $V - J$ color.

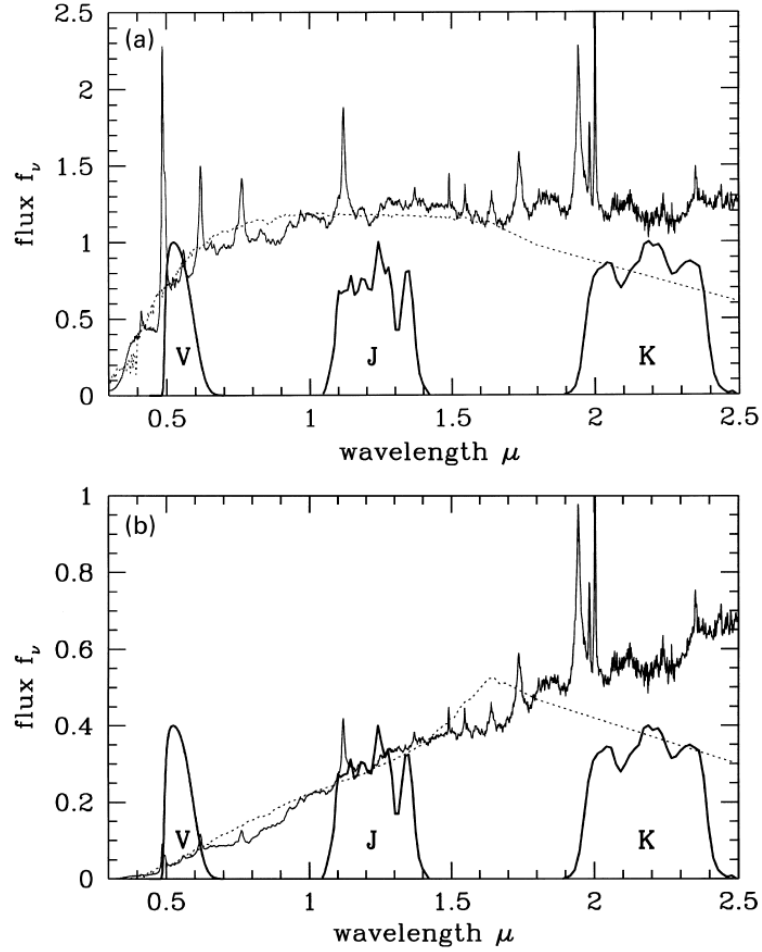


Figure 1.6: Comparison of the spectral energy distribution of quasars and stars with a similar $V - J$ color from the optical to near-infrared presented by Warren et al. (2000), with the composite quasar spectrum from Francis et al. (1991) and the star template of different types from Buser & Kurucz (1992) and Kurucz (1979), overplotted with the V, J and K filter transmission curves. The upper panel presents the spectra of a normal quasar without extinction at $z = 3$ in the solid line and an early K-type star in the dotted line. The lower panel shows the spectra of the same quasar but reddened by an intervening cloud at $z = 2.5$ with the amount of extinction being $E(B - V) = 0.3$ (for more details on dust extinction, see Sect. 4.1) and an early M star to make sure they have a similar $V - J$ color.

1.2.3 Mid-infrared selection

There are also different selection rules based on the mid-infrared (MIR) color features of quasars, after the launch of the Spitzer Space Telescope and the Wide-field Infrared Survey Explorer (WISE), because of the fact that quasars are clearly separated from others in MIR color-color space (Wright et al. 2010; Nikutta et al. 2014). Stern et al. (2005) found a mid-infrared color criterion with over 80% detection efficiency and 17% contamination from galaxies and stars, covering 91% of the total quasars in their samples. However, X-ray-selected AGN can be missed by this criterion, pointed out by Barmby et al. (2006) and Brusa et al. (2009), and it may be influenced by the contamination from star-forming galaxies and high-redshift galaxies (Brusa et al. 2009; Park et al. 2010; Donley et al. 2012).

Based on the work of [Stern et al. \(2005\)](#), [Stern et al. \(2012\)](#) developed a much simpler mid-infrared color criterion utilizing the WISE photometry results, which is $W1 - W2 \geq 0.8$ in the Vega magnitude system, with the W1 filter at $3.4 \mu\text{m}$ and the W2 filter at $4.6 \mu\text{m}$. This criterion can reach over 95% reliability rate in the COSMOS field ([Sanders et al. 2007](#)), compared to the overall 66% efficiency of selecting quasars (quasars/quasar candidates) of the SDSS Legacy Survey Target Selection ([Richards et al. \(2002\)](#)). This mid-infrared color criterion is quite simple and elegant, but it's not perfect and optimal. Contamination from massive galaxies at $z \gtrsim 1$ with the similar $W1 - W2$ colors to those of quasars can decrease the selection robustness. Moreover, it becomes not quite credible for red objects, which are encircled by the red curve in Fig. 1.7. Fig. 1.7 shows the objects, which have photometric data simultaneously existing in the databases of the [Gaia](#), [SDSS](#), [UKIDSS](#), and [ALLWISE](#), plotted in the $g - r$, $J - K$ color-color space ($g_{477} \text{ nm}$; $r_{623} \text{ nm}$; $J_{1.25} \mu\text{m}$), with adopting the $W1 - W2 \geq 0.8$ as the color criterion.

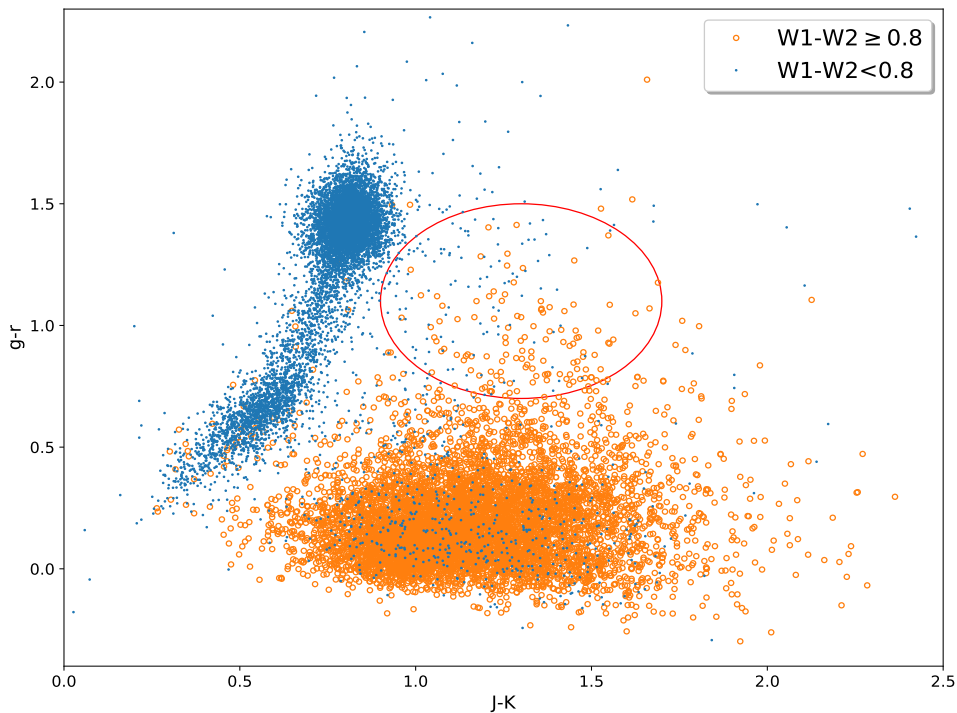


Figure 1.7: The color-color diagram of objects observed by multiple surveys, which illustrates their optical and infrared color excess, with orange circles being the $W1 - W2 \geq 0.8$ criterion selected quasars and blue dots as the predicted stars. These objects are chosen by requiring $J < 30$ and $K < 30$ to make sure they aren't too faint and influenced by the noise too much, with the UKIDSS and SDSS types to be stars, to ensure we only include the point sources here.

In Fig. 1.7, the stellar locus shown by blue dots and the quasar clump formed by orange circles are very obvious, verifying the blue-color nature of normal quasars in the optical bands, while we can see some orange circles in the stellar locus and quite a lot of blue dots overlapping the quasar clump, which makes these selection made by

$W1 - W2 \geq 0.8$ not trustworthy. In addition, there are a large number of objects dissociated from the stellar and quasar groups, such as those marked in blue or orange located in the red curve, making their classification quite ambiguous. Because the objects are brighter in the corresponding band if they have smaller magnitudes there, the objects circled by the red curve with greater $g - r$ and $J - K$ values (meaning that they have smaller magnitudes in the bands with longer wavelengths) are redder than those gathering in two clumps, which are believed to be reddened by the interstellar extinction. Therefore, we can tell that even the mid-infrared color criterion is still bothered by the dust extinction.

In addition to these color criteria generated in different photometric bands, multiple approaches are taken to identify quasars, such as the BOSS Quasar Target Selection (Ross et al. 2012), of which the algorithms are the combination of different tools and methods like the Kernel Density Estimation and the Neural Network. Afterward, the eBOSS Quasar Target Selection was introduced by Myers et al. (2015), merging the BOSS algorithms with the optical selection and a variability selection, while they only target the quasars at $2.2 < z < 3.5$ (BOSS) and $0.9 < z < 2.2$ (eBOSS). There are also lots of scientists adapting color criteria in multiple bands to form a refined one and try to reach a full selection of quasars (Fynbo et al. 2013; Krogager et al. 2015; Heintz et al. 2016).

In a word, to achieve a higher completeness of quasar selection, it's inevitable to make the criteria and algorithms more and more sophisticated. However, it can't ensure that we obtain the complete census of quasars, as the dust extinction and redshifts will always influence the color that quasars appear, while we are making color criteria based on limited samples. This consequence can be appreciated, since we don't have enough time to get the spectra of all the point sources in the universe to pick quasars out of them previously, and the imprecision of photometric data is the price we have to pay.

1.3 Red quasar candidates

However, we don't want to give up acquiring a complete census of quasar and we can actually achieve it in two different ways. On the one hand, Heintz et al. (2015, 2018, 2020) developed a purely astrometric way to only select those point sources with zero proper motions and zero parallaxes within one degree of the North Galactic Pole, based on the fact that although quasars and stars are both point sources, quasars are much further away than stars and they barely move in the sky. However, the selection efficiency of this method is not very high, which is near 60%, and much more stellar

contamination can be added when we get closer to the galactic plane.

On the other hand, we can seek to get the spectra of all the point sources and it will be feasible soon for the objects in the southern sky after the 4-metre Multi-Object Spectroscopic Telescope (4MOST) comes into service, which is able to attain the spectra of approximately 2400 targets in a hexagonal field-of-view of 4.2 square degrees at the same time, making it possible to obtain the spectra of a large number of objects in a reasonable time frame. My supervisor Johan is currently working on carrying out a large survey targeting quasars with 4MOST and hopefully, it can be carried out successfully on the 4MOST.

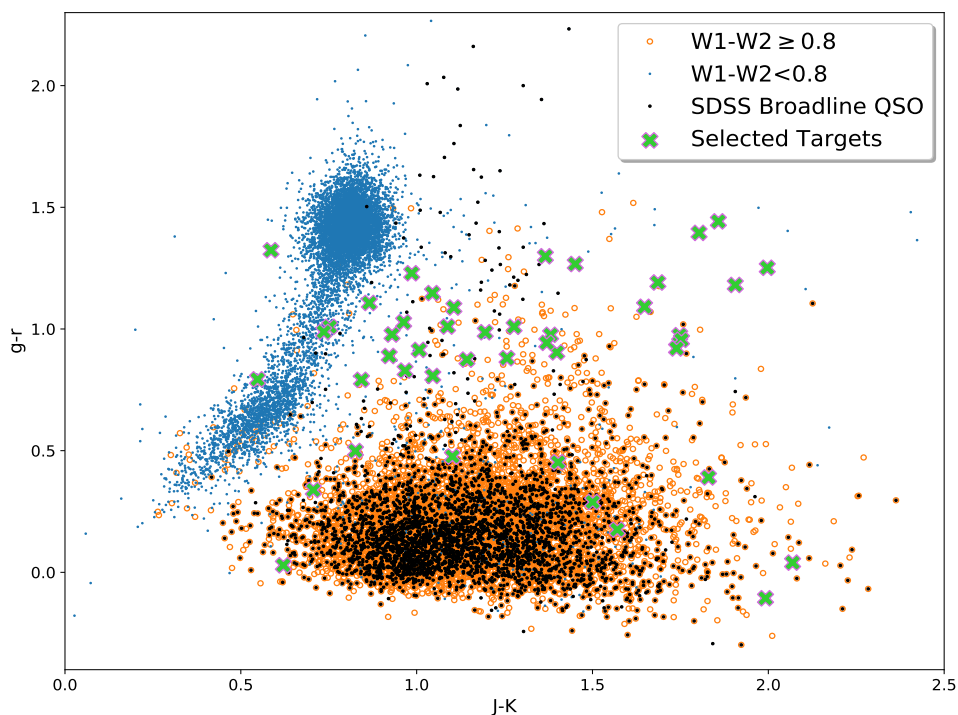


Figure 1.8: The targets we select for research are shown by lime green crosses in the color-color map together with quasars selected by $W1 - W2 \geq 0.8$. The SDSS confirmed quasars are given in black dots, from which we can see there are some quasars in the stellar locus and far away from the normal clumps of stars and quasars, but mainly grouped at the bottom cluster as predicted by the color criterion. However, it can still reveal the incompleteness of the quasar population selected by color selection methods plus their imprecision.

As we don't have the powerful facility 4MOST to get all the point sources' spectra at present, we can instead try to directly get the spectra of the reddened objects outside the two clumps shown in Fig. 1.7, like those in the red elliptical curve, to analyze them and find out what kind of objects they are, what spectral features they have, and why they have such abnormal colors if they are quasars. We selected 50 targets for investigation, which are mainly red quasar candidates (30 out of 50), lying above the normal quasar clumps and right to the stellar locus, as presented by lime green crosses in Fig. 1.8.

There are also extra targets selected by other students of Johan for curiosity, while all the targets presented in Fig. 1.8 are selected based on their peculiar colors different from those of the normal groups, as they are all situated at least on the outskirts of the normal quasar and star clumps. After taking their spectra, we can figure out why they are isolated from normal clumps and what makes them outliers.

By researching these targets with unusual colors, most of which are redder than typical stars and quasars, and unveiling whether they are quasars or not, we can attest to the importance of getting rid of color selection criteria for their harm to the complete census of quasars if many of these outliers are indeed quasars. Moreover, these objects are more likely to be worthy of research since they must have some special properties compared to normal ones that give rise to their distinctive colors, and we can usually find interesting spectral characteristics or even potential new phenomena from such uncommon targets.

To analyze these red quasar candidates, we should obtain their spectra first, which is introduced in Chapter 2. Second, we should process the raw spectra we get directly from the telescope, which is elaborated in Chapter 3. Third, we can analyze the processed spectra in such ways as discussed in Chapter 4. Lastly, the best-fit spectra and corresponding fitted parameters are presented in Chapter 5, with the detailed analysis and some discussion. Moreover, a new dusty wind model demonstrating the inner structure of outflows is also given in the last chapter.

Chapter 2

Data Acquisition

In this thesis, spectra of 50 quasar candidates were acquired and analyzed. 14 of them were observed by my teammates and me in the NOT Summer School 2021. The rest were provided by my supervisor, Prof. Johan Fynbo, which were taken using the Gran Telescopio Canarias ([GTC](#)) and the Nordic Optical Telescope ([NOT](#)). The full sample of quasar candidates is shown in Table [2.2](#).

From August 2nd to August 6th, 2021 (specifically on the 2nd, the 4th, and the 6th of August 2021), we observed a part of red quasar candidates and a few normal quasars utilizing the Alhambra Faint Object Spectrograph and Camera ([ALFOSC](#)) of the NOT on La Palma, together with my lovely teammates Rami Al-Belbeisi, Maja Skafsgaard, Marina Koukouvaou, Giannis Mageiras, and Youyou Li in the summer school. It was done remotely in Copenhagen due to the influence of Covid-19, and the following sections demonstrate the preparation and procedures of the astronomic observation based on this experience.

2.1 Preparation

2.1.1 Target selection

The first and the most important thing one need to consider before the observation is what you are going to look at. The selection of targets not only depends on your scientific goal but also on the telescope you are using. For our case, with using the NOT, the targets are better to have magnitudes roughly below 20 to be bright enough since the NOT is not a very big telescope. Besides, the targets should be within the field of view of the NOT. As the NOT is located in La Palma, Canary Islands, Spain, apparently the

objects that are only visible in the southern hemisphere should not be included in the target list. According to the location of the telescope in the northern hemisphere and our observation time in August, the feasible target should have a right ascension between roughly 15h and 5h, and a declination above -20° . Moreover, due to the limitation of the field-of-view of the ALFOSC (<http://www.not.iac.es/instruments/instruments.html>), the target should have an apparent size smaller than $6.7 \text{ arcmin} \times 6.7 \text{ arcmin}$. The targets we observed during the summer school were listed in Table 2.1 and all the spectra of them are shown in Sect. 5.2.

Table 2.1: The 14 observed quasar candidates using the NOT by us in the summer school.

Target	RA (J 2000) [hr : min : sec]	Dec (J 2000) [deg : min : sec]	Telescope	Exposure Time [sec]	Observation Date
CQ 001035.57-070232.2	00:10:35.57	-07:02:32.29	NOT	2×50.0	2021-08-03T04:45:43.675
CQ 003236.58-091026.2	00:32:36.58	-09:10:26.21	NOT	4×15.0	2021-08-03T04:39:08.784
CQ 010930.72-071931.1	01:09:30.72	-07:19:31.17	NOT	2×300.0	2021-08-03T03:04:21.733
CQ 014434.15-014830.4	01:44:34.15	-01:48:30.44	NOT	2×700.0	2021-08-03T03:28:21.817
CQ 235544.91-192524.5	23:55:44.91	-19:25:24.59	NOT	2×300.0	2021-08-03T02:47:51.808
CQ 014541.50-163419.2	01:45:41.50	-16:34:19.27	NOT	2×250.0	2021-08-03T04:56:56.271
CQ 022742.93-173121.5	02:27:42.93	-17:31:21.54	NOT	2×600.0	2021-08-05T04:53:35.212
CQ 234859.52-193324.89	23:48:59.52	-19:33:24.89	NOT	2×500.0	2021-08-05T03:06:29.480
CQ 000404.29-135905.43	00:04:04.29	-13:59:05.43	NOT	2×500.0	2021-08-05T02:40:46.006
CQ 003635.12-140917.41	00:36:35.12	-14:09:17.41	NOT	2×500.0	2021-08-05T03:57:54.109
CQ 234530.53-135734.65	23:45:30.53	-13:57:34.65	NOT	2×500.0	2021-08-05T02:17:01.273
CQ 010013.02+280225.8	01:00:13.02	+28:02:25.84	NOT	2×600.0	2021-08-07T02:47:54.461
CQ 010339.41-132238.91	01:03:39.41	-13:22:38.91	NOT	2×500.0	2021-08-07T03:13:43.075
CQ 012813.63-120319.79	01:28:13.63	-12:03:19.79	NOT	2×300.0	2021-08-07T03:38:32.828

2.1.2 Visibility plots

After selecting the targets we want to observe, we need to arrange the time to observe them since the time is tight and the targets can rise in the sky at different times due to their different coordinates. Thus, the observing schedule is made according to the best observable time of the targets with some concession, with the help of [visibility plots](#). Particularly in our case, the visibility of targets is also restricted by the telescope itself. For example, the target's altitude should exceed the NOT lowest limit for observing, while the possibility of a closed lower hatch that may alter the observing window due to the potential strong wind should also be taken into account. Besides, Moon gives significant rise to the brightness of UV and optical band, so it produces disturbance to our observation when it is not the target. The moon coordinate is also shown in the visibility plots, and one must make sure the object is not close to the moon. Fortunately, our observation nights are during the period of the new moon and crescent, so the influence of the moon is minimized. One visibility plot as an example is presented in Fig. 2.1. As we can see in Fig. 2.1, all the targets can rise to a fairly high altitude in the late night, which is exactly our arranged observation time on that day, and a high

altitude makes it much easier and better for observation. This is also the reason why we scheduled these targets for August 2nd.

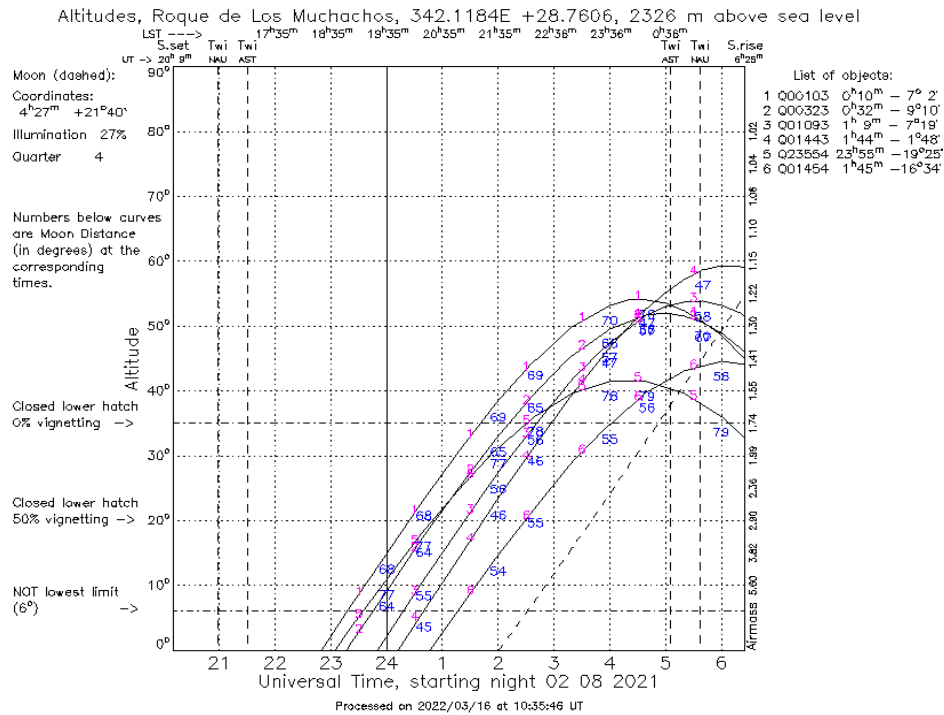


Figure 2.1: The visibility plot of targets for our observing block on August 2, 2021.

2.1.3 Instruments and filters

Another thing we need to consider is what equipment we want to use for observation. There are usually several facilities or cameras in one telescope, which may be applicable to different circumstances or scientific purposes. For instance, there are ALFOSC, The high-resolution Fibre-fed Echelle Spectrograph (FIES) and many other instruments in the NOT, which may have different wavelength range and resolution. We chose to use ALFOSC because it's capable of observation of faint objects, like our targets, quasars, which are faint due to their large distance from us. Besides, compared to other instruments in the NOT, ALFOSC is mainly used for UV-optical spectroscopy which is commonly used in quasar spectroscopy, and it can cover a larger wavelength range, which can maximize the possibility of including obvious emission lines of quasars in our spectra, to make sure we can find out the redshifts of them (the method to determine the redshift of the quasar is introduced in Sect. 4.3). Although it has a lower resolution, it's enough and adequate for our research, while for the high-resolution spectroscopic instrument like FIES, it has low UV sensitivity, because of the inevitable Rayleigh scattering losses in the long fiber, and it's also impossible to apply long-slit spectroscopy in FIES, which is the method that we were going to use in ALFOSC.

In spectroscopy, we also need the instrument called grism, which is simply a combination of a prism and grating, to disperse the light of the spectrum from red to blue wavelengths. Thus, among the grisms provided in ALFOSC, we chose grism 4 (3200-9600 Å) and grism 19 (4400-6950 Å), to make the spectra cover a wide wavelength range and get a better optical resolution for several objects. For grism 4, a 2nd-order blocking filter called WG345 356_LP is used at the same time, because grism 4 can cause substantial 2nd-order effects in the spectra. In addition, we chose the slit_1.0 (with the width of 1.0 arcsecond) for the long-slit spectroscopy, to make sure we can get a relatively high resolution and signal intensity in the meantime.

2.1.4 Exposure time

The exposure time is a key aspect that we also need to consider. We have already known what we will observe, when we will conduct the observation, what instruments we want to use, and then we should know how long we are going to observe for each of the targets. Ideally one wants a long enough exposure time for very smooth and clear spectra of targets (with an extremely high Signal-to-Noise Ratio (SNR)), but our observation time is limited and an adequate SNR is preferable. Moreover, a very long exposure time can also cause a saturation problem in the camera. When the exposure time is too long, the CCD sensor can be over-exposed because each pixel can only hold finite charges, which is called full well capacity, and the charge transfer speed is also finite. Once the full well capacity is reached, accumulation of excess photoelectrons can give rise to overflow or leaking of the additional electrons to the adjacent pixels, creating an artifact. Besides, any pixel which produces more electrons than can be represented by the output signal from the A/D converter (introduced in Sect. 3.1.2) can get saturated as well (see [Howell 2006](#)).

In addition, even though the pixels are not saturated, the relationship between detected photons and converted output signals can still become nonlinear if the pixel values are very high, making the data unusable, as shown in Fig. 2.2.

Thus, deriving appropriate exposure times for different targets is very important. An appropriate SNR depends on your scientific purposes. If you just need to classify the objects like potential stars, galaxies, or whatever else, an SNR around 3 is actually enough. But if you want to research the emission features or especially the properties of absorption lines, a higher SNR should be required and an SNR about 10 or greater is usually considered to be good enough for such purposes.

We are interested in the detailed aspects of quasars, which need a high SNR to be

evaluated, and in general, we want a longer exposure time for fainter objects naturally, to make sure enough photons can hit the CCD sensor. As a result, for faint objects such as quasars, a long exposure time is expected. With the help of the [Exposure time calculator](#) in the ALFOSC page, we determined the exposure time for every target as listed in Table 2.1. One may notice that all the quasar candidates are observed multiple times, which is because the required exposure times of them are actually quite long, and to prevent the saturation of the CCD, we can divide the total time into several pieces, normally in two parts. Apart from the saturation concern, making extremely long exposures is not a good choice also because of the imperfect telescope tracking, possible change in focus, or weather conditions like the seeing, potential failure of instrument, or the accumulation of lots of cosmic ray hits. Later we can combine them together in the processing procedure, to get the same SNR as the figure could have if observed in one shot.

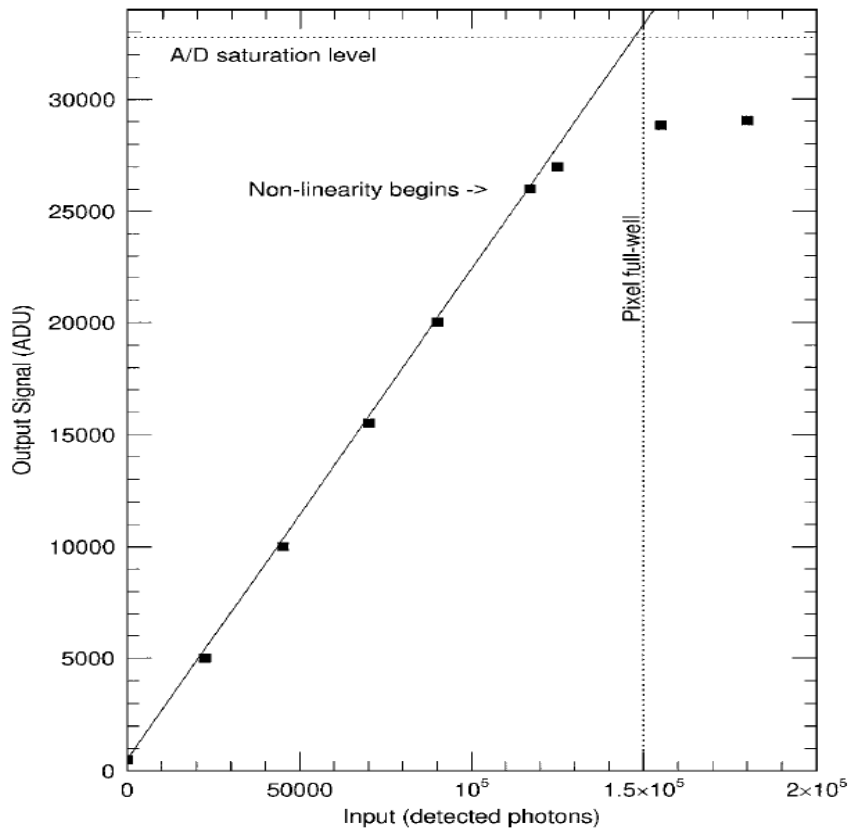


Figure 2.2: A typical CCD linearity curve from [Howell \(2006\)](#). The ratio of the output to the input of the device is constant over the output signal range from 500 ADU (an intrinsic bias level of the CCD) to roughly 26000 ADU, which is less than the A/D saturation level, and the corresponding detected photons are also less than the full well capacity. It means that the device becomes nonlinear before it's saturated. Therefore, the largest usable output ADU value is limited by the CCD nonlinearity.

2.2 Observation

In the summer school, we got 13 hours in total for observation, during which we successfully obtain some scientific images of different galaxies and planetary nebulae, spectra of elliptical galaxies in order to deduce their rotation curves and the dark matter content, as well as the spectra of 14 quasar candidates.

2.2.1 Observation process

On the night of August 2nd, our observation time was scheduled between 02:30 - 05:00 UT (on August 3rd). The seeing was below 1 arcsecond for the whole time and the wind was mild, and we were able to observe all of our planned targets. Thanks to other teams as well, who helped to make bias frames (introduced in Sect. 3.1.4) and flat field frames (introduced in Sect. 3.1.5) at dawn and twilight, and also thanks for their help in observations of several quasar candidates due to the limitation of the observation time of our team.

On the 4th of August, we had the whole observation night from 21:30 to 05:00 UT. We started by making flat field frames and bias frames in the twilight. The twilight time was fairly short and for a while, the sky was too bright that even the narrowband filters were saturated in one second. We ended up almost running out of time for measuring the flats - but we managed just in time. On this night the wind picked up a lot and for the first 4 hours of our actual observing time, the wind speed was above 12 m/s. This meant that the lower hatch of the NOT had to be raised up and we, therefore, had to discard our first imaging target. The wind speed flickered around 15 m/s which meant we also had to point the telescope at least 85 degrees away from the wind direction, further limiting our options for targets. The seeing was around 2-4 arcsec due to the strong wind, which made imaging a bad option and we instead started with monitoring for another science group which consisted of spectroscopy. After this, we spent our time finding more targets for spectroscopy since most of our early evening targets were planned to be imaging, because of which we took spectra of two new supernovae and a nova. We also made it to measure the rotation curves of several galaxies by obtaining their spectra. Around 1 am UT the wind speed decreased significantly to less than 5 m/s, and the seeing became less than 1.5 arcsec for the rest of the night, which was finally better for observation. So we could go back to our scheduled targets for imaging and 5 quasar spectra and ended up with no accident.

August 6th is our last observation night. We did our observation from 02:30 to 05:00

UT. The seeing was below 1" with low wind. We took spectra for 3 quasars, an elliptical galaxy, and an image of a globular cluster.

2.2.2 Observed targets

By connecting to the NOT FTP, we easily downloaded our raw data, and I also got 37 extra spectra (one additional observation to CQ 234530.36-135743.3 in the infrared with GTC) from my supervisor Johan, for further analysis. All the targets which are observed and investigated in this thesis are listed in Table 2.2.

Table 2.2: The full sample of observed 50 quasar candidates.

Target	RA (J 2000) [hr : min : sec]	Dec (J 2000) [deg : min : sec]	Telescope	Exposure Time [sec]	Observation Date
CQ 001035.57-070232.2	00:10:35.57	-07:02:32.29	NOT	2×50.0	2021-08-03T04:45:43.675
CQ 003236.58-091026.2	00:32:36.58	-09:10:26.21	NOT	4×15.0	2021-08-03T04:39:08.784
CQ 010930.72-071931.1	01:09:30.72	-07:19:31.17	NOT	2×300.0	2021-08-03T03:04:21.733
CQ 014434.15-014830.4	01:44:34.15	-01:48:30.44	NOT	2×700.0	2021-08-03T03:28:21.817
CQ 235544.91-192524.5	23:55:44.91	-19:25:24.59	NOT	2×300.0	2021-08-03T02:47:51.808
CQ 014541.50-163419.2	01:45:41.50	-16:34:19.27	NOT	2×250.0	2021-08-03T04:56:56.271
CQ 135305.76+255429.2	13:53:05.76	+25:54:29.28	NOT	2×500.0	2021-08-03T21:56:06.531
CQ 022742.93-173121.5	02:27:42.93	-17:31:21.54	NOT	2×600.0	2021-08-05T04:53:35.212
CQ 234859.52-193324.89	23:48:59.52	-19:33:24.89	NOT	2×500.0	2021-08-05T03:06:29.480
CQ 000404.29-135905.43	00:04:04.29	-13:59:05.43	NOT	2×500.0	2021-08-05T02:40:46.006
CQ 003635.12-140917.41	00:36:35.12	-14:09:17.41	NOT	2×500.0	2021-08-05T03:57:54.109
CQ 234530.53-135734.65	23:45:30.53	-13:57:34.65	NOT	2×500.0	2021-08-05T02:17:01.273
CQ 010013.02+280225.8	01:00:13.02	+28:02:25.84	NOT	2×600.0	2021-08-07T02:47:54.461
CQ 010339.41-132238.91	01:03:39.41	-13:22:38.91	NOT	2×500.0	2021-08-07T03:13:43.075
CQ 012813.63-120319.79	01:28:13.63	-12:03:19.79	NOT	2×300.0	2021-08-07T03:38:32.828
CQ 015957.91-061052.2	01:59:57.91	-06:10:52.22	NOT	2×700.0	2021-08-21T02:49:00.218
CQ 000049.99-044426.6	00:00:49.99	-04:44:26.61	GTC	2×800.0	2021-08-17T04:37:20.359
CQ 000337.27-004228.9	00:03:37.27	-00:42:28.97	GTC	2×1000.0	2021-08-18T05:16:10.326
CQ 000455.89-004515.1	00:04:55.89	-00:45:15.19	GTC	2×800.0	2021-08-16T05:17:21.653
CQ 000625.41-041003.7	00:06:25.41	-04:10:03.75	GTC	2×1000.0	2021-08-18T04:03:24.729
CQ 000822.07-002302.7	00:08:22.07	-00:23:02.77	GTC	2×400.0	2021-08-12T05:12:08.488
CQ 003859.56+021008.2	00:38:59.56	+02:10:08.23	GTC	2×1350.0	2021-08-17T05:18:54.965
CQ 132930.98+282538.3	13:29:30.98	+28:25:38.35	GTC	2×1150.0	2021-08-04T21:23:55.762
CQ 133639.96+282502.2	13:36:39.96	+28:25:02.27	GTC	2×900.0	2021-08-14T21:48:00.578
CQ 134053.89+145853.7	13:40:53.89	+14:58:53.77	GTC	2×300.0	2021-08-11T21:53:53.331
CQ 140513.29+060902.2	14:05:13.29	+06:09:02.28	GTC	2×300.0	2021-08-11T22:06:55.757
CQ 230007.30-181651.6	23:00:07.30	-18:16:51.64	GTC	2×1000.0	2021-08-17T02:54:10.948
CQ 231242.04-083700.8	23:12:42.04	-08:37:00.82	GTC	2×600.0	2021-08-12T01:56:02.475
CQ 231423.51-094732.6	23:14:23.51	-09:47:32.66	GTC	2×600.0	2021-08-13T00:05:54.264
CQ 232821.99-063025.2	23:28:21.99	-06:30:25.25	GTC	2×600.0	2021-08-14T02:40:20.633
CQ 234610.32-014557.5	23:46:10.32	-01:45:57.57	GTC	2×1000.0	2021-08-19T05:28:53.935
CQ 234744.54-104255.8	23:47:44.54	-10:42:55.89	GTC	2×720.0	2021-08-17T03:28:34.332
CQ 234930.46-053817.7	23:49:30.46	-05:38:17.70	GTC	2×600.0	2021-08-17T03:56:16.502

Table 2.2: *Continued.*

Target	RA (J 2000) [hr : min : sec]	Dec (J 2000) [deg : min : sec]	Telescope	Exposure Time [sec]	Observation Date
CQ 235140.03-011330.5	23:51:40.03	-01:13:30.54	GTC	2×600.0	2021-08-13T05:01:34.073
CQ 235807.91-011943.3	23:58:07.91	-01:19:43.35	GTC	2×500.0	2021-08-13T05:38:27.905
CQ 005406.43-100002.6	00:54:06.43	-10:00:02.66	GTC	2×900.0	2021-07-30T05:05:04.427
CQ 010002.00-030856.7	01:00:02.00	-03:08:56.76	GTC	2×800.0	2021-08-02T03:23:10.417
CQ 231904.59-073841.6	23:19:04.59	-07:38:41.61	GTC	2×800.0	2021-07-30T04:20:11.817
CQ 234530.36-135743.3	23:45:30.36	-13:57:43.3	GTC	2×1000.0	2021-08-18T03:16:02.137
CQ 003634.82-081425.8	00:36:34.82	-08:14:25.85	NOT	2×900.0	2021-12-31T20:03:51.692
CQ 005258.35-052240.2	00:52:58.35	-05:22:40.29	NOT	2×900.0	2022-01-01T21:54:50.230
CQ 021725.85-144057.31	02:17:25.85	-14:40:57.31	NOT	2×900.0	2021-12-31T21:00:45.567
CQ 115341.57+060815.5	11:53:41.57	+06:08:15.56	NOT	2×900.0	2022-01-03T04:45:27.794
CQ 121020.98+142958.5	12:10:20.98	+14:29:58.55	NOT	2×600.0	2021-12-31T05:37:35.374
CQ 124154.87+255632.5	12:41:54.87	+25:56:32.57	NOT	2×900.0	2022-01-03T05:23:35.917
CQ 130022.82+241136.1	13:00:22.82	+24:11:36.16	NOT	2×900.0	2022-01-03T04:09:08.178
CQ 131117.99+314715.4	13:11:17.99	+31:47:15.43	NOT	2×900.0	2022-01-02T05:34:38.978
CQ 131919.56+115251.9	13:19:19.56	+11:52:51.95	NOT	2×900.0	2022-01-03T06:37:25.558
CQ 235600.19-073716.0	23:56:00.19	-07:37:16.08	NOT	2×600.0	2022-01-02T20:39:28.697
CQ 235954.08-124150.58	23:59:54.08	-12:41:50.58	NOT	2×450.0	2021-12-30T19:45:22.935
PSS J0141+3334	01:41:32.79	+33:34:24.69	NOT	2×900.0	2022-01-01T22:46:44.349

Chapter 3

Data Processing

After we get the raw data of the spectra, it's not a wise choice to utilize and analyze them immediately since there are lots of noise and different influences from many sources, such as the device or the sky. Only after processing the raw spectra can we use them for scientific purposes. The way to get rid of most of the noise and perform the calibration of the data is described in the following sections. This chapter is based on the book by [Howell \(2006\)](#), the course literature of Astronomical Data Processing by Prof. Lise Bech Christensen ([Christensen et al. 2019](#)), and the Python scripts¹ by Johan and Prof. Kasper Elm Heintz.

3.1 Data Reduction

3.1.1 Fundamental theory

In general, raw data can be reduced in a way as described in eq. (3.1) from [Christensen et al. \(2019\)](#), which is applicable to both astronomical images (photometry) and spectra (spectroscopy), but we will just focus on the processing of spectra here.

$$\text{Reduced spectrum} = \frac{(\text{Raw spectrum} - \text{Master Bias})}{\text{Normalized Flat}} \quad (3.1)$$

'Raw spectrum' in eq. (3.1) refers to the output of the target observed by the telescope, one example of which is shown in Fig. 3.1. As we can see, the raw spectrum of the object is very faint and not really usable for research without reduction, as stated above, so it's very necessary to process the raw data. 'Bias' refers to bias frames, and 'master bias'

¹<https://github.com/keheintz/PyReduc>

represents the combined bias frame, which is explained in Sect. 3.1.4. 'Flat' refers to flat field frames, which will be illustrated in Sect. 3.1.5. We reduced the spectra in such a way to get rid of the noise from the device and the difference in signal response between pixels, due to the properties of CCDs.

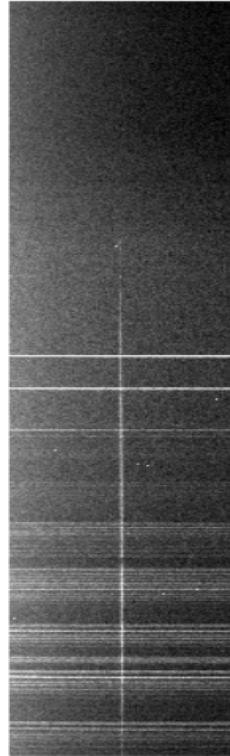


Figure 3.1: A raw spectrum of the target CQ 014434.15-014830.4, in which we can see the horizontal sky emission lines and the vertical line being the spectrum of the object. The spectrum is a bit fuzzy due to the sensitivity difference of the CCD in dissimilar wavelengths and the noise, which is why we need to process the observed spectra first.

3.1.2 Basic knowledge of CCD astronomy

The charge-coupled devices (CCD) are the key facilities that are widely used in modern telescopes for scientific imaging and spectroscopy, including the telescopes we used to get all the spectra (the NOT and the GTC). Because CCDs are the actual receivers of the photon information of targets, to know how we should process the data we receive, we have to know how the receiver, which is the CCD, works at first.

The CCD is a device that can contain and manipulate electrons with a negative charge and holes with a positive charge, which are produced in the CCD when it's exposed to radiation, via the photoelectric effect. This is the reason why the CCD can be used in the telescope as a receiver. The operating principle of the CCD can be easily described by the 'water bucket' idea, which is a very understandable and simple analogy introduced by [Janesick et al. \(1987\)](#).

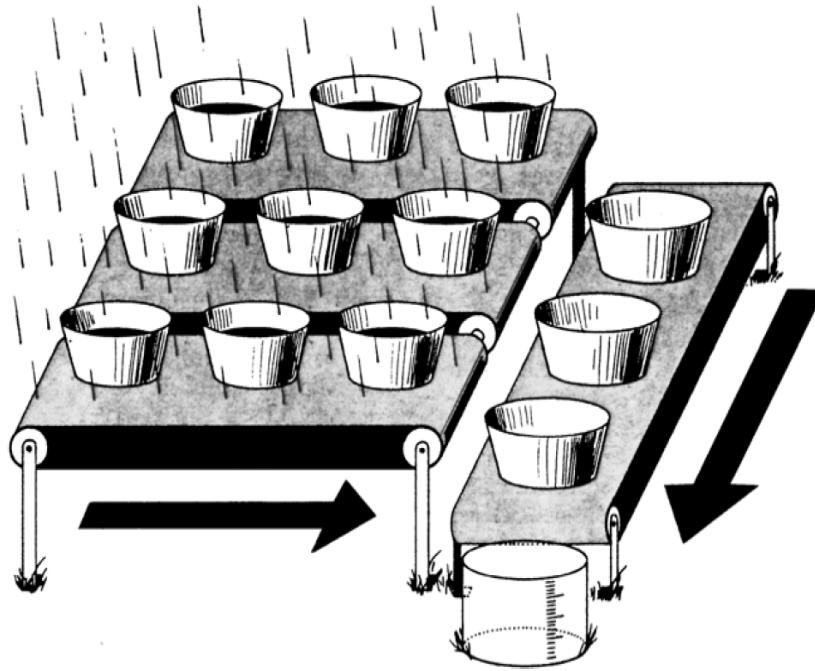


Figure 3.2: An illustration of the 'water bucket' analogy for the operation of CCDs from [Janesick et al. \(1987\)](#).

The buckets in Fig. 3.2 represent the pixels in the CCD, and the raindrops represent the incoming light. All the buckets are aligned in rows and columns to form an array, which shows that the CCD array consists of pixels placed neatly. The exposure process of the CCD is similar to buckets collecting raindrops. When the rainstorm stops (CCD integration is finished), we close the shutter, and each bucket is moved to the measuring spot successively. It's subsequently emptied into the measuring bucket to meter how much water is collected. A two-dimensional record of the rainfall (incoming photons) in the measured area is then produced, which is the final output CCD image.

However, the real circumstance here is a bit different and more complex in fact. For instance, the analog-to-digital (A/D) converters needed for the CCD are not shown in the 'water bucket' idea. The job of the A/D converter is to assign an appropriate digital number to the generated charge value of every pixel because the data which are stored in the computer are digital numbers (in counts or analog-to-digital unit (ADU)), and the output of pixels is actually an analog voltage, which has to be digitized by A/D converters ([Merline & Howell 1995](#)). The way of assignment or conversion is determined by the gain (in electrons/analog-to-digital unit (e^- / ADU)) of the device.

As what is shown by the unit of the gain, gain values indicate how many electrons are needed for one ADU step. Let's assume the gain of one CCD is 5 electrons/ADU, and the function of A/D converters is to divide the number of electrons produced in each

pixel during the exposure, which are related to the incident photon number, by 5. Every time 5 electrons are measured, it will add one to the ADU value, but a question arises here what if there are fewer than 5 electrons left after the division? In general, ADU converters will neglect these electrons and leave them uncounted, so these dozens of electrons become unknown to the output pixel value and are lost in our observation. It can induce severe problems that the uncertainty of the output image can be very large, and what's more terrible is that we don't even know what the value of error can be.

Thus, the gain of a device can influence the quality of output photometric information significantly and the lower gain value is what we are trying to achieve for telescopes (see [Howell 2006](#)). For all the images we got from the NOT and the GTC, the gain is around 0.16 and 0.95 electrons/ADU. Besides, the processing speed of pixel examination and A/D conversion determines the actual readout speed of the CCD, which can be related to the saturation problem as described in Sect. [2.1.4](#).

3.1.3 Readout noise

We have discussed what CCDs are and how they work, but it's not enough for us to know how to process the output data from CCDs. To achieve this goal, we also need to learn about the properties of CCDs and the first thing we want to talk about is the readout noise (RON).

Readout noise, as we can see from its name, it's the noise introduced when reading out the CCD, which means that several extra electrons can be produced in each pixel and included in the final output signal every time after the readout. It's an inherent noise that is created by the A/D converters and all the output electronics themselves. When converting an analog signal to a digital value, some statistical distribution around the optimal mean digital number will be inevitably generated by the A/D circuit, making the conversion unrepeatable. Besides, all the used electronics can produce spurious electrons while working, bringing random fluctuation into the output. The combination of these two fluctuations gives rise to additional uncertainty in the output, and the average of the uncertainty (one sigma) is the RON.

The RON used to be a big problem in the old telescopes, which can reach 100 electrons per pixel or even more. However, for modern telescopes with more advanced CCDs, the RON becomes only a few electrons per pixel, making it hardly the dominant noise for bright sources. However, when researching faint objects such as some of the quasars, the RON should not be ignored. The RON can be calculated as described by eq. [\(3.2\)](#) from [Howell \(2006\)](#),

$$RON = \frac{Gain * \sigma_{Bias_1 - Bias_2}}{\sqrt{2}} \quad (3.2)$$

which means that the RON is determined as the standard deviation of the difference between two bias frames, while the digital numbers in the bias frames should be converted to electrons, so an extra gain is multiplied. The typical RON of the telescopes we used is about 4.3 electrons per readout time.

3.1.4 Bias frame

As bias frames are mentioned frequently, one must be curious about what bias frames are. Bias frames or images are the first CCD images taken during an observation, with a zero-second exposure time and closed shutter, which are read out immediately and can be used to determine the zero noise level of CCDs as indicated by eq. (3.2). Ideally, for an unexposed image, a zero output value is expected, but in reality, there are readout noise and noise from A/D conversion, which will make the output value become a distribution around the mean value of zero. However, the negative value is not allowed in the CCD output, so to keep the output value positive, we add an artificial offset level to the CCD. The electronically added offset value is the so-called bias level, becoming the new 'zero' level, which can typically be 100 - 1000 ADU per pixel (Christensen et al. 2019). The bias level can be determined by using the mentioned bias frames, or the overscan region.

The overscan region is a few additional rows or columns (in general it's 32), added to every image automatically. These rows or columns are not physically existing in the CCDs themselves, but they are just extra pseudo-pixels produced by the device to evaluate the bias level, which is the mean value of every pixel in the overscan region. By subtracting the single mean value from each pixel in the CCD output image, we can get the real output values referencing the real zero level, without the bias offset. However, because of the influence of CCD amplifiers and readout noise, there can be a little spatial variation in the bias level, while the overscan region can't help us reduce such noise and spatial structure in the output image. Thus, bias frames are needed not only for determining the offset bias level, which is constant for some CCDs, but also for finding out the variance in the bias level.

However, to get the spatial variation, a single bias image is not enough. For the statistical reason, to sample all the variations well in the CCD output image, we need at least 10 bias frames or more, synthesizing which to be a master bias (Gilliland 1992).

Combining multiple bias frames can also help to limit adding extra noise to our science data during reduction, by increasing the signal-to-noise ratio to reach good statistics. In our reduction process, nearly 50 data frames are combined to make the master bias.

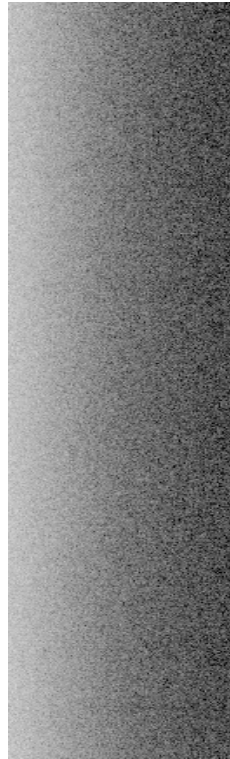


Figure 3.3: A master bias frame used for spectroscopic reduction.

The way to combine all the bias frames has to be considered. It's usually done by taking the average or median of all the frames. What we did is taking the average value of all the pixels in the overscan region of each bias frame separately to get the bias level in every single image, and subtracted the corresponding mean bias level from each image to set all the bias frames to the true zero level reference. Then all the values of pixels in every bias frame are distributed around zero in a Gaussian shape, from which we can measure the noise level in the images by combining all of them. To get rid of the possible influence of cosmic rays, random perturbations and noise variations, we chose to take the median value of each pixel in all the 50 bias frames to get one final master bias. One should be noted that cosmic rays can be radiation from the radioactive materials embedded in CCDs, not necessarily be cosmic ([Florentin-Nielsen et al. 1995](#)). In addition, the master bias frame for spectroscopy is different from that for imaging, but only in the size of them, simply due to windowing of the detector in spectroscopy. Because the entire information of a long-slit spectra can be represented by a central fraction of the whole CCD image, we don't need that big area of the whole CCD. Moreover, to decrease the readout time and ease the reduction process (fewer pixels are needed to be reduced and calibrated), it's a wise choice to merely read out

the central part of the CCD (usually 500 columns), which is the so-called technique, 'windowing'. It's not a real window which appears above the CCD to limit the incoming light. One example of a master bias frame used in spectroscopy is shown in Fig. 3.3.

3.1.5 Flat field frame

As shown in eq. (3.1), in addition to bias frames, we also need to know another jargon that is related to the spectra reduction, which is the flat field frame. It's also a kind of image taken before or after our observation, but different from the zero exposure time of bias frames, it's taken in a short exposure time to prevent possible saturation of the CCD, with the open shutter, pointing towards an evenly illuminated surface. Such evenly illuminated surface can be the sky during twilight or dawn, a bright spot inside the telescope dome when it's illuminated by a light source, or mounted lamps for spectroscopy. What we used is the dusk sky for imaging, to fully utilize the time before the dark night which is suitable for scientific observation, and the Halogen lamp mounted inside the dome with the same setup as used for scientific targets (slit_1.0, detector windowing, grism 4 or 19 and corresponding filter) for spectroscopy. Due to the dusk sky's bright nature, the exposure time is typically around 2 seconds, which can be adjusted automatically by the programs of the telescope themselves, and the exposure time of mounted lamps with different grisms used for spectroscopy is suggested in advance by the telescope manual (e.g. [Overheads at the NOT](#)).

The reason why we need the flat field frame is very simple, which is that actually, every pixel in the CCD has a slightly different response. In other words, the properties of pixels, like the gain, are all not exactly the same, which can be expected because we are not able to produce CCDs perfectly (Howell 2006). Thus, to manually correct for such differences and flatten the relative response, the flat field frame is created to perform such calibration. Besides, because the response difference depends on the spectral distribution of the incoming light, flat field frames should be taken separately when observing in different wavelength ranges, or using different filters. Particularly in spectroscopy, different flats are needed when using different grism, and we can't use the sky for the flat calibration of the spectroscopy, since there are air emission and absorption lines in the atmosphere, and such lines will appear in the flat frames when using grisms. Therefore, we chose to use the Halogen lamp installed in advance, which is a black body emitter, producing a continuum with a usable wavelength range from around 300 nm to 3000 nm (the range depends on the color temperature).

In practice, similar to bias frames, we need multiple flat field frames to reach good statistics and limit adding random noise, and the number of needed flats can be less,

but at least 5 frames are required. However, before combining them directly, there are a few more steps we need to take. First, flat frames are obtained from the CCD, so they also contain the bias level and noise considered in Sect. 3.1.4. The solution is also similar to that in Sect. 3.1.4, which is that we can use the overscan region in each flat frame to get the bias level, and simply subtract the master bias frame created in Sect. 3.1.4 from every flat frame. Second, we are aiming to correct the variations in the sensitivity of each pixel in the CCD, so for a given incident flux, the pixel values should be ideally the same after correction, reflecting the same signal. It should be a kind of relative correction between pixels and we just want the final master flat to reflect the relative response difference between pixels. Thus, the pixel values fluctuating around 1.0 and with a median of 1.0 are expected, which means that we need to normalize each flat frame before combining them together and do the same after the combination. Moreover, the intensity levels of flats are normally very high (around 20,000 ADU), so we normalize the flat frames before applying them to science data to get good statistics (Christensen et al. 2019).

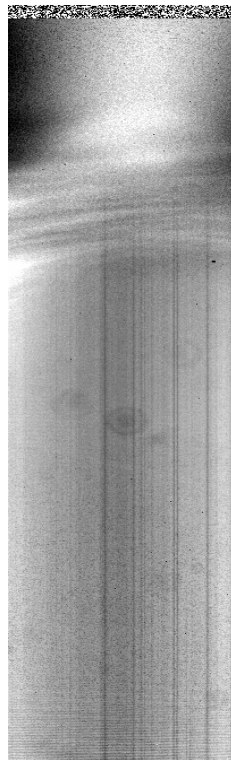


Figure 3.4: A master flat field frame used for spectroscopic reduction.

The way we perform the normalization is to divide each pixel of the entire flat image by the median of it. We choose the median not the average for a similar reason to that presented at the end of Sect. 3.1.4, to avoid the influence of possible cosmic ray hits and for the sky flat frames of imaging, it can help to remove the possible presence of stars in the image. There are some more details that one needs to pay attention to. As

shown in Fig. 3.4, for the existence of the overscan region in the top several rows in flat frames, if we simply obtain the median of the whole image, the zero values after bias correction can inevitably influence the result, although not as significantly as getting the mean value. Besides, one may notice that there is a clear distinction between the much more uniform area at the top and the rest majority of the image with vertical stripes at the bottom. Such significant difference is mainly caused by the 2nd-order blocking filter mentioned in Sect. 2.1.3, which basically filters out all the light with wavelengths shorter than 300 nm, plus the low sensitivity of the CCD and grisms to the UV light in the blue end, making the top regions very uniform and actually unusable for scientific purpose, and we will cut them off when making the science images. Therefore, we also need to discard these pixels to prevent them from affecting our normalization process of flat frames.

First, What we need to do is to only select the central bottom region in the flat image, but as big as possible, to be statistically good and avoid including the edges which may give bad values. Second, take the median of the pixels' value in the selected region as the normalization coefficient. Third, divide all the pixels in every single flat field frame by the corresponding normalization coefficient and combine all of the normalized flat images together by their median again. We can stop here if we are making master bias frames as described in Sect. 3.1.4, but more need to be done when making master flat frames, which is to normalize the master flat frame once again.

During synthesis, some noise can be introduced inevitably, making the average value of all pixels no longer 1. This time, we normalize the master flat frame column by column since we can utilize as many useful pixels as we can to fulfill better statistics in this way. We can do such an operation in this step because we have excluded the possible outliers in the previous combination process. Thus, we divide columns by the mean value of the whole master flat frame, and the reason why we don't perform it pixel by pixel is that there is an intrinsic sensitivity difference depending on the wavelength (aligned on the column) in CCDs, and we want to keep this feature because we can correct such sensitivity distinction when dividing our science image by the master flat frame, without adding any artificial effect. In such a manner, we can get a desired normalized master flat frame as shown in Fig. 3.4, which can be used in eq. (3.1).

3.1.6 Dark current

In fact, there used to be another thing that is a concern during astronomical data reduction, which is the dark current. The dark current is the intrinsic thermal signal in CCDs,

which is the thermal noise that every material will suffer from if it's at a temperature exceeding absolute zero. The dark current electrons will be read out together with the signal during readout, becoming identical to the science signal and impossible to be separated from photoelectrons. In the past, such dark current has to be measured with exposure time over 0 seconds and a closed shutter. However, the dark current becomes extremely insignificant for modern CCDs, which equals a level of approximately 2 - 10 electrons/pixel/hour (Christensen et al. 2019). Thus, for each of our observations with less than 20 minutes of exposure time, the dark current can be neglected obviously. We don't include the dark current in eq. (3.1) for such reason, but the dark current should be considered in the infrared observations.

3.2 Spectral Calibration

We can get the reduced science image, which refers to the reduced spectra here in our thesis, following the strategy as stated in eq. (3.1). one needs to remember to remove the possible cosmic-ray hits in the raw science images at the beginning of the reduction process simply by sigma clipping. Besides, as mentioned in Sect. 2.1.4, we need to combine multiple reduced science images into one 'master' image for our analysis, to reach a desired and optimal SNR. At the same time, we should be careful that the locations of the target's spectra on the detector are usually different, which are typically offset slightly in position from one another, to avoid the influence of possible bad pixels on the CCD. Thus, we need to align and match the spectra properly, which is the horizontal bright line in Fig. 3.5. One example of the 'master' spectrum of CQ 014434.15-014830.4 is shown in Fig. 3.5. You may notice that the spectrum of the target is much brighter and more obvious now than that shown in Fig. 3.1 before reduction, which shows how significantly the quality of spectra can be improved after processing. Besides, the spectrum is also rotated 90 degrees anticlockwise, making the blue part of the spectrum situate on the left-hand side and red on the right, which is corresponding to the fact that blue light has a shorter wavelength. Doing such rotation can make the following steps much easier.

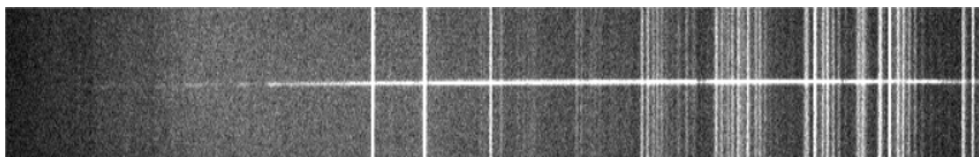


Figure 3.5: A 'master' spectrum of the target CQ 014434.15-014830.4, in which the horizontal bright line is the spectrum of CQ 014434.15-014830.4. The vertical narrow lines are the atmospheric emission lines, which are subtracted later as described in Sect. 3.2.2.

3.2.1 Wavelength calibration

It's enough to stop here for imaging processing, but more need to be done when we are working on spectra. First, the units of the x-axis and y-axis are both pixel numbers in Fig. 3.5 for instance, while the x-axis represents the wavelength of the spectrum and the y-axis shows the spectrum's spatial location on the detector. It's kind of comprehensible if the location of the spectrum is in pixels, but it doesn't make any sense if the wavelength is described in pixels. Thus, after we get the reduced two-dimensional (2D) spectrum, we ought to correlate the pixel numbers on the x-axis with wavelengths. For this reason, images are taken in advance by illuminating the CCD with the HeNe lamp or ThAr lamp and the same setup as our observations, which can then be used for wavelength calibration (the details on arc lamps used in the NOT can be found in [ALFOSC Arc Lamps](#)). Based on the fact that we know the wavelength of He and Ne emission lines, we can easily find the pixel values and their corresponding wavelengths. Such correlation of pixel numbers and wavelengths must be consistent because we are using the same grism and CCD for the observations and the arc images. In this way, the wavelength problems on the 2D spectrum are solved by fitting a Chebyshev polynomial with known arc maps (can be found in [ALFOSC Arc Lamps](#)), for more details see the [identify.py](#) made by Johan and Kasper. Besides, one should be noted that the arc images should also be reduced in the same way as described by eq. (3.1).

3.2.2 1D spectra extraction and sky background subtraction

Now we have the 2D spectra in pixel values correlated with wavelengths on the x-axis. However, the modern spectra we use for research are usually one-dimensional (1D). It is easy to measure the flux and appearance of emission or absorption lines in this 1D format, which is very crucial in spectra analysis. Therefore, what we need to do is extracting the 1D spectra from the 2D images.

In the meantime, there are also emission lines from the particles and molecules in the atmosphere on the 2D spectra, which are called sky emission lines, appearing as the vertical lines in Fig. 3.5. The common sky emission lines are oxygen lines at 5577 Å, 6300 Å, and 6364 Å ([Christensen et al. 2019](#)), for instance. They can influence our measurement of flux in the spectra later in the Sect. 3.2.3, so we need to subtract them while extracting the 1D spectra, and it's very easy and feasible to do so. One can just slice the 2D spectrum perpendicular to the object (along the y-axis), and then determine the object position and the region you want to use to calculate the sky background, as presented by Fig. 3.6.

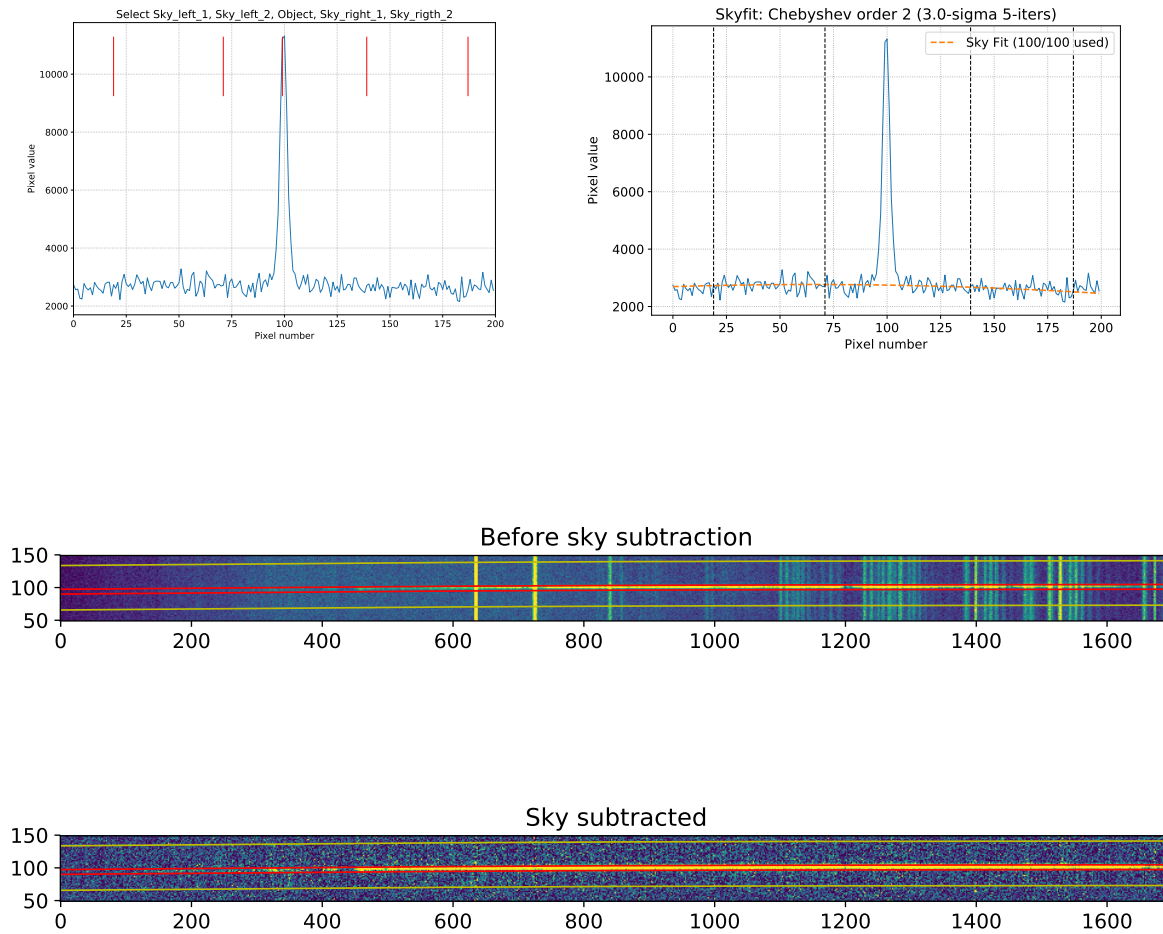


Figure 3.6: The sky subtraction process of CQ 014434.15-014830.4. The top left panel shows the step when we select the sky region with the object in the center. Note that the selected sky regions ought to be as large as possible while they should be far enough from the central object. The bottom two figures show the 2D spectrum before and after sky subtraction as indicated by the titles.

Afterward, slice the 2D spectrum along the spectrum of the object (the horizontal central line along the x-axis) and subtract the data counts at every wavelength (x-axis) with the corresponding values of sky background calculated as the mean of the pixels' values in the selected sky regions (y-axis). As a result, we can get the sky subtracted 1D spectrum. The entire process is realized with [extract_1d.py](#) made by Johan and Kasper, and diagrams in Fig. 3.6 are screenshots of the program's output.

3.2.3 Flux calibration

What we get now is the 1D spectra with wavelengths on the x-axis. However, on the y-axis, the intensity of the spectral energy distribution is given by the ADU, which we can't use for scientific purposes, as displayed in Fig. 3.7.

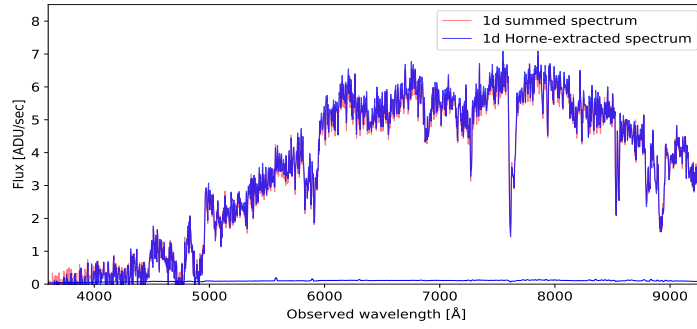


Figure 3.7: The extracted 1D spectrum of CQ 014434.15-014830.4 with flux described in ADU, produced with [extract_1d.py](#) by Johan and Kasper.

Therefore, the final step is to calibrate the spectra with the standard star. Because we know the accurate AB magnitudes of standard stars at each wavelength, by taking the spectrum of standard stars, we can know the correlation between the counts of CCD (in ADU) and the flux (in $\text{erg}/\text{s}/\text{cm}^2/\text{\AA}$) of the object at each wavelength in the spectrum. The flux can be converted from the AB magnitudes in the following way,

$$F_\nu = 10^{-0.4 \times (48.60 + m_{\text{AB}})} \quad \text{and} \quad F_\lambda = \frac{F_\nu \times 3.34 \times 10^{18}}{\lambda^2} \quad (3.3)$$

where m_{AB} denotes the AB magnitude, F_ν and F_λ refer to the flux expressed in the frequency and in the wavelength respectively. After we know the relationship between the ADU and the flux in $\text{erg}/\text{s}/\text{cm}^2/\text{\AA}$, we can easily convert the unit of the flux in the 1D spectrum from ADU to $\text{erg}/\text{s}/\text{cm}^2/\text{\AA}$. This step in our thesis is finished with the help of [calibrate.py](#). Note that the spectrum of the standard star should also be processed in the same way as described previously for the science objects. The final spectrum is given in Fig. 3.8.

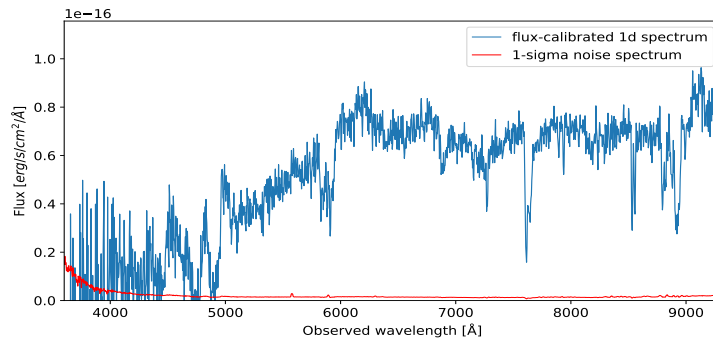


Figure 3.8: The final 1D spectrum of CQ 014434.15-014830.4 with flux described in $\text{erg}/\text{s}/\text{cm}^2/\text{\AA}$, produced with [calibrate.py](#) by Johan and Kasper.

3.2.4 Error propagation

Last but not least, it's very crucial to measure the error levels in the flux of our spectra in the meantime, otherwise, the flux values and the corresponding results can't be trusted. In general, the errors are the uncertainties in our spectra, which are described in standard deviation and usually come from the photon noise, the readout noise, the noise from the bias frames, the noise from the flat frames, the noise from the dark frames (Christensen et al. 2019). However, in our thesis, the dark current is not considered as demonstrated in Sect. 3.1.6. Besides, we will also ignore the noise from the bias frames and the flat frames, since they are too small compared to the photon noise and the readout noise, which can be described by eq. (3.4) and eq. (3.5) from Christensen et al. (2019). Note that the values in the equations are in units of electrons.

$$\text{Var}(\text{bias}) = \sigma^2(\text{bias}) = \sigma^2(\text{DC}) + \left(\frac{\text{RON}^2}{N_{\text{bias}}} \right) K(N_{\text{bias}}) \quad (3.4)$$

$$\text{Var}(\text{flat}) = \sigma^2(\text{flat}) = \frac{\text{RON}^2}{N_{\text{flats}} \bar{F}^2} + \frac{f}{N_{\text{flats}} \bar{F}} \quad (3.5)$$

In eq. (3.4), $\sigma^2(\text{bias})$ denotes the variance of pixel values in the master bias, $\sigma^2(\text{DC})$ refers to the uncertainties in determining the bias DC level, N_{bias} is the number of bias frames we used to composite the master bias, which is 50. $K(N_{\text{bias}})$ is equal to 1 when we combine the bias frames with a geometric average, and converges toward $\sqrt{\pi/2}$ when we median combine the bias frames for $N_{\text{bias}} \rightarrow \infty$ (Christensen et al. 2019). As a result, we can estimate $K(N_{\text{bias}}) = \sqrt{\pi/2}$ for our case and $\sigma^2(\text{DC})$ is considered to be zero for well-behaved CCDs, of which the DC level is normally constant. Thus, the noise from the bias frames is 50 times as small as the readout noise, not to mention the photon noise and we can neglect it without a doubt.

As for the noise from the flat frames, it's far smaller than the readout noise and the photon noise, with \bar{F} being the overall flux level (around 20,000 ADU and hereby 2000 electrons assuming the gain to be 0.1) in the flat frames and f denoting the signal level in the master flat-field in eq. (3.5), which normally equals to 1. Thus, we can omit such errors as well.

The only things we need to consider now are the photon noise and the readout noise. The number of photons with certain energy is theoretically and experimentally governed by the Poisson distribution, which is a common discrete probability distribution.

Poisson statistics has a very special and cardinal property that the variance of any Poisson distributed stochastic variable is always equal to the mean value of it (Jakobsen 2013).

It's also valid for photons. More specifically, the statistical distribution of the expected number of photons with certain energy received by us per unit time, obeys the Poisson distribution. In other words, during an exposure duration, there are uncertainties in the number of photons we collect at a certain wavelength and these uncertainties are described by the photon noise. The flux at each wavelength is then fluctuated by the photon noise since it's proportional to the integrated number of photons with a certain frequency.

Because the number of photons we acquire with our telescopes follows Poisson distribution, it's then rather easy to get the photon noise. As described previously, the variance of the number of photons at a certain wavelength always equals the average number of photons we can receive per unit time, which is calculated quite straightforwardly by dividing the final data counts at every pixel by the exposure time. Note that the final data counts are in units of electrons since only the number of generated electrons in the CCD is correlated with the actual received number of photons, as described in Sect. 3.1.2. This also why we set the units in eq. (3.4) and eq. (3.5) to be electrons.

Therefore, we can determine the variance of photon numbers in units of electrons being $Var(\text{photon}) = N(\text{photon})$, in which $N(\text{photon})$ denotes the number of photons received per unit time expressed in the electron numbers. In addition, the readout noise can add extra electrons to the output every time we read out an image, as what has been described in Sect. 3.1.3. It will influence our measurement of electron numbers at each pixel and further the photon numbers, so it ought to be included in the estimation of photon numbers' variance, while $\sigma(\text{readout}) = RON$.

In conclusion, the variance of photon numbers and hence the variance of flux is described by eq. (3.6),

$$Var(\text{flux})_e = Var(\text{photon})_e = N(\text{photon})_e + (N_{\text{exp}} * RON_e)^2 \quad (3.6)$$

in which all the values are in units of electrons except for N_{exp} denoting the number of exposures (readout times). The last step is to convert them to be expressed in units of ADU with the help of the gain since we need all the values measured in ADU in the flux calibration step as demonstrated in Sect. 3.2.3. Here is the final form of the error we calculate in this work, as given in eq. (3.7),

$$Var(\text{flux})_{ADU} = Var(\text{photon})_{ADU} = \frac{N(\text{photon})_{ADU}}{GAIN} + \left(\frac{N_{\text{exp}} * RON_e}{GAIN}\right)^2 \quad (3.7)$$

where $N(\text{photon})_{ADU} = N(\text{photon})_e / GAIN$. It is derived in the way as described by eq. (3.8), while $Var(\text{photon})_{ADU} = \sigma(\text{photon})_{ADU}^2$.

$$\begin{aligned} Var(\text{photon})_e &= N(\text{photon})_e + (N_{\text{exp}} * RON_e)^2, \\ \sigma(\text{photon})_e &= \sqrt{N(\text{photon})_e + (N_{\text{exp}} * RON_e)^2}, \\ \sigma(\text{photon})_{ADU} &= \frac{\sigma(\text{photon})_e}{GAIN} = \sqrt{\frac{N(\text{photon})_e + (N_{\text{exp}} * RON_e)^2}{GAIN^2}} \quad (3.8) \\ &= \sqrt{\frac{N(\text{photon})_{ADU}}{GAIN} + \left(\frac{N_{\text{exp}} * RON_e}{GAIN}\right)^2} \end{aligned}$$

Chapter 4

Spectral Analysis

We can set about analyzing spectra we got from the telescope after processing them. We are mainly interested in red quasars as stated in Sect. 1.3, and we want to know what are the reasons for such quasars to be much redder than other normal blue ones. There are two properties of these quasars which are the most relevant and helpful for our research since in general, the quasars can either be reddened by the dust or their high redshifts or the combination of the two factors as mentioned in Sect. 1.2.1. Therefore, the first thing we can do is to get the intervening dust extinction coefficient on the line of sight from us to the quasars, which can indicate how much dust there is in the intervening space, while the dust can present in the quasars themselves, their host galaxies or the intergalactic materials such as the interstellar medium or intervening galaxies. Second, we can derive the redshifts of these quasars, which is a very basic but key property of astronomical objects. When knowing the redshift, we can determine the chemical properties at the same time and physical characteristics as well. Investigating the redshift can also help with the understanding of the galaxy evolution. We can find out these two factors with spectral analysis, by fitting our spectra with the quasar template, which will be elaborated in Sect. 4.2. Then, more detailed information about the quasars can be analyzed, such as their classification, configurations, or possible outflows.

4.1 Dust Extinction

As we want to know how much dust there is between us and the quasars, we need to know how dust extinction works first. [Trumpler \(1930a\)](#) was the first one to document the absorption of light in the interstellar space due to possible extinction from gas or solid particles of extremely small size, with the evidence shown in Fig. 4.1. We can see

that there are many clusters that have larger photometric distances than the expected angular diameter measured ones, while they should be identical if there is no interstellar extinction. That is to say, the object with the given diameter distance appears much fainter than one would suppose, which indicates the existence of extinction in the galactic systems. Nowadays, we know that extinction is contributed by the absorption and scattering of radiation from targets by interstellar dust and gas.

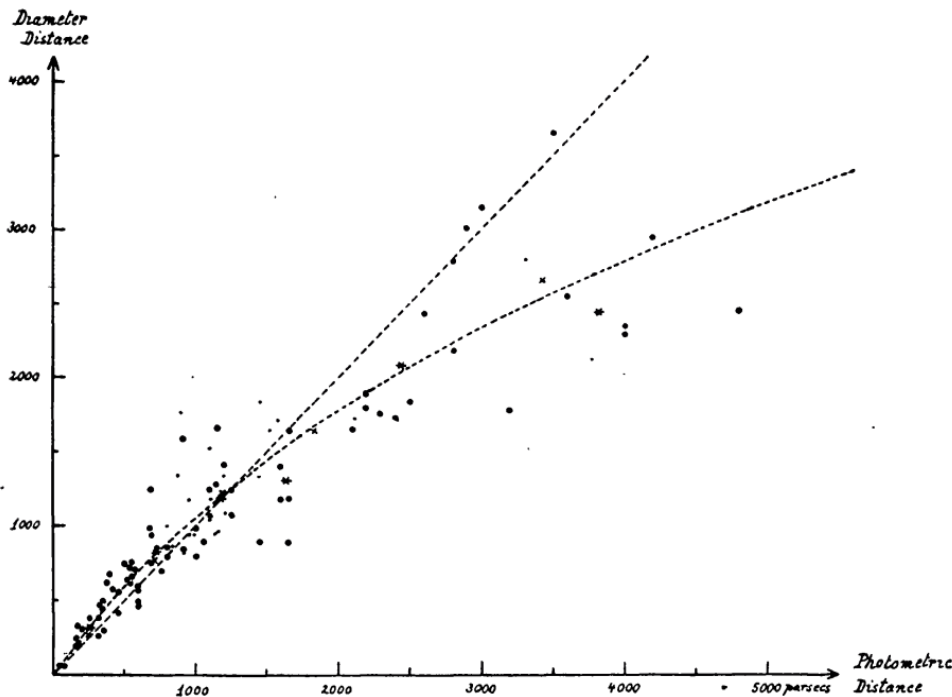


Figure 4.1: The comparison of angular diameter distance and photometric distance of 100 star clusters from [Trumpler \(1930a\)](#). The dotted straight line shows the case that these two kinds of distance are identical and the dotted curve gives the relation between two measurements of distance with assuming a general interstellar extinction of 0.7 magnitudes per 1000 parsecs.

4.1.1 Absorption

Such extinction is due to the appearance of gas clouds and dust in the intervening medium, while gas clouds tend to absorb the radiations with specific wavelengths depending on their composition, due to discrete atomic electron transitions and molecular transitions, which contain rotational transition, vibrational transition, and electronic transitions as well. Atomic and molecular absorption lines are produced in ways that may be broadened due to the mechanical motion of gas clumps or collisions between particles. The gas absorption lines can be used to investigate the chemical evolution in the intergalactic medium or chemical properties of certain clouds. However, the absorption due to intervening gas won't influence the colors of objects so much in general, since it's merely a kind of localized feature in the spectrum. At the same time, the filters for photometry have relatively broad widths.

Thus, we mainly consider the dust extinction here in our thesis as one factor to redden the quasars, since the dust grains can diminish the radiation with shorter wavelengths (UV, optical, and near-infrared (NIR)) and re-emit the absorbed energy at longer wavelengths such as mid-infrared (MIR) or submillimeter, making the radiation redder than that without undergoing dust attenuation. Different from the gas, the cosmic dust can vary in size from several molecules (a few Å to several dozen Å) to microns, which may consist of carbon, silicates, silica, metal oxides, pure metals, or more species (Molster et al. 2010; Cherchneff 2010; Sarangi et al. 2018). The relatively large sizes of solid dust grains can keep radiation with wavelengths shorter than the dimension of dust grains from diffracting through them without extinction. Thus, radiation with a shorter wavelength tends to be absorbed by dust grains, while radiation with a longer wavelength can pass through dust much more easily, based on the absorption coefficient function eq. (4.1),

$$\kappa_\nu = \frac{N\pi a^2 Q_\nu}{N\frac{4}{3}\pi a^3 \rho_G} = \frac{3Q_\nu}{4a\rho_G} \quad (4.1)$$

where κ_ν refers to the absorption coefficient per unit grain mass, a refers to the radius of grains, N is the number of grains, and Q_ν denotes the emissivity of grains, which equals to the absorption efficiency Q_{abs} , according to Kirchoff's law of thermal radiation by assuming the grains are in full equilibrium (for more details see Emerson 1999). Although for the constant emissivity, grains seem to absorb more efficiently if they are small, in fact, the emissivity is not constant and will decrease significantly once the grains become smaller than the wavelength of radiation. Therefore, the grains with the size of the order of radiation wavelength can absorb the corresponding light the most efficiently, plus in reality, substantial numbers of dust grains with sizes comparable to the wavelengths of UV and visible light are present in the interstellar medium. In a more quantitative way, Mathis et al. (1977) found that the classical size distribution of the dust grains is $dn \propto a^{-3.5} da$, showing that there are much more dust grains with small sizes than those which are larger. As a result, dust becomes very efficient at extinguishing radiation with shorter wavelengths such as UV and blue light (Trumpler 1930b). This is also one of the reasons why gas particles (atoms and molecules) are not considered the main factor in reddening the radiation because, after all, their sizes are so much smaller than those of dust grains, which makes them not good absorbers at UV and visible wavelength.

4.1.2 Scattering

Besides absorption, however, extinction also contains the effect of radiation scattering by dust and gas, where the gas can play a role. For small particles like gas and small dust grains (with the upper limit of size being about 1/10 the wavelength), Rayleigh scattering is considered as the mechanism for radiation scattering here. The Rayleigh scattering cross-section σ_s is given by eq. (4.2),

$$\sigma_s = \frac{2\pi^5 d^6}{3 \lambda^4} \left(\frac{n^2 - 1}{n^2 + 2} \right)^2 \sim \frac{1}{\lambda^4} \quad (4.2)$$

in which d is the diameter of the particle, λ is the wavelength of the incident light, and n refers to the refractive index (Siegel & Howell 1981). The Rayleigh scattering cross-section has strong wavelength dependence, which can be approximated to be reciprocal of λ^4 , making blue radiation with shorter wavelengths scattered more significantly than red light with longer wavelengths. Because the blue light is scattered more strongly, less blue light from the targets can follow the line of sight and be received by us on the Earth. However, the density of gas in the interstellar medium is not as high as that in the atmosphere, so the scattering of gas may not be that significant. Therefore, the scattering is still dominated by the dust grains, especially the small ones.

4.1.3 Extinction

The combination of absorption and scattering becomes the effect called extinction, causing interstellar reddening. The extinction can be expressed as eq. (4.3),

$$\kappa_{\text{ext}}\rho = \kappa_{\text{abs}}\rho + \kappa_{\text{sca}}\rho = N\sigma Q_{\text{ext}} = N\sigma (Q_{\text{sca}}(\lambda) + Q_{\text{abs}}(\lambda)) \quad (4.3)$$

where κ is the coefficient per unit grain mass and Q is the efficiency, with subscripts (ext, abs, and sca) referring to extinction, absorption (for more details see Emerson 1999). σ is the geometrical cross-section. In a word, the overall effect of scattering and absorption, which is the extinction, prefers to eliminate photons with shorter wavelengths while photons with longer wavelengths will survive, keeping the emission and absorption features unchanged. Thus, in the visible band, the light turns out to be redder. A classic example of the interstellar reddening is shown in Fig. 4.2, and the optical radiation from stars behind the dark cloud B68 is completely obscured by a large amount of dust in the cloud as we can see in Fig. 4.2a. B68 is not a void region, and it's just

optically opaque, since the stars there are only visible at the longer wavelengths (such as infrared), making them appear red in Fig. 4.2b.

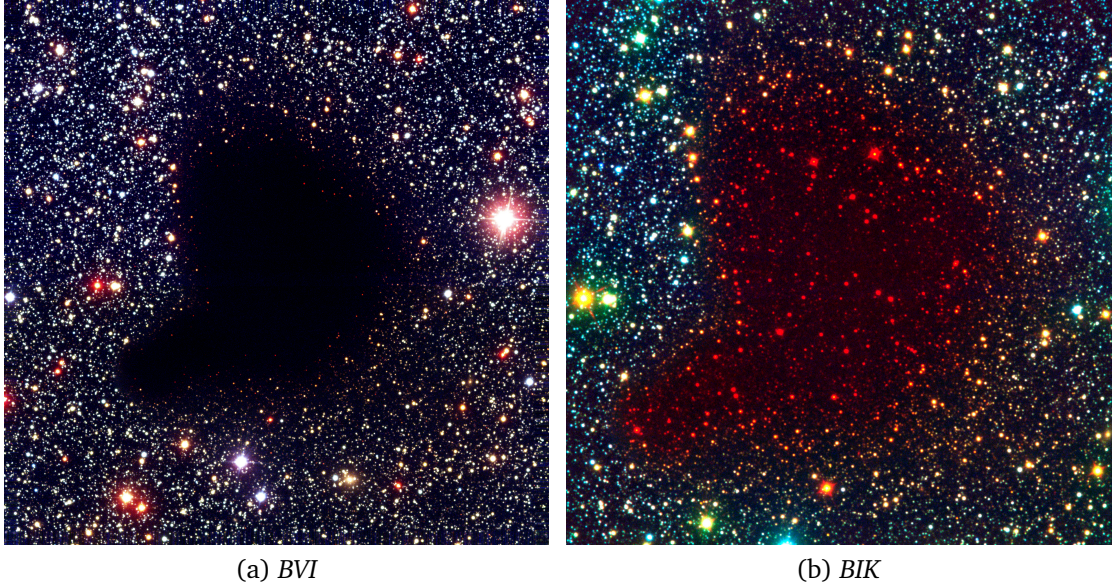


Figure 4.2: The three-color composite images of the central area of globule Barnard 68 (B68) dust cloud, with panel (a) showing the color composite of the visible and near-infrared band (B_440 nm, V_557 nm, and I_768 nm). The panel (b) is the false-color composite figure that combined a visible image (B_440 nm, rendered as blue), a near-infrared image (I_768 nm, green) and an infrared (K_2160 nm, red) image. **Credit:** ESO.

In practice, however, it's not so realistic to obtain the extinction coefficient per unit grain mass κ_{ext} directly from the observation results, not to mention that we may need the intervening dust mass in advance to carry out the measurement of the dust extinction by following the procedures based on eq. (4.3). A more common and intuitive way is to determine the total extinction directly, which we can easily get from the observation, based on the observed color index of one object and its intrinsic color index, which usually can be replaced by the normal color index of the same kind of object. To be specific, the amount of interstellar reddening can be denoted by the color excess, which is defined as the difference between the observed color index and the hypothetical true color index without extinction of the same target, shown in eq. (4.4),

$$E_{B-V} = A_B - A_V = (B - V)_{\text{observed}} - (B - V)_{\text{intrinsic}} \quad (4.4)$$

in which E_{B-V} denotes the color excess of the B band to the V band. A_B and A_V refer to the total extinctions at the B and V photometric bands, while $(B - V)_{\text{observed}}$ and $(B - V)_{\text{intrinsic}}$ are the observed and intrinsic $B - V$ color indices, such that,

$$B_{\text{observed}} = B_{\text{intrinsic}} + A_B, \quad V_{\text{observed}} = V_{\text{intrinsic}} + A_V \quad (4.5)$$

where B and V are the observed and intrinsic (normal) values for the magnitudes of objects at the corresponding bands.

In general, every different kind of object can have a different color index in a certain band. The reason is that the objects in different temperatures will have dissimilar spectra, according to the black body radiation theory and Wien's displacement law ($\lambda_{\text{peak}} = b/T$, with b known as Wien's displacement constant, equal to $2.898 \times 10^{-3} \text{ m K}$), which shows that the radiation from a black body can peak at different wavelengths if it has different temperatures. We basically classify the objects based on their unique spectra which are distinct from others. The significant dissimilarity in objects' spectra will be reflected in their colors, which are often used for the selection of a certain kind of object when we don't have enough time to get spectra of every single target, especially in modern large sky surveys.

Take stars as an example, the hotter the stars, the bluer they will appear. Main sequence O5 stars can have a BV index of about -0.33, while main sequence M0 stars have a BV index of around 1.4 (Zombeck 2007). In this manner, we often use the intrinsic color index as the hypothetical color index of the target unaffected by extinction, as long as we confirm what kind of object it is. Besides, the hotter (or bluer) the stars, the lower value the color index has, as we can see in the example above and O type stars are the hottest stars. This is a very natural conclusion since according to what is demonstrated in Sect. 1.1.3 and eq. (1.5), brighter objects have smaller magnitudes, and if the objects are brighter at the B (Blue) band, they appear bluer. In addition, the magnitude of the band with the shorter wavelength is always the minuend in the color index. Therefore, when the color index is negative, the objects are considered to be blue.

This is also the reason why we can use the color selection techniques elaborated in Sect. 1.2 to distinguish quasars from stars because quasars are much hotter than stars. Nonetheless, the empirical consequence of the normal intrinsic color index of a certain type of object can inevitably be wrong on some occasions, such as the red quasars we research in this thesis, which are reddened by the dust and have unusual color indices. Although the empirical conclusions are not accurate all the time, we have to rely on them and after all, they are usually correct. Summarizing the common rules out of similar phenomena is also an essential way to get empirical evidence and conduct scientific research, while the divergence between abnormal phenomena and empirical evidence is also a miraculous booster for scientific development. Here, in research on extinction in astronomy, the empirical evidence is widely accepted and used, which is known as standard extinction curves.

4.1.4 Standard extinction curves

Knowing the color excess of certain filter bands is not enough for our measure of extinction, because our ultimate goal is to reproduce the observed diminished spectra with the empirical extinction law and the normal spectra that one kind of object would have. These normal spectra are usually referring to templates like the quasar template introduced in Sect. 4.2. The extinction law should describe how radiation is attenuated depending on the wavelength in a large range, and the summarized rule is called the standard extinction curve, which is also the main approach to research the dust properties.

Before we demonstrate the standard extinction curve, we can first discuss how the extinction curve for one single object is derived. In principle, it's made by comparing the observed spectrum of the target, such as a star, with the spectrum of another star, which is the same type as our target but appropriately chosen to be unaffected by the extinction. The method is called the standard-pair method, using the reddened and comparison star pairs to study the extinction curve (it's a bit tricky but important to identify a good comparison star, for more details see [Fitzpatrick 1985](#) and [Gordon & Clayton 1998](#)). The normalized extinction curve for every single target is calculated using the relationship described in eq. (4.6) from [Massa et al. \(1983\)](#),

$$\frac{E(\lambda - V)}{E(B - V)} = \frac{m(\lambda - V) - m(\lambda - V)_0}{(B - V) - (B - V)_0} \quad (4.6)$$

where, unsubscripted quantities denote the observed target, while the items with subscript refer to the chosen unreddened comparison object of the same type as the target (with similar spectral features), which is equivalent to what we called intrinsic color index in eq. (4.4).

Hereafter, the average extinction curve of multiple objects can be derived ([Savage & Mathis 1979](#); [Seaton \(1979\)](#)), while large variations are present between regions ([Pei 1992](#), [Gordon et al. \(2003\)](#)), not only in the Milky Way (MW; [Witt et al. 1984](#)), but also in the Small Magellanic Cloud (SMC; [Prevot et al. 1984](#)) and in the Large Magellanic Cloud (LMC; [Misselt et al. 1999](#)), as shown in Fig 4.3 The variations were not well understood until [Cardelli et al. \(1989\)](#) found that such variations can be demonstrated with merely one parameter, $R_V = A_V/E(B - V)$, which is a rough indicator of the mean dust grain size, and the larger the R_V value, the larger the grain size is. Larger R_V values are also found in dense clouds, which is claimed to be due to coagulation in the dense regions by [Cardelli et al. \(1989\)](#).

[Cardelli et al. \(1989\)](#) also made a big modification to the scale of the extinction curve, which was based on the two-color normalization in the manner of $E(\lambda - V)/E(B - V)$ before as shown in eq. (4.6). They converted the extinction curves to an absolute scale, by normalizing the wavelength-dependent extinction A_λ to the one-color A_V . They affirmed that the quantity A_λ/A_V , which is called absolute extinction, is more fundamental since it's not described by comparing two other colors with the extinction at the wavelength we are concerned about, but expressed directly in the ratio of it to the total extinction at the single visual (V) band. The quantity A_λ/A_V is called absolute extinction because it's an absolute measure of dust properties, unlike the relative measure of those by $E(\lambda - V)/E(B - V)$. Expressing the extinction curves in the absolute scale A_λ/A_V can help to unveil the hidden dust effects more efficiently and accurately.

We need the normalization because we can compare different extinction curves easily after normalizing the observed extinction, by expressing the total extinction at any wavelength A_λ , with respect to the total extinction at a reference wavelength. The V band was chosen as the reference wavelength for the historical reason that all the samples they used had observations at V and B, while observations in other filters were missed in some objects, although the optimal reference wavelength can be the one where the variability is as small as possible.

In addition, [Cardelli et al. \(1989\)](#) found a very clear linear relationship between A_λ/A_V and R_V^{-1} in the absolute scale, and the fact that the average extinction law can be expressed by just one parameter demonstrates that the dust grains must grow in a general and stochastic way, to ensure that grains of all sizes except the largest ones can participate in the extinction process to an appreciable extent, giving a physical interpretation to the variations in extinction curves in different regions.

However, the R_V dependent extinction law is not always the same in the universe, according to [Gordon et al. \(2003\)](#). [Cardelli et al. \(1989\)](#) did the research only based on the samples in the Milky Way, while [Gordon et al. \(2003\)](#) found that all of the extinction curves derived from reddened stars in the SMC star-forming bars don't follow the relationship described by [Cardelli et al. \(1989\)](#). Besides, only 4 out of 19 extinction curves obtained in the LMC coincide well with those in the Milky Way. So there must be some difference in the physical and chemical conditions of the SMC, the LMC, and the Milky Way, while the extinction curves from these three regions are still related.

[Gordon et al. \(2003\)](#) showed strong evidence that the A_λ/A_V to R_V^{-1} relationship in [Cardelli et al. \(1989\)](#) acts as a bound of that derived from all the extinction curves of Magellanic Clouds, which shows that the extinction is still related to the dust grain size

in the Magellanic Clouds and even the whole universe, but the size distribution there may be different. In addition, some other factors may also play a role in producing the extinction curves, such as the gas to dust ratio ($N(H_I)/A_V$) or related metallicity proposed by [Gordon et al. \(2003\)](#), or chemical composition of grains mentioned by [Pei \(1992\)](#).

By combining the extinction curves from the Milky Way, the SMC, and the LMC observed from ultraviolet to near-infrared, [Gordon et al. \(2003\)](#) presented the sample average extinction curves shown in Fig. 4.3, where we can clearly notice the difference between the extinction curve of the SMC and those of the LMC and the Milky Way. The SMC extinction curve is the most distinct one, as there isn't a bump at the wavelength around 2175 \AA in it, while the extinction curves of the LMC and the Milky Way all have such features, although the strength may differ. Besides, there is also stronger far-UV extinction in the SMC, which may indicate that the average sizes of dust grains there may be smaller than those in the other two galaxies.

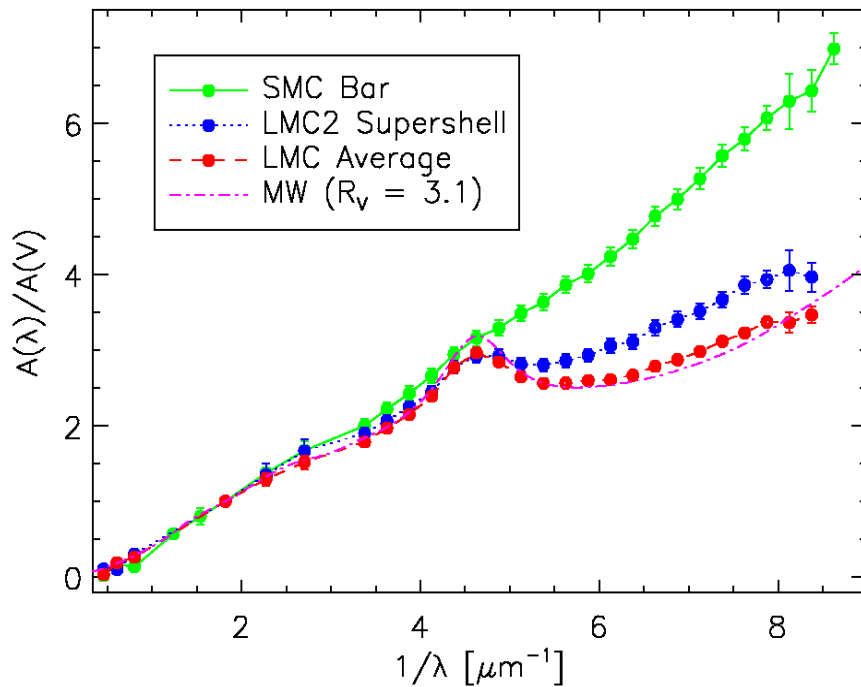


Figure 4.3: The combined average extinction curves of the Milky Way, the SMC bar, and the LMC ([Gordon et al. 2003](#)). **Credit:** Karl D. Gordon on wikipedia.org.

The SMC, the LMC, and the Milky Way are still the three main sources of the extinction curves we adopt in the research influenced by the extinction. Due to their overall similarities and the general R_V dependent relationship, it's feasible to extrapolate such extinction curves to other reddened objects in other galaxies as long as their ambient environments are similar to the galaxy where one gets the extinction curve. Different from the Milky Way, the extinction curves obtained from the Magellanic Clouds origi-

nate from the active star-forming regions, plus the Magellanic Clouds also have lower metallicity and dust abundance than Milky Way. As a consequence, the extinction curves of the Magellanic Clouds (especially the ones from the SMC) can be more applicable to the high-redshift galaxies (Pei 1992), which are considered to have fewer metallicities and higher star formation rates (Somerville et al. 2001; Mannucci et al. 2010).

4.1.5 SMC-like quasar extinction curve

As quasars are usually located at the center of high-redshift galaxies, it's reasonable that the SMC extinction curves can apply to simulating the extinction that the reddened quasars undergo. This is a strategy that is commonly used in the study of the quasar extinction, while the composite quasar extinction curve constructed by Czerny et al. (2004) based on the work of Richards et al. (2003), following the same way to obtain those extinction curves in the three galaxies introduced in Sect. 4.1.4, was questioned by Willott (2005). Willott (2005) argued that the idea to make sample average extinction curves like what people did for the SMC, the LMC, and the Milky Way extinction curves is not valid anymore in the case of quasars, since the quasars used to create the composite quasar extinction curve have different redshifts. Taking such action can make Czerny et al. (2004) risk combining quasars at different redshifts, which may have different physical conditions, resulting in artificial quasar extinction law.

The SMC-like quasar extinction curve is then thought to be proper for demonstrating the actual quasar extinction, investigated by Crenshaw et al. (2001; 2002), Richards et al. (2003), and Hopkins et al. (2004). It's then widely used to match the effect of dust in the research of the reddened quasars (Fynbo et al. 2013; Krogager et al. 2019; Fynbo et al. 2020) and becomes a kind of empirical routine now to apply the SMC-like extinction curve to present the dust extinction of quasars unless there is a bad fit around 2175 Å, where the LMC-like or MW-like extinction curves with a bump may be more suitable.

Therefore, We use the SMC-like extinction curve to infer the amount of extinction as well. Moreover, because we need to fit the observed spectra, the numerical extinction laws presented in many papers are not enough, and we utilize the analytical fitting function for the SMC-like extinction curve given by Pei (1992), covering all wavelengths, as shown in eq. (4.7),

$$\xi(\lambda) = \sum_{i=1}^6 \frac{a_i}{(\lambda/\lambda_i)^{n_i} + (\lambda_i/\lambda)^{n_i} + b_i} \quad (4.7)$$

in which $\xi(\lambda) = A_\lambda/A_B$ is a nondimensional quantity similar to the absolute extinction mentioned in Sect. 4.1.4, while A_B is the total extinction at the B band, different from the commonly used normalization factor A_V in the initial absolute extinction expression (A_λ/A_V), which is first introduced by Cardelli et al. (1989). However, it won't influence much because A_B and A_V are closely related by the value of R_V , since $R_V = A_V/E_{B-V} = A_V/(A_B - A_V)$, and A_B can be express by A_V as described in eq. (4.8),

$$A_B = \left(\frac{R_V + 1}{R_V}\right)A_V \quad (4.8)$$

while the value of R_V varies in different parts of different galaxies, depending on the dust properties there. The standard R_V value of the diffuse interstellar medium in the Milky Way is $R_V = 3.1$, plus R_V is usually equal to 5 for dense clouds (Cardelli et al. 1989). For the SMC and LMC, the value of R_V is typically between 2 and 3. In general, A_B is thought to be approximately $\frac{4}{3}A_V$, however, it's only valid for the diffuse clouds in Milky Way.

The other parameters a_i, λ_i, n_i, b_i in eq. (4.7) are free parameters, and they all should be positive. The summarized estimates of these parameters after fitting the analytical extinction curve to the three classic extinction curves in the SMC, LMC and MW (Fig. 4.3) are shared by Pei (1992), presented in Fig. 4.4.

For reddened quasars, by substituting the corresponding parameters of the Small Magellanic Cloud into eq. (4.7), we can obtain the SMC-like absolute extinction $\xi(\lambda)$ at all wavelengths of our observed spectra, and by assuming a value of the free parameter A_B , we can derive the actual total extinction at every wavelength with eq. (4.9), which is the analytical SMC-like extinction law applicable to demonstrate the effect of dust in the quasar reddening process.

$$A_\lambda = \xi(\lambda)A_B \quad (4.9)$$

We can acquire the reddened quasar spectra which match the observed spectra by applying the analytical SMC-like extinction law to the quasar template with a fitted appropriate value of the free parameter A_B , in the manner demonstrated by eq. (4.10),

$$I = 10^{-0.4 \times A_\lambda} \times I_0 \quad (4.10)$$

ANALYTIC EXTINCTION CURVE PARAMETERS					
Parameter	a_i	$\lambda_i (\mu\text{m})$	b_i	n_i	K_i
Milky Way Galaxy					
BKG	165.	0.047	90.	2.0	2.89
FUV	14.	0.08	4.00	6.5	0.31
2175 Å	0.045	0.22	-1.95	2.0	0.16
9.7 μm	0.002	9.7	-1.95	2.0	0.31
18 μm	0.002	18.	-1.80	2.0	0.28
FIR	0.012	25.	0.00	2.0	0.76
Large Magellanic Cloud					
BKG	175.	0.046	90.	2.0	3.00
FUV	19.	0.08	5.50	4.5	0.56
2175 Å	0.023	0.22	-1.95	2.0	0.08
9.7 μm	0.005	9.7	-1.95	2.0	0.77
18 μm	0.006	18.	-1.80	2.0	0.86
FIR	0.020	25.	0.00	2.0	1.26
Small Magellanic Cloud					
BKG	185.	0.042	90.	2.0	2.89
FUV	27.	0.08	5.50	4.0	0.91
2175 Å	0.005	0.22	-1.95	2.0	0.02
9.7 μm	0.010	9.7	-1.95	2.0	1.55
18 μm	0.012	18.	-1.80	2.0	1.72
FIR	0.030	25.	0.00	2.0	1.89

Figure 4.4: The concluded fitted parameters in eq. (4.7) to produce the analytical extinction curves for the MW, LMC, and SMC respectively (Pei 1992).

derived from eq. (1.5) and eq. (4.5). In eq. (4.10), I_0 denotes the intrinsic flux from the target without extinction, while I refers to the flux after reddening. According to eq. (4.5), we can also know that $m - m_0 = A_\lambda$, in which the magnitude with subscription is the magnitude of the object without extinction. After substituting the relationship between A_λ and the magnitudes into eq. (1.5), we can attain eq. (4.10) which is essential in the practical process when applying the SMC-like extinction law to the normal quasar template.

4.2 Quasar Template

There are two free parameters we need to consider when we fit the observed quasar spectra with the quasar template, which are the total extinction at the B band A_B required in eq. (4.9) to match the overall continuum with the spectra and the redshift to match the spectra features (emission and absorption) in the observed spectra. However, before all the fitting work, a template spectrum of normal quasars is the most

fundamental and necessary thing we need to prepare.

The first popular and widely used quasar template was produced by [Vanden Berk et al. \(2001\)](#), median combining over 2200 quasar spectra from the Sloan Digital Sky Survey (SDSS; [Blanton et al. 2017](#)), whose redshifts range from 0.044 to 4.789 and r magnitudes range from -18 to -26.5. The samples were selected in the manner described by [Richards et al. \(2002\)](#) from their non-stellar colors and possible radio properties. The template of [Vanden Berk et al. \(2001\)](#) improved a lot compared to the old ones such as the First Bright Quasar Survey (FBQS) composite from [Brotherton et al. \(2001\)](#), which were generated using the entirely radio selected quasars. However, there are still problems with the Vanden Berk's template (VB template), as shown in Fig. 4.5, created by [Fynbo et al. \(2013\)](#).

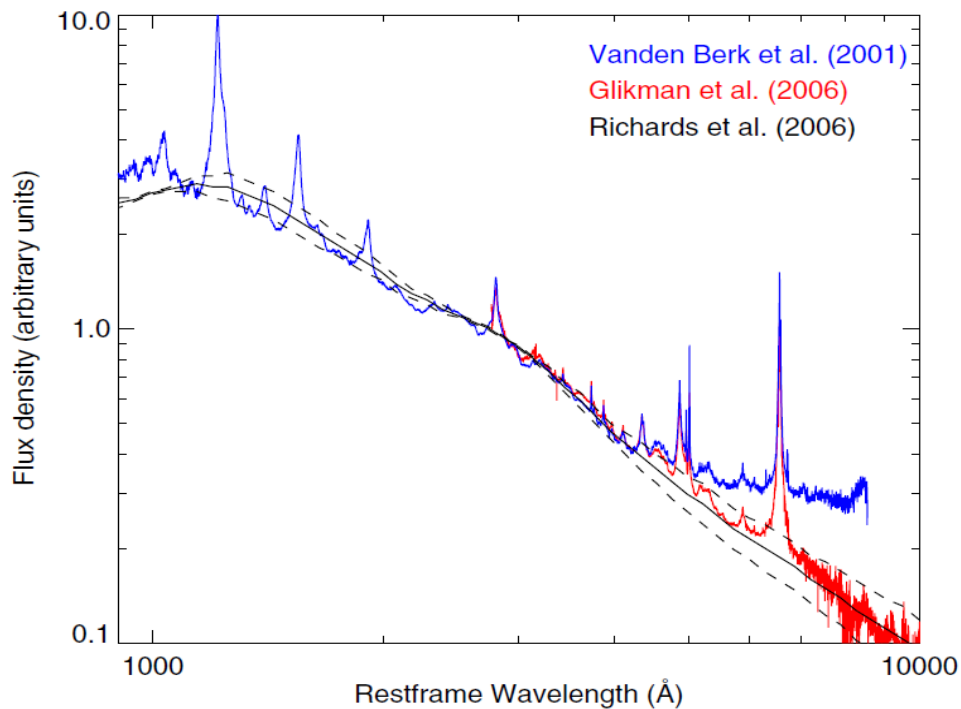


Figure 4.5: The comparison of quasar templates from [Vanden Berk et al. \(2001\)](#), [Glikman et al. \(2006\)](#), and [Richards et al. \(2006\)](#), with dashed lines showing the $\pm 1\sigma$ curves relative to Richards's template ([Fynbo et al. 2013](#)).

We can clearly see the discrepancy between the VB template and others at the wavelengths longer than 5000 \AA , which is presumably because of the excess emission from the host galaxy contamination in the VB template ([Fynbo et al. 2013](#)), noticed by [Vanden Berk et al. \(2001\)](#) themselves as well. Thus, to solve the problem, [Fynbo et al. \(2013\)](#) merged the VB template at shorter wavelengths (shorter than 3000 \AA at the rest frame) with the template made by [Glikman et al. \(2006\)](#) at longer wavelengths (longer than 3000 \AA at the rest frame). However, this tentative solution didn't work well and a new problem was found that they couldn't fit the specific example of CQ0127+0114

well simultaneous at the optical and near-infrared regions, which was indicated in Fig. 4.6.

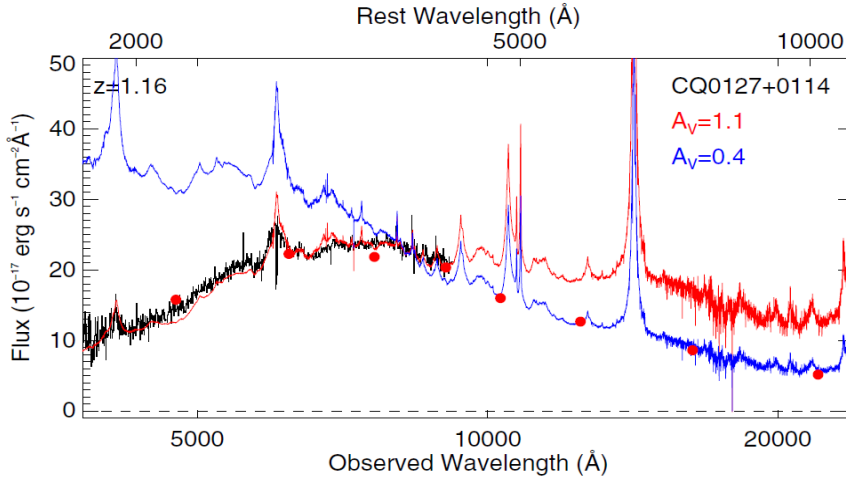


Figure 4.6: Attempts to fit the spectrum of CQ0127+0114, which can be only achieved by fitting the optical and near-infrared parts separately (Fynbo et al. 2013).

Fynbo et al. (2013) proposed a possible extinction curve with a steeper UV rise than that of the SMC can solve such contradiction in the measure of dust extinction, to match the full spectrum, which was seen in Crenshaw et al. (2001) and even in the afterglow of gamma-ray bursts (Fynbo et al. 2014; Heintz et al. 2017). Nevertheless, it's still a bit arbitrary to stitch the different templates together, as argued by Selsing et al. (2016), which can introduce different systematic effects due to distinct quasar samples selected in different template spectra and different instruments used to make the observations.

Therefore, it's necessary to generate a template spectrum of quasars from quasar samples without significant host galaxy contamination observed with one single facility, but it should cover a relatively large range of wavelengths. This arduous work was done by Selsing et al. (2016), and the produced quasar template spectrum is what we use in this thesis.

Selsing et al. (2016) chose bright blue quasars with redshifts between 1 and 2 from the SDSS and observed them with X-shooter simultaneously, which enabled the spectra to cover the UV to near-Infrared light (3100 - 24800 Å). The selected luminous ($r \lesssim 17$) blue quasars at redshifts $1 < z < 2.1$ can ensure the insignificant host galaxy contamination and negligible dust extinction, helping to create an uncontaminated normal quasar template, displayed in Fig. 4.7.

The data and code to reproduce the template spectrum of normal quasars are available at <https://github.com/jselsing/QuasarComposite>. The comparison of this template with other composites is also presented in their paper, showing a high degree of similarity and better performance at the redder wavelengths as expected.

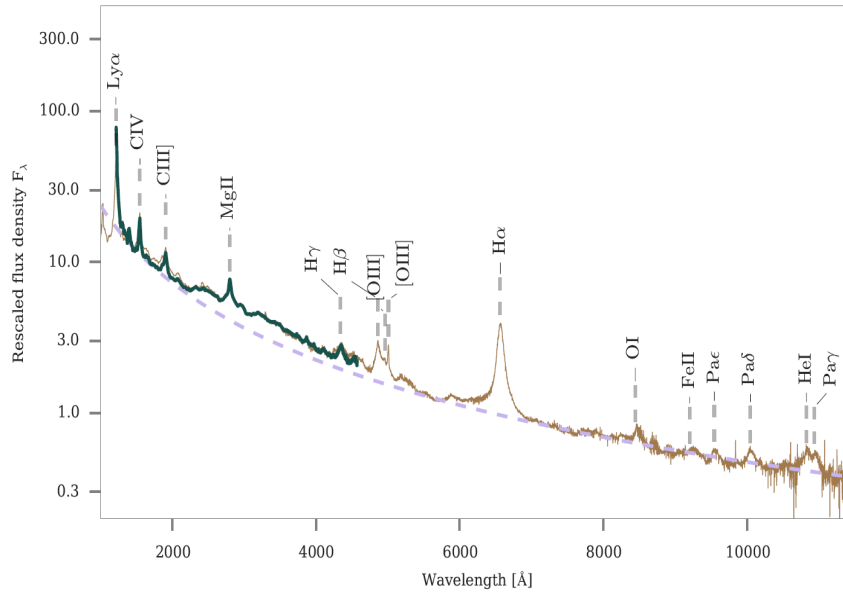


Figure 4.7: The X-shooter weighted arithmetic mean quasar composite is plotted in brown by [Selsing et al. \(2016\)](#). The overplotted dark green line is the combined SDSS spectra of the same samples as those used to generate the X-shooter composite, and they are in good agreement, with a purple line demonstrating the continuum.

Nevertheless, the VB template is not entirely wrong and it may be more applicable to the quasars with lower redshift since they are intrinsically fainter than high redshift ones. Quasars at lower redshifts, are more likely to be embedded with their host galaxies due to the galaxy evolution, making them contaminated by their host galaxies inherently because the galaxies at lower redshift tend to be much denser and have larger stellar mass ([Muzzin et al. 2013](#)). Therefore, it's not very proper to fit these quasars at low redshifts with the template from [Selsing et al. \(2016\)](#) anymore, for they assume that quasars are not influenced by the host galaxies, while it's not true for nearby quasars.

Therefore, in general, we decide to fit the spectra of quasars at low redshifts (here $z < 1$ in our thesis) with the template from [Vanden Berk et al. \(2001\)](#), and fit the high-redshift ones with the template generated by [Selsing et al. \(2016\)](#).

4.3 Fitting Procedures

We have the required quasar template spectrum and applicable SMC-like extinction curve in hand, and we can set about fitting all the processed spectra of our observed quasar candidates. We can work on it in the following ways.

First, Check if there are any significant emission features in the spectra. Normally there will be a few since the broad emission lines are one of the unique characteristics of quasars. Then we need to classify the emission lines and find out which elements they

are produced by. Because we merely observed in the optical and near-infrared bands, we just need to consider the emission lines in the bluer part of the template spectrum shown in Fig. 4.7. There are some special emission lines we can easily identify. Especially the triple-horn shape emission lines of the $H\beta$ line embedded with two forbidden lines $[O\ III]\lambda 4960$ and $[O\ III]\lambda 5008$ nearby are the most distinct ones. Once we recognize such unique lines, we can immediately derive the redshift of the corresponding object with the help of eq. (1.2). Besides, the extreme emission lines like the $Ly\alpha$ line and the $H\alpha$ line are effortless to be found as well. In addition, the relative positions of emission lines can also help. For instance, the closely located lines $Ly\alpha$ line, $C\ IV$ line, and semi-forbidden $C\ III]\lambda 1908$ line are usually conspicuous in the spectrum, and the $Mg\ II$ appears individually, without any obvious emission features close by, similar to the $H\alpha$ line, but has a lower intensity in general. All the rest wavelengths of the significant emission lines appearing in the spectra of quasars can be found at <http://classic.sdss.org/dr6/algorithms/linestable.html>, which is used in the SDSS.

However, the absence of emission lines can sometimes happen, which will make the determination of redshifts much more difficult. Such features are usually seen in detached BAL quasars, while the reason is still not well understood. We have found a quantitative way to derive the redshifts of detached BAL quasars without any emission lines more accurately and credibly, which is elaborated in Sect. 5.3.

After finding out the redshifts, we can start to measure the dust extinction. The optimal result is obtained when we fit the full continuum of a spectrum well with the template shifted to a certain redshift. The only parameter we need to fit as what has been mentioned in Sect. 4.1.5, is the total extinction at the B band (A_B). However, there are cases that we can't fit the entire continuum, as showed in Sect. 5.2 plus discussed in Sect. 4.2 and Fynbo et al. (2013). We are inclined to fit the redder wavelengths since a steeper UV extinction in the quasar's SMC-like extinction curve is expected in order to match the whole continuum (Fynbo et al. 2013). The redder parts are usually given by photometric data, as we can't observe these infrared wavelengths with our optical telescope. With the help of photometric data from the SDSS (Blanton et al. 2017), 2MASS (Skrutskie et al. 2006), UKIDSS (Lawrence et al. 2007), and ALLWISE (Wright et al. 2010; Cutri et al. 2013), we can make sure that we fit the observed spectra well.

All the best-fit spectra are displayed in Sect. 5.2, with which we can classify the quasars and study some specific types.

Chapter 5

Results and Discussion

Now we have the processed spectra, needed SMC-like dust extinction curve, and quasar template ready. By following the fitting procedures described in Sect. 4.3, we can get the measured redshift, the estimated amount of dust extinction at the B band (A_B), and the best-fit spectra.

In conclusion, we find 23 normal quasars, 18 BAL quasars, 2 detached BAL quasars, 2 peculiar quasars, and 5 stars among our samples. The full list including classifications and corresponding parameters is presented in Table 5.1 and all of their spectra in Sect. 5.2. Moreover, the explanation of how we measure all the parameters and do the classifications for every target with full details is given in the Notes on Individual Objects in Sect. 5.2.

Besides presenting our results, we discuss the reason for the distributions of our selected targets with mostly red and peculiar colors on the color-color map, in Sect. 5.1, showing the role of redshifts and different amounts of dust extinction in changing the color of all the objects. In addition, a circumstantial investigation of the detached BAL quasars, which is extremely interesting for their unique spectra, is implemented in Sect. 5.3. After all the discussions, we hope it's crystal clear that the complete census of quasars without relying on color criteria is essential and demanded by future research with a need for precise statistical analysis, which can only be achieved with the help of big enough datasets.

5.1 Classifications and Properties of Observed Targets

We display the overall visualization of the best-fit parameters in Fig. 5.2, placing the targets in the color-color diagram in the same way as Fig. 1.8 to give a comparison, and

plot a background consisting of the normal quasar and star clumps from Fig. 1.7 in black on the same maps for more intuitive perception. Although not all the observed targets are shown in the plot due to the lack of photometry for some of them, in this manner, we can tell why our selected targets have unusual colors and are located separately from the normal population accordingly, with the help of their spectra shown in Sect. 5.2.

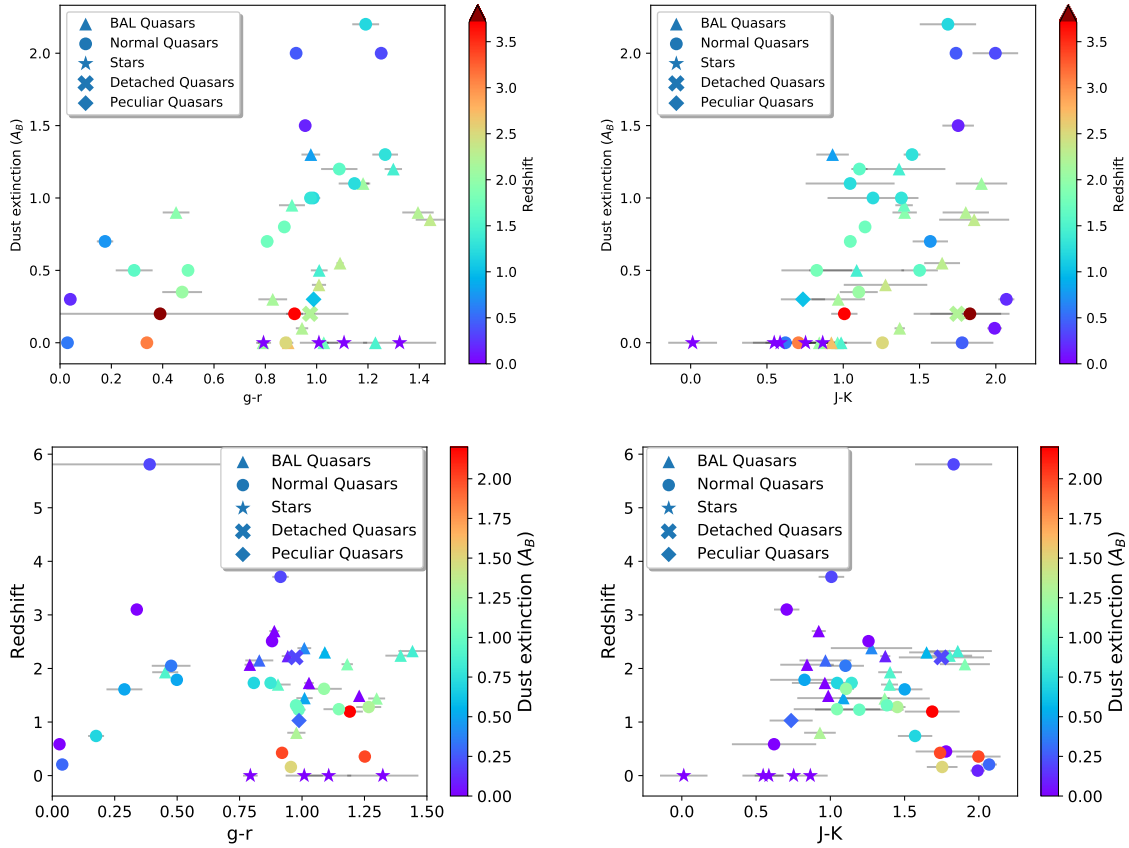


Figure 5.1: Illustrations of the dust extinction and redshift properties of objects with different color excesses in the optical and infrared band ($g - r$, $J - K$). The objects with a higher value on the x-axis are redder as described in Sect. 1.2.3, showing the red colors of objects as a joint result of their redshift and amount of interstellar dust extinction, while dust may play a more significant role in the reddening, especially that in the infrared, as indicated by the upper panels.

Generally speaking, the combined effects from the high redshifts and a large amount of dust extinction give our samples their uncommon colors. As we can see in Fig. 5.2, our main research targets, red quasar candidates in the center of the figures, have either high redshifts up to $z = 3.71$, rather large amounts of dust reddening with a maximum of $A_B = 2.2$, or both but have slightly medium values for these two parameters, with the mean combination of $z = 1.5$ and $A_B = 0.75$. When one is greater, the other parameter is likely to have a lower value, as demonstrated by Fig. 5.1. Besides, the objects redder in the optical bands (with higher $g - r$ value) or infrared bands (with higher $J - K$ value) appear to be more possible to have a higher dust extinction level, as shown in the upper panels of Fig. 5.1, which exemplifies the fact that the dust absorbs radiation in the blue while re-emits the energy in the red, most of which in the infrared, agreeing

with the top right plot in Fig. 5.1. The redshift seems to spread randomly, for it only makes the emission line be shifted randomly into the passband of some photometry filters, as illustrated by the bottom panels of Fig. 5.1.

More importantly, almost all our selected red quasar candidates in the lands between the star and quasar clusters are indeed quasars (29 out of 30, with one bordering the stellar locus), which directly demonstrates that we can miss a large number of quasars based on the high-efficiency pure wise color criterion. It can be improved when you make the more and more sophisticated color criteria, but no matter what, these criteria can't get rid of the inevitable selection bias due to their limited samples and the intrinsically low accuracy of photometry.

Furthermore, nearly all the special quasars (BAL quasars, detached BAL quasars, and peculiar quasars) are located in the red region. These targets are already worthy of being investigated simply due to their distinction from normal counterparts, not to mention the possibility for them to have a different nature or experience different evolution stages, which is very essential for our research on the galaxy evolution plus the growth of black holes. In addition, we propose that the detached BAL quasars found in our observations can help to substantiate one model illustrating the inner structure of disk wind in quasars, as described in Sect. 5.3.2.

However, if we persist in the color criteria, we may overlook these special quasars, preventing us from having a true and complete perception of the quasars and even the universe. For example, our result of finding 16 BAL quasars in the red quasar candidates (with the colors of 3 BAL quasars are not found) indicates that we can overlook a large amount of BAL quasars in the universe, which may generally be much redder than normal quasars for their either potential dusty feature or they just seem to endure more dust absorption due to certain range of viewing angles. Our present estimation of their population to be 10% can in fact be too low, which is consistent with the argument proposed by Allen et al. (2011) that the intrinsic C IV BAL quasar fraction in the entire quasar population can be much higher and even reach 40%.

As for other quasar candidates located on the outskirts of the normal star and quasar groups, dissociated from the red quasar candidates, they also follow the general rule that is shown in Fig. 5.1. When they suffer more dust extinction, they tend to have higher $J - K$ values (redder in the infrared), except for two outliers at the bottom right corner in Fig. 5.2. However, we don't think they break the rule.

CQ 001035.57-070232.2 and CQ 003236.58-091026.2 are the two outliers. The first object CQ 001035.57-070232.2 has the color excess of $g - r = 0.04$, $J - K = 2.069$,

and CQ 003236.58-091026.2 has $g - r = -0.1065$, $J - K = 1.992$, so they indeed act as normal quasars in the optical band, which is also verified by their spectra, while the dust re-emission after extinction gives rise to its extreme infrared excess. We notice that they have the highest $J - K$ values in our samples, and the $J - K$ color excess of CQ 001035.57-070232.2 is even higher than that of CQ 015957.91-061052.2 with much more severe dust extinction $A_B = 2.0$ while they have similar redshifts.

We suppose the comparable $J - K$ value of CQ 015957.91-061052.2 to these two targets is due to the fact that some dust may re-emit the radiation in a much longer wavelength, while the most fraction of the dust influencing CQ 015957.91-061052.2 belongs to such a kind, which won't contribute to the radiation in J and K bands so much. The idea is identical to what is illustrated in the dust emission model by [Draine & Li \(2007\)](#), predicting that the dust infrared emission peaks between dozens of microns to a hundred microns depending on the grain size distribution and the intensity of interstellar radiation. One simplified equation offered by [Draine \(2011\)](#) gives that the long-wavelength dust emission peak occurs at $\lambda_{peak} = 140U^{-1/6} \mu\text{m}$, in which U denotes the intensity of interstellar radiation.

Such theory can also help to explain the abnormal spectra of CQ 010339.41-132238.91, CQ 012813.63-120319.79, and CQ 121020.98+142958.5, where they don't seem to sustain any dust extinction or merely suffer from very little dust extinction. However, they have very uncommon spectra energy distributions in the blue that their spectra drop very rapidly towards the blue end, showing there must be something absorbing the emission with a short wavelength. It's not rare in our samples, and it's also discussed in Sect. 4.2 and seen in gamma-ray bursts ([Fynbo et al. 2014](#); [Heintz et al. 2017](#)). Therefore, we think there must indeed be a large amount of dust between them and us, absorbing blue light. However, the re-emission from the dust is not reflected in the near-infrared J and K bands, but in the far-infrared bands with much longer wavelengths.

For the reason why CQ 001035.57-070232.2 and CQ 003236.58-091026.2 have such high $J - K$ values, we suspect that the excess infrared emission comes from the contamination of their host galaxies. According to their spectra, our template fits quite well with them both in blue and red. However, one should be noted that the template we use to fit the low-redshift quasar is from [Vanden Berk et al. \(2001\)](#) (VB), which contains the contamination from the host galaxies as discussed in Sect. 4.2. It means that when we fit their red part together with the blue radiation well with the VB template, the quasars themselves are indeed set in the relatively bright galaxies, which contribute to their emission in the infrared. Thus, we think it's the infrared radiation from the host galaxies that makes CQ 001035.57-070232.2 and CQ 003236.58-091026.2 have

such red infrared color due to their low redshift despite the estimated small amount of dust reddening, since the quasars at lower redshift are more likely to be located in more evolved and denser galaxies with much more stellar mass (Muzzin et al. 2013). This argument can be verified by the bottom right diagram in Fig. 5.1, in which the low-redshift quasars ($z < 1$) tend to have the $J - K$ values around 2.0, forming a cluster at the bottom right corner of the diagram.

In addition, 4 out of the 5 targets near the stellar locus are stars as expected. Nevertheless, there is still one quasar in our limited samples overlapping the stellar clump, while what's more surprising and essential is that it's a very peculiar quasar, CQ 235600.19-073716.0. As discussed in the Notes on Individual Objects in Sect. 5.2, we can't really determine its redshift precisely, for its abnormal emission features and spectral energy distribution. Besides, we also find another object in our candidates, CQ 235954.08-124150.58, which resembles this one. Unluckily, we can't find the photometric data for this object, so it doesn't appear in Fig. 5.2. It's hard for us to understand the spectra of them, but we have made sure that they are not stars at least, with the help of [PyHammer](#), which is a Python program created by [Roulston et al. \(2020\)](#) for fast and automatic spectral categorization of stars and we don't find any proper fit to their spectra. Hopefully, in the future we can get them to be observed in other bands like in the infrared, to get more information about them and manage to find out their redshifts and explain their spectral features.

The appearance of a peculiar quasar on the stellar locus just highlights the shortcomings of the color criteria for selecting quasars. We could neglect so many strange but interesting quasars which may enrich our knowledge of them and the universe if we don't even bother to obtain their spectra.

In a word, it's really important for us to get as many spectra of quasars as we can, approaching a complete census of quasars, for a better understanding of the AGN, the galaxies, and the universe. Furthermore, it's also feasible with the upcoming powerful [4MOST](#), capable of surveying a large fraction of the southern sky.

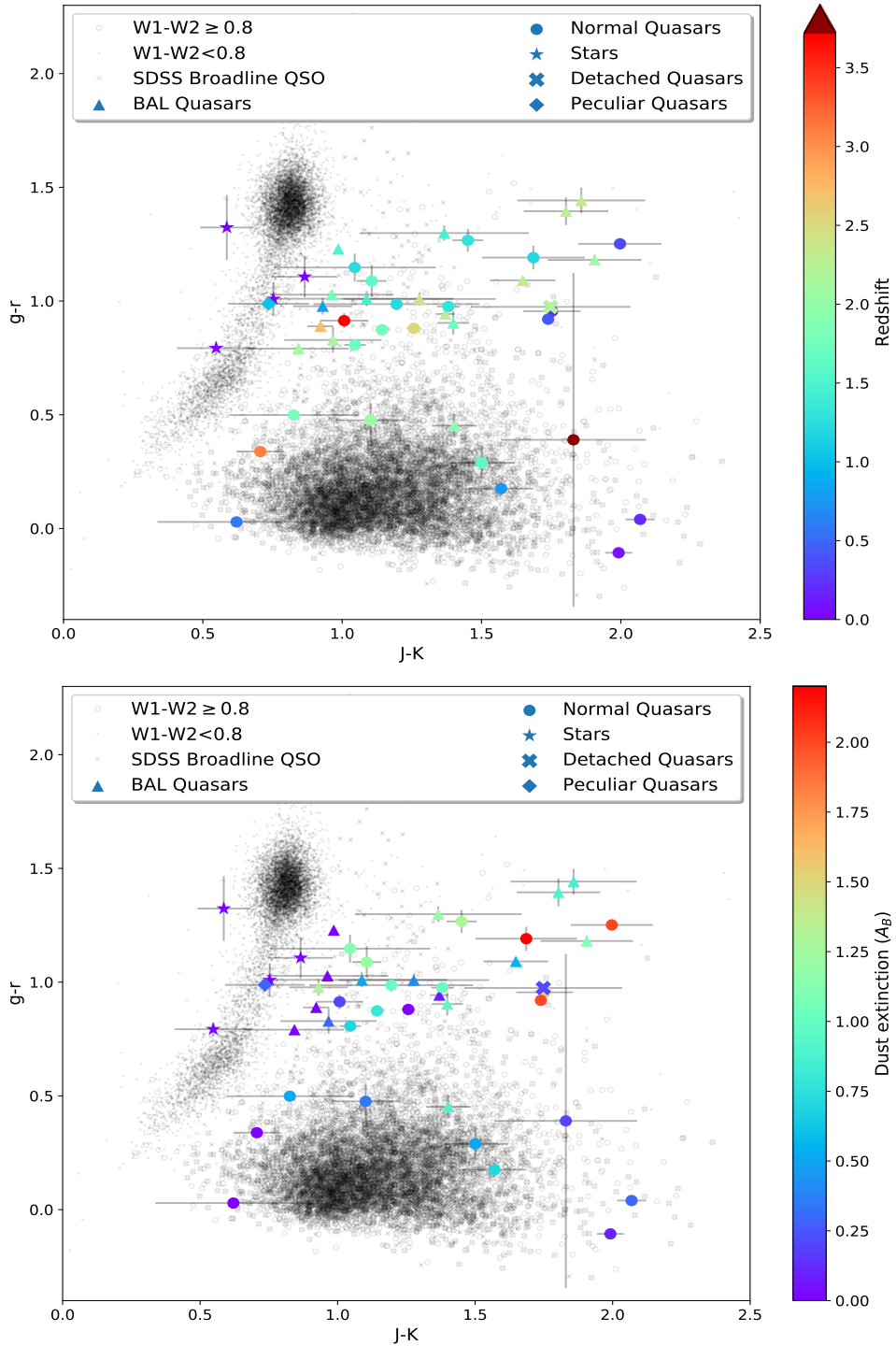


Figure 5.2: The collection of all the observed targets in this thesis, displayed on the $g - r$, $J - K$ color-color diagram, similar to Fig. 1.8 for collation, with all the objects in Fig. 1.7 plotted in black as the background to illustrate the relative positions of our selected targets to normal star and quasar groups, based on their different redshifts, dust extinction, or categories. The uncertainties of the photometry are plotted in grey error bars, calculated by $\sqrt{err(band1)^2 + err(band2)^2}$ due to their linear combinations (band1 - band2). The top panel shows the targets in different colors according to their redshifts, with one outlier plotted in dark red at redshift $z = 5.81$. The bottom panel presents our samples color-scaled by their different amount of dust extinction. Objects of different categories (for details see Sect. 1.1.5 and the following Notes on Individual Objects) are plotted in different markers as shown in the legend.

Table 5.1: The result of the best-fit parameters and spectroscopic classifications.

Target	SDSS <i>type</i>	Type	Redshift (z)	A_B
CQ 001035.57-070232.2	STAR	Normal	0.207	0.3
CQ 003236.58-091026.2	STAR	Normal	0.093	0.1
CQ 010930.72-071931.1	STAR	Detached	2.207	0.2
CQ 014434.15-014830.4	STAR	BAL	2.239	0.9
CQ 235544.91-192524.5	STAR	BAL	0.8	1.3
CQ 014541.50-163419.2	STAR	Normal	0.586	0
CQ 135305.76+255429.2	STAR	BAL	2.13	0.8
CQ 022742.93-173121.5	STAR	BAL	2.3	0.55
CQ 234859.52-193324.89	Nodata	Normal	0.45	0
CQ 000404.29-135905.43	Nodata	BAL	1.44*	1.2
CQ 003635.12-140917.41	Nodata	Normal	1.23	1.0
CQ 010013.02+280225.8	STAR	Normal	5.81	0.2
CQ 010339.41-132238.91	Nodata	BAL	1.73*	0*
CQ 012813.63-120319.79	Nodata	BAL	1.447	0.2
CQ 015957.91-061052.2	STAR	Normal	0.355	2.0
CQ 000049.99-044426.6	STAR	Normal	1.61	0.5
CQ 000337.27-004228.9	STAR	BAL	1.93	0.9
CQ 000455.89-004515.1	STAR	M5 star	0	0
CQ 000625.41-041003.7	STAR	Normal	1.195	2.2
CQ 000822.07-002302.7	STAR	Normal	3.1	0
CQ 003859.56+021008.2	STAR	M6 star	0	0
CQ 132930.98+282538.3	STAR	Normal	1.28	1.2
CQ 133639.96+282502.2	STAR	BAL	2.231	0.1
CQ 134053.89+145853.7	STAR	Normal	1.73	0.8
CQ 140513.29+060902.2	STAR	Normal	1.73	0.7
CQ 230007.30-181651.6	STAR	Normal	1.62	1.2
CQ 231242.04-083700.8	STAR	Normal	0.74	0.7
CQ 231423.51-094732.6	GALAXY	Normal	2.05	0.35
CQ 232821.99-063025.2	GALAXY	BAL	1.7*	0.95
CQ 234610.32-014557.5	STAR	M3 star	0	0
CQ 234744.54-104255.8	STAR	M5 star	0	0

Note: The SDSS *type* provided here is obtained from the [SDSS DR16 SkyServer](#), with 'Nodata' denoting that the corresponding object is not found in the SDSS DR16 archive. What are displayed together are our classifications of all the observed targets (normal quasar, detached BAL quasar, BAL quasar, peculiar quasar, and star), the best-fit redshift, and dust extinction (A_B). The values marked with * in superscripts are tentative estimates due to the low quality and limited range of observed spectra.

Table 5.1: *Continued.*

Target	SDSS <i>type</i>	Type	Redshift (z)	A_B
CQ 234930.46-053817.7	STAR	BAL	2.15	0.3
CQ 235140.03-011330.5	STAR	K3+M0 star	0	0
CQ 235807.91-011943.3	STAR	Normal	3.71	0.2
CQ 005406.43-100002.6	STAR	BAL	2.38	0.4
CQ 010002.00-030856.7	STAR	Normal	1.24	1.1
CQ 231904.59-073841.6	STAR	BAL	2.08	1.1
CQ 234530.36-135743.3	Nodata	BAL	2.325	0.85
CQ 003634.82-081425.8	STAR	Normal	1.788	0.5
CQ 005258.35-052240.2	GALAXY	Normal	0.161	1.5
CQ 021725.85-144057.31	Nodata	BAL	2.07	0.4
CQ 115341.57+060815.5	STAR	Normal	0.425	2.0
CQ 121020.98+142958.5	STAR	BAL	1.49*	0*
CQ 124154.87+255632.5	STAR	Normal	1.313	1.0
CQ 130022.82+241136.1	STAR	BAL	2.698	0
CQ 131117.99+314715.4	STAR	BAL	2.172	0
CQ 131919.56+115251.9	STAR	Normal	2.51	0
CQ 235600.19-073716.0	STAR	Peculiar	1.028**	0.3
CQ 235954.08-124150.58	Nodata	Peculiar	0.95**	0
PSS J0141+3334	Nodata	Detached	3.32	0.1

Note: The redshifts marked with ** in superscripts are tentative estimates due to the absence of emission lines in their spectra matching well with the template.

5.2 All Spectra

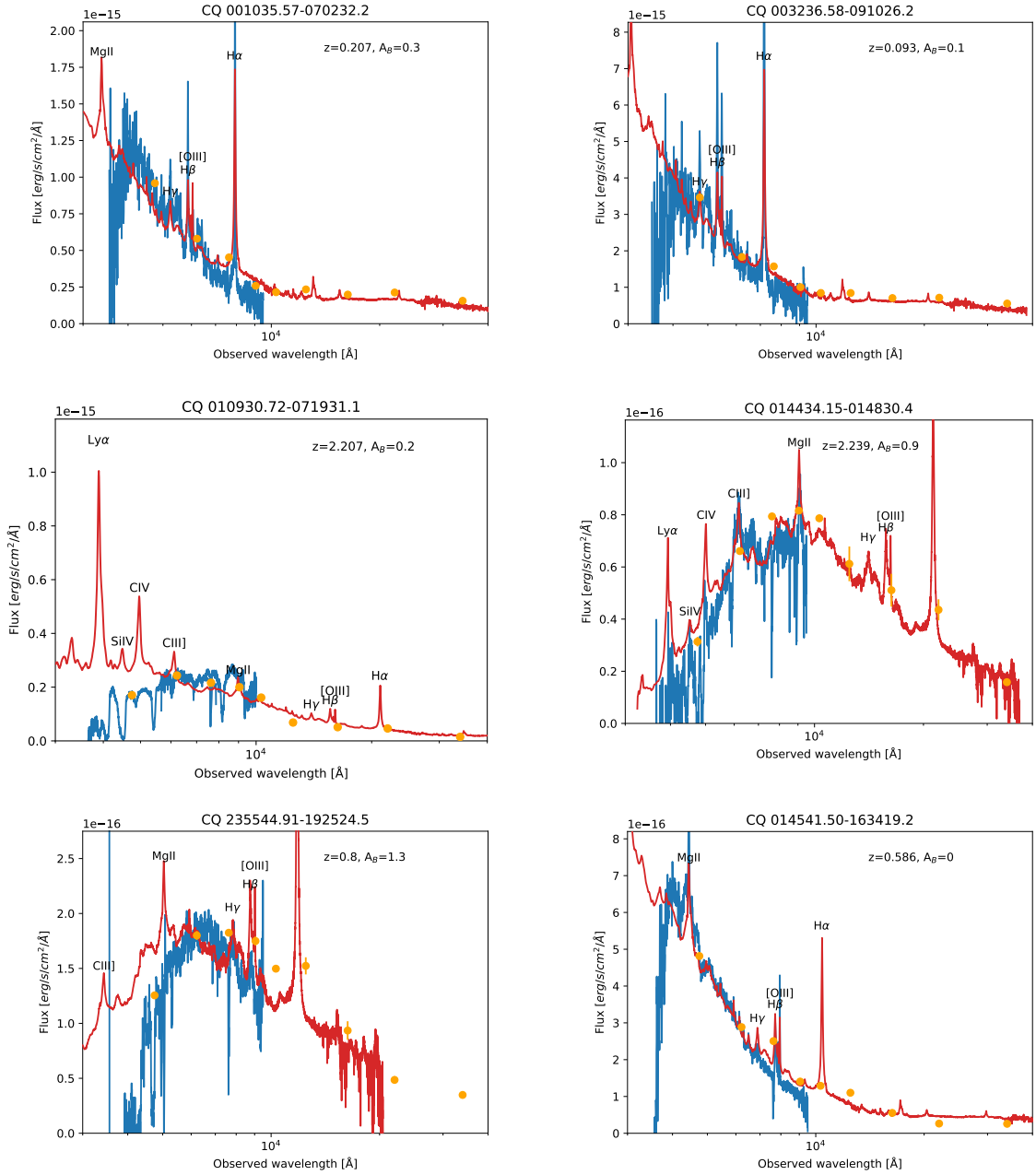


Figure 5.3: One-dimensional spectra for all the selected quasar candidates observed in this thesis, showing the flux distribution in the observed wavelengths. For every candidate, the observed spectrum is plotted in blue, our best-fit spectrum in red, and the retrieved photometry from different datasets (for more details see Sect. 4.3) in orange dots with error bars illustrating the errors in their magnitudes. The best-fit spectrum is the quasar composite template (for more details see Sect. 4.2) redshifted to the estimated redshift and reddened by the inferred dust extinction at the photometric B band (A_B) assuming an SMC-like extinction curve (see Sect. 4.1.5). Note that all the telluric absorption lines (atmospheric absorption features) in the spectra are not corrected, appearing around 6860 \AA (B-band) and 7600 \AA (A-band).

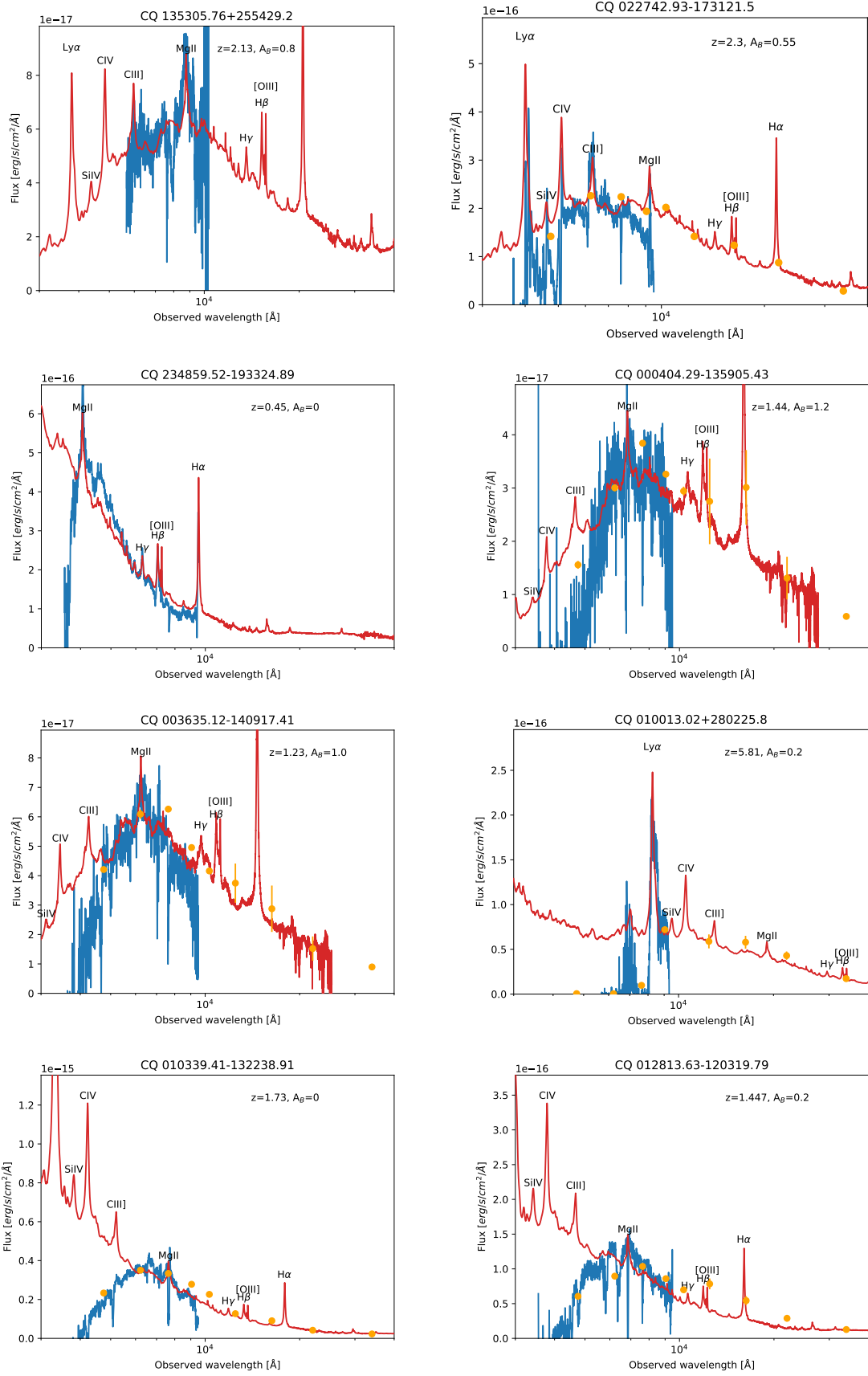


Figure 5.3 (Continued): One-dimensional spectra for all the quasar candidates observed in this thesis.

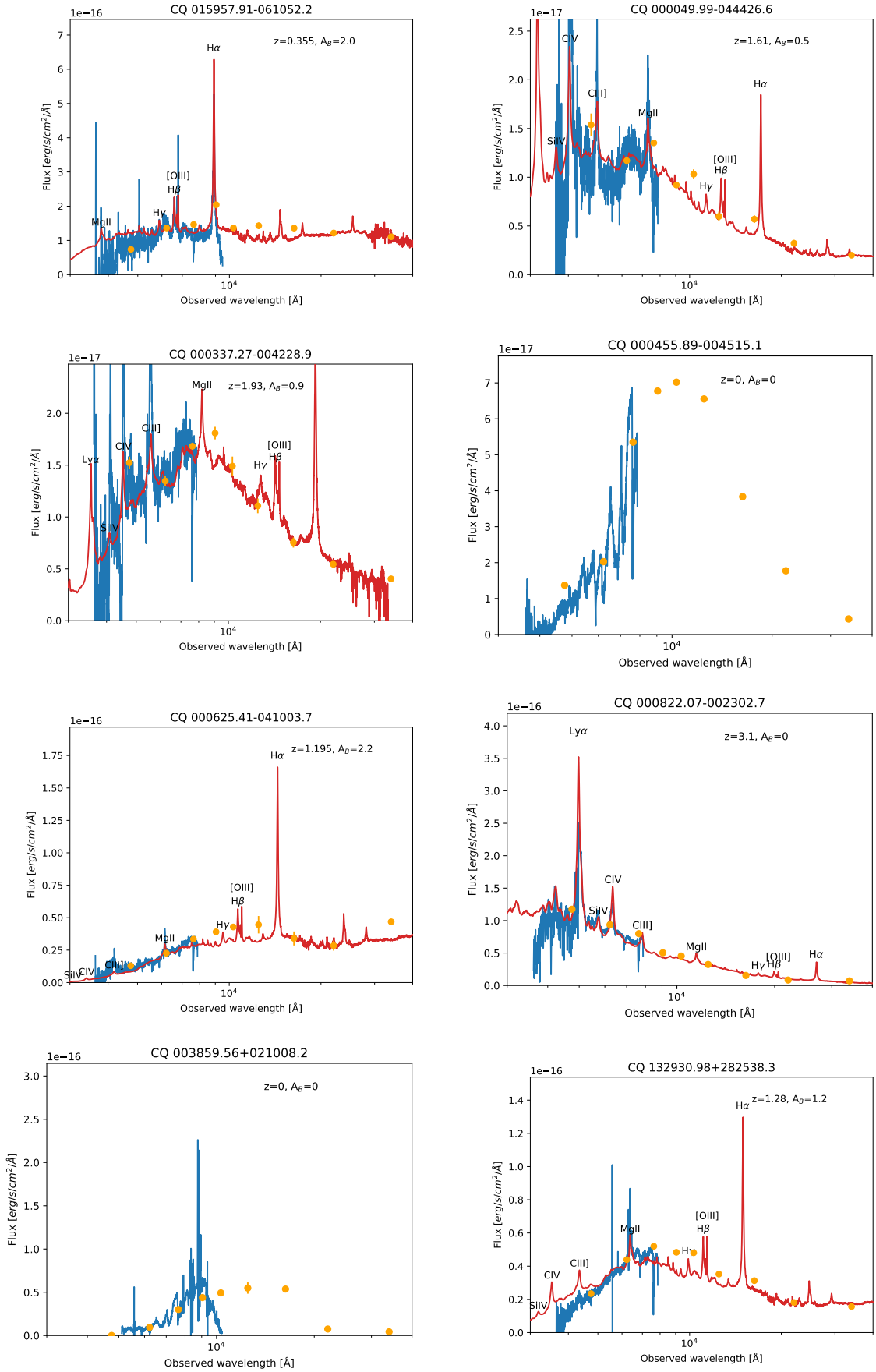


Figure 5.3 (Continued): One-dimensional spectra for all the quasar candidates observed in this thesis.

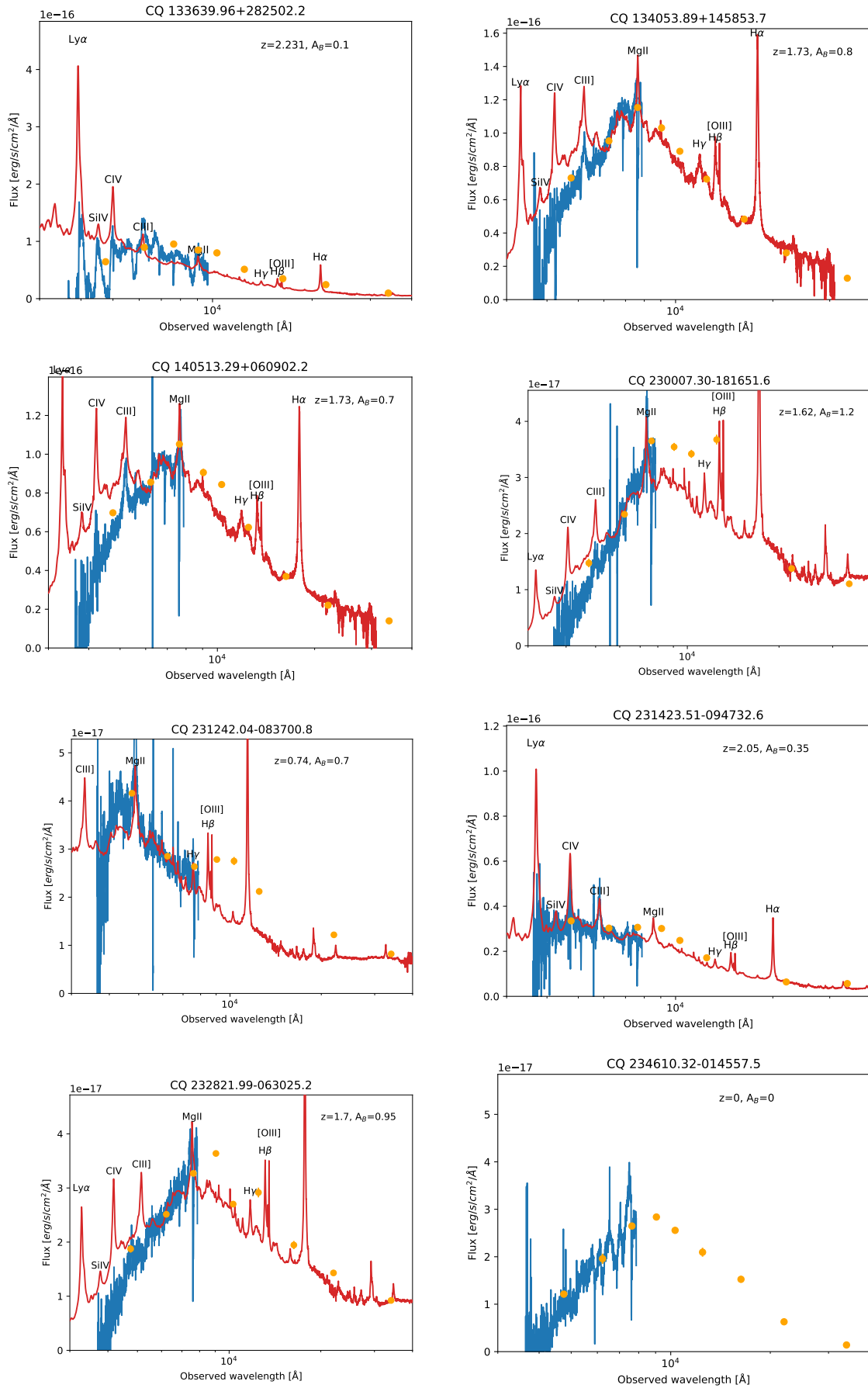


Figure 5.3 (Continued): One-dimensional spectra for all the quasar candidates observed in this thesis.

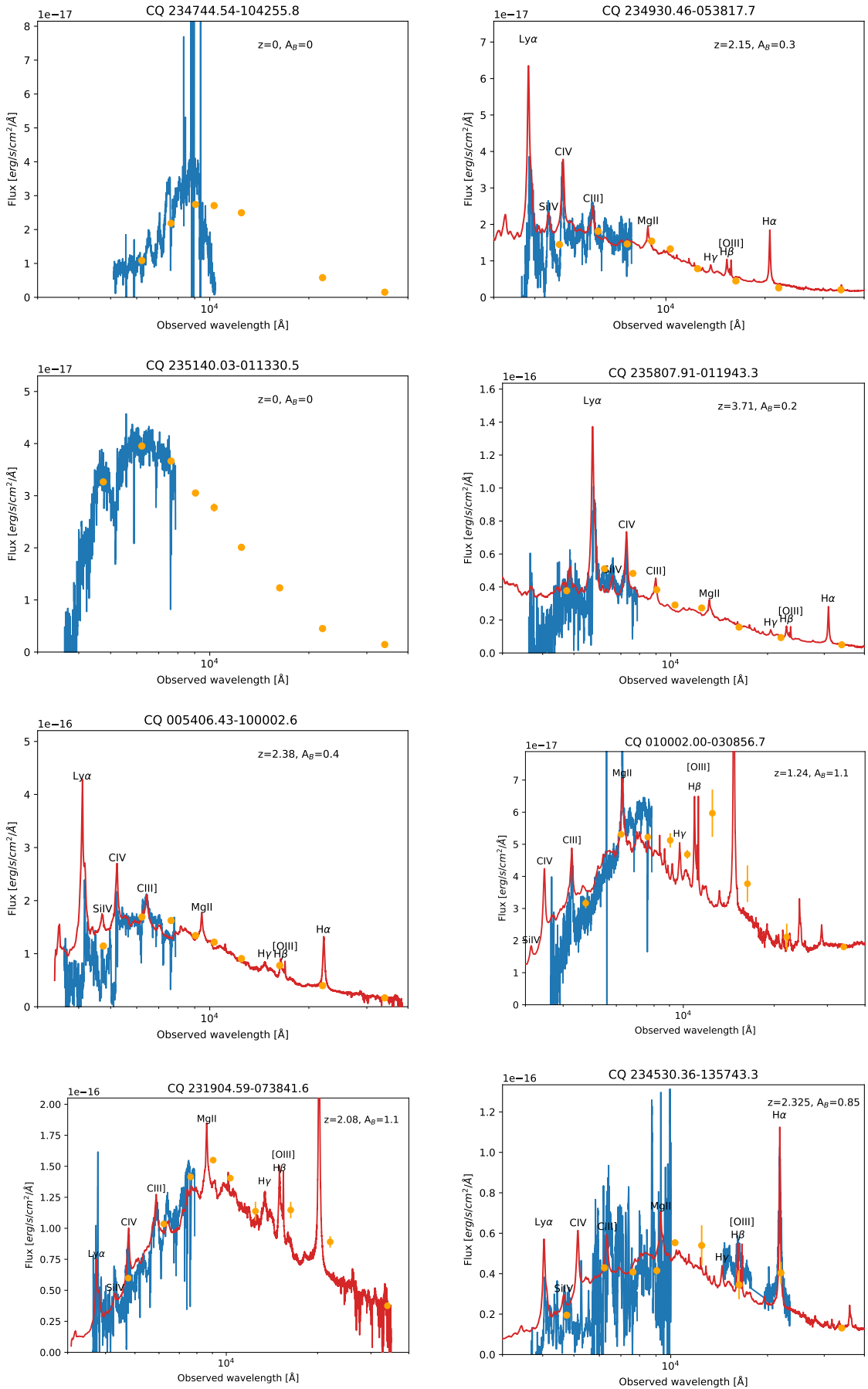


Figure 5.3 (Continued): One-dimensional spectra for all the quasar candidates observed in this thesis.

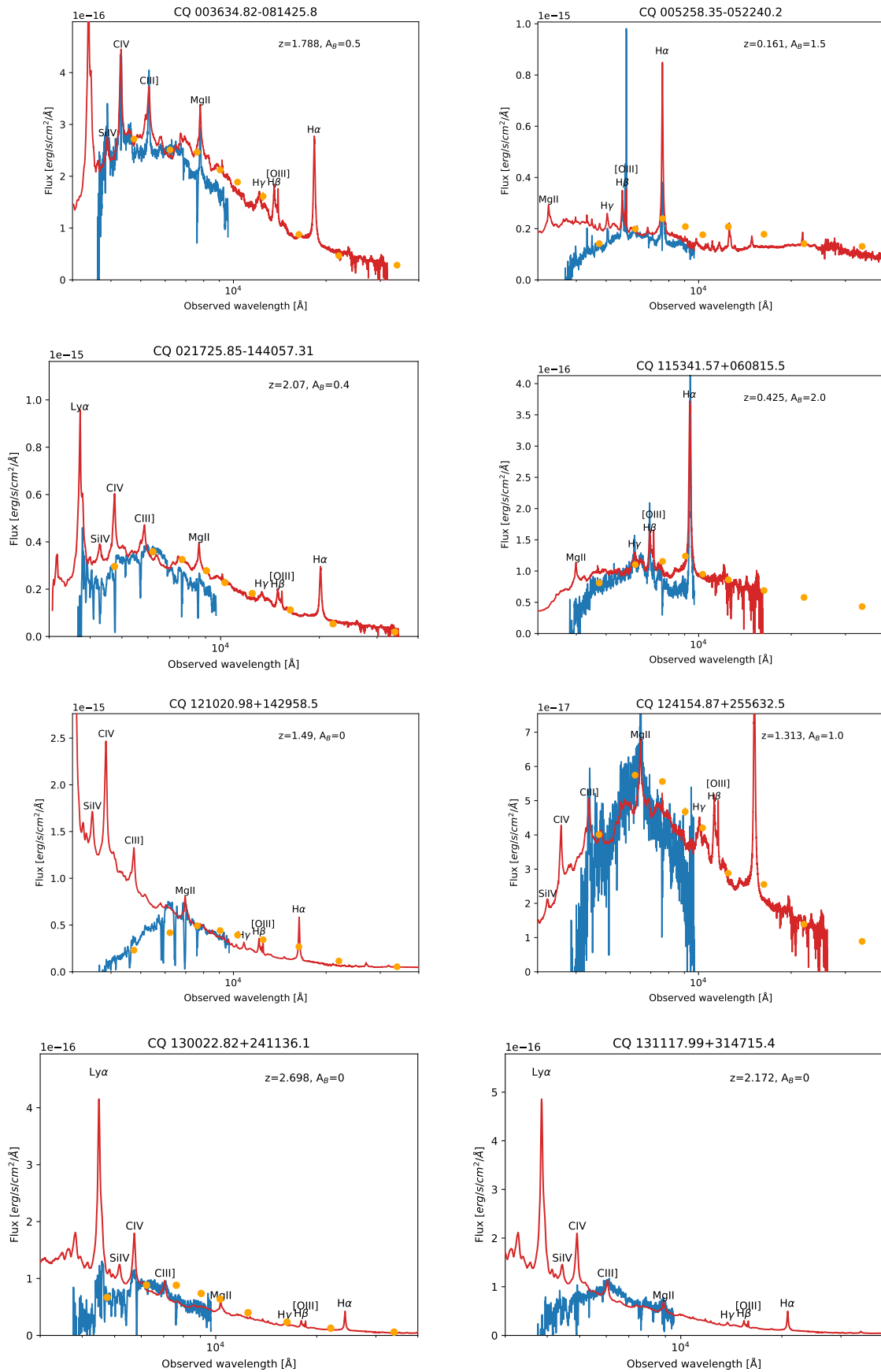


Figure 5.3 (Continued): One-dimensional spectra for all the quasar candidates observed in this thesis.

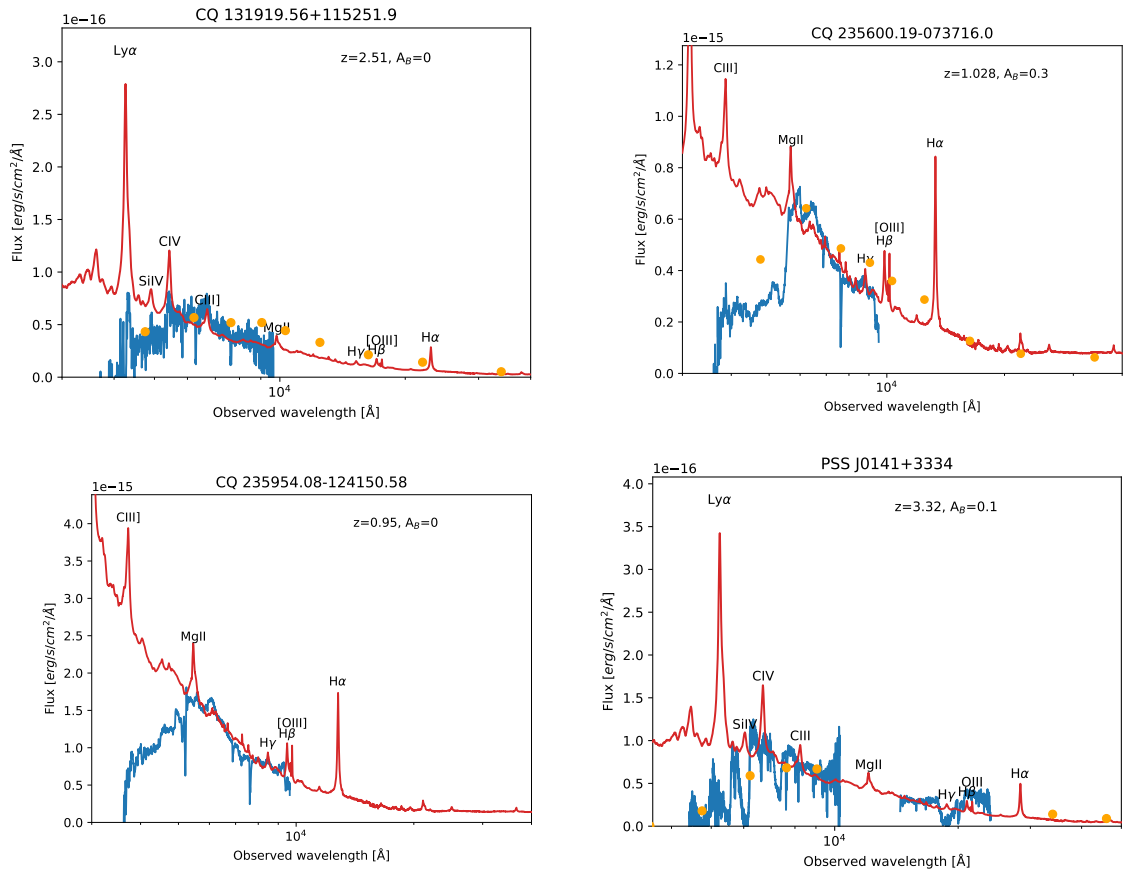


Figure 5.3 (Continued): One-dimensional spectra for all the quasar candidates observed in this thesis.

Notes on Individual Objects

Here we present the detailed spectral fitting process for every observed target, giving reasons for our choice of classifications and measurement of redshift and amount of dust extinction. Besides, the analysis of special features in the spectra is also elaborated. A separate discussion on the detached BAL quasars is stated in detail in Sect. 5.3.

CQ 001035.57-070232.2 ($z = 0.2071$)

This is a quasar at $z = 0.2071$, which is determined based on the presence of the Balmer series ($H\alpha$, $H\beta$, and $H\gamma$). It's a bit dust-reddened with an estimated extinction of $A_B = 0.3$, which provides a good match both to the observed spectrum and the reference photometry. However, without including the Mg II line and the C IV line in our optical spectrum due to its relatively low redshift, we tentatively label it as a normal quasar. While it's labeled as a star in the SDSS object explorer.

CQ 003236.58-091026.2 ($z = 0.0928$)

This object is a quasar with a lower redshift at $z = 0.0928$, derived from the prominent Balmer lines one can easily see in the spectrum. Different from CQ 001035.57-070232.2, it also has the obvious [O III] lines, which may indicate a much more diffuse environment and a more evolved state due to the appearance of the forbidden lines and oxygen. By assuming the dust extinction to be $A_B = 0.1$, we match the template well with the target's spectrum and photometric data. It's labeled as the normal quasar for the same reason as previously mentioned, although the SDSS still marks it as a star.

CQ 010930.72-071931.1 ($z = 2.2069$)

This one is a relatively high redshift quasar at a speculative estimation of the redshift $z = 2.2069$, the deduction and determination of which is elaborated in Sect. 5.3. We combined the spectra obtained with grism 4 and grism 19 from the NOT, to make it cover a larger wavelength range. However, there is still no clear evidence for us to identify any natural emission line of the quasar. Based on the absence of emission lines and the separation of absorption lines and 'assumed' emission lines which are different from the P Cygni profile (named after P Cygni, whose spectrum shows the combination of emission lines with connected blueshifted absorption lines) of common BAL quasars, we label it to be a detached BAL quasar, while it's classified as a star by the SDSS. We fit the dust extinction to be $A_B = 0.2$, mainly for matching the infrared photometry,

leaving the blue part of the spectrum badly fitted since we would assume a steeper UV extinction here than the normal SMC-like extinction curve we use, as described in Sect. 4.2.

CQ 014434.15-014830.4 ($z = 2.2394$)

This target is also a quasar at a fairly high redshift ($z = 2.2394$) in our samples. By assuming the emission line at around 9000 \AA as the Mg II line, we find the other lines like C III] or C IV match quite well with the spectral features, and Ly α and Si IV lines are at the appropriate position although there is a bit low reliability for the presence of emission lines there. We label this object as a BAL quasar according to the absorption lines beside the Mg II, C III], and C IV lines, showing it to be a LoBAL quasar more specifically, although all the absorption lines seem to be very narrow, which is actually because wavelengths of all the figures are displayed in the log scale. We obtain the estimated amount of dust extinction to be $A_B = 0.9$, which is a quite high value, indicating that it's a heavily dust-reddened quasar. With the proposed extinction value, we fit the blue spectrum and red photometry nicely. The SDSS flag of it is 'STAR'.

CQ 235544.91-192524.5 ($z = 0.8$)

The quality of this object's spectrum is not so good and it's hard for us to see any significant broad absorption lines. After assuming the lines at around 7900 \AA and 8800 \AA to be H γ and H β , we happened to find that the Mg II line match perfectly with the emission line at about 5000 \AA . Moreover, we check the firmly identified Fe II absorption lines in BAL quasars from [Hall et al. \(2002\)](#) with many strange absorption lines in this spectrum, which we find can be fitted quite well, confirming our estimation for the redshift. Therefore, we give our best-fit redshift of this object being $z = 0.8$ and the dust extinction being $A_B = 1.3$. Note that we use the template from [Selsing et al. \(2016\)](#) to fit this low-redshift quasar, for it's a better match to the entire spectrum, showing the absence of contamination from its host galaxy. It's not a very bright quasar, indicating that its host galaxy is even much fainter. This may hint that the host galaxy has been quenched, leaving a large amount of dust shrouding the quasar. Clearly, there is still something happening in the blue, producing a divergence between our best-fit model and the observed spectrum. It can be due to the need for an extinction curve with a much steeper UV extinction as discussed in Sect. 4.2 or this quasar is intrinsically different from those used to composite the template. In addition, such a rapid drop of the spectrum towards the blue end is also seen in the afterglow of gamma-ray bursts, discussed by [Fynbo et al. \(2014\)](#) and followed by [Heintz et al. 2017](#)). We think it's a

BAL quasar since if its redshift is correct, there is an obvious absorption line blueward of the Mg II line, making it be a LoBAL quasar. It's marked by the SDSS to be a star.

CQ 014541.50-163419.2 ($z = 0.58562$)

This object is a normal quasar at the redshift $z = 0.58562$, with the appearance of Mg II, H γ , H β , [O III] lines in the spectrum. The template we used is a perfect match to this spectrum, fitting well with even the smallest structure and we find no dust extinction features in this quasar, which is flagged to be a star in the SDSS database. We believe the rapid drop of the spectrum at the blue end is not originated from something really happening in or around the quasar other than the bad function of the CCD at the very blue side. It's a normal quasar with regard to the wavelength range we observed, although the possibility for it to be a HiBAL is not excluded since the high ionization lines are not within our spectrum.

CQ 135305.76+255429.2 ($z = 2.13$)

This one is taken with grism 19 of the ALFOSC in the NOT, so unfortunately very few real emission lines appear in the spectrum. We suspect the line around 9000 Å to be the Mg II line and there is an emission line at the bluest part of this spectrum that has exactly the same wavelength as that of C III] predicted by the template, making the estimated redshift be $z = 2.13$, although the SNR here is not so good. We also set the preliminary extinction amount to be $A_B = 0.8$, to fit the spectrum as well as possible with the fact that we can't find the infrared photometry of this object in all the catalogs and databases. It can be found in the SDSS with a type of 'STAR', but because of the lack of its infrared photometric data (especially at the J and K bands), it's not plotted in Fig. 5.2 color-color diagram. According to the existence of an absorption line connected with the Mg II line at the wavelength longer than 8000 Å, making sure that it doesn't belong to the telluric lines, it's thought to be a LoBAL quasar.

CQ 022742.93-173121.5 ($z = 2.3$)

This is a classic LoBAL quasar at $z = 2.3$ as we can easily identify the common emission lines of the quasar from Ly α to Mg II and the broad absorption lines associated with basically all the present emission lines. By assuming the extinction to be $A_B = 0.55$, we fit the spectrum and photometric data points well, except few parts such as that redward of the C IV line and blueward of the Mg II line, which may indicate a possible influence from the 2175 Å extinction bump of the dust in the potential intervening systems that

is not considered in our SMC-like extinction curve. It's regarded as a star in the SDSS server.

CQ 234859.52-193324.89 ($z = 0.4504$)

This is a normal quasar with a spectrum very similar to that of CQ 014541.50-163419.2, located at $z = 0.4504$ according to the existence of the same emission lines in the wavelength range of grism 4. Nevertheless, we don't have any photometric data on this object, although it ought to be not affected by any dust extinction based on its spectrum barely. Therefore, this target isn't displayed in Fig. 5.2 as well.

CQ 000404.29-135905.43 ($z = 1.44?$)

This one is very similar to CQ 135305.76+255429.2, however, with a much worse SNR. Considering the emission line at about 7000 \AA together with the enhancement of the magnitude of J and H bands, we propose the redshift of it to be at $z = 1.44$, by fitting the mentioned emission line with Mg II. It's just a preliminary guess since there isn't a good match of several abnormal absorption lines with the Fe II absorption lines from [Hall et al. \(2002\)](#), which all have shorter wavelengths than predicted by the line list, although it can be interpreted as Fe II absorption in the outflow. Nonetheless, the uncommon increase in the magnitude of J and H bands can then be interpreted as the existence of high-intensity $H\beta$ and $H\alpha$ lines within the bandwidth of the corresponding filter. We estimate the amount of extinction to be $A_B = 1.2$, matching the infrared photometry more, while we can see that it looks like CQ 235544.91-192524.5 in the blue part, with a similar amount of dust extinction. As a result, the spectra of them may be generated by a similar process. This object can't be found in the SDSS database, and we give it a preliminary label of being a BAL quasar, as there is an obvious absorption line blueward of the Mg II line despite the large noise.

CQ 003635.12-140917.41 ($z = 1.23$)

The target resembles the last one CQ 000404.29-135905.43, at a slightly lower redshift $z = 1.23$, fitting the most significant emission line in the spectrum near 6000 \AA with the Mg II line, and the] line can match the potential emission line at the corresponding wavelength if it's not generated by the noise. With the assuming redshift, we fit the dust extinction to be $A_B = 1.0$, tuned to the infrared photometry, while the template

also has exceeding blue emission than the observed spectra similar to CQ 000404.29-135905.43. Besides, it's not observed by the SDSS, either. Based on the fact that there is no obvious absorption line existing, we classify it to be a normal quasar.

CQ 010013.02+280225.8 ($z = 5.81$)

This object has the highest redshift in our samples, which is located at $z = 5.81$. A very obvious Gunn–Peterson trough can be seen in the spectrum (Gunn & Peterson 1965; Becker et al. 2001), indicating the most significant emission line in the spectrum to be $\text{Ly}\alpha$. Besides, the higher $\text{Ly}\beta$ residuals than those at $z \gtrsim 6$ show that there are much fewer neutral hydrogen atoms in the space at the redshift $z < 5.81$ since lots of them have been re-ionized, displaying the process of reionization in the early universe. However, the appearance of the Gunn–Peterson trough implies that there is still an appreciable amount of neutral gas left, demonstrating that the reionization doesn't end at $z < 5.81$, which agrees with the statement from Zhu et al. (2021) suggesting that the reionization is still in progress until at least $z \simeq 5.3$. We measure the amount of dust extinction to be $A_B = 0.2$ in agreement with the photometric data. We tentatively set its type to be a normal quasar since no absorption lines appear in the optical spectrum due to its high redshift, while the SDSS categorizes it to be a star.

CQ 010339.41-132238.91 ($z = 1.73?$)

This object is not included in the SDSS database, while we think it's a BAL quasar based on the P Cygni configuration of C III] in the spectrum, by fitting the emission line near 7600 \AA with the Mg II line assuming it's correct, to determine the tentative redshift of this object being $z = 1.73$. Unfortunately, the telluric lines happen to overlap with the Mg II line, so we are not able to confirm whether it's a LoBAL or not. However, it's more likely to be a HiBAL since the absence of absorption lines at the left of the blue wing of the Mg II line. With the help of the infrared photometry, we think there is no dust extinction ($A_B = 0$) along the line of sight from it to us, making it impossible to attribute the discrepancy between the template and the spectrum to the need for a much steeper UV extinction line. However, it's indeed a quasar, not a star, showing that the peak of its radiation at about 6500 \AA is not intrinsic, since we have fitted this object by using the PyHammer and no proper fitting result is found. Besides, the abnormal decrease in the blue part is seen in the spectrum of CQ 235544.91-192524.5, but it's even much more severe in this case. We suspect that this object is actually obscured heavily by the dust, making its spectrum in the blue diminished severely, while the dust there may re-emit in a much longer wavelength ($100 \mu\text{m}$) as demonstrated in Sect. 5.1, which is

not included in the wavelength range we are investigating. Thus, the estimation of dust extinction to be $A_B = 0$ is very tentative and may be proved to be wrong if we can get its spectrum or photometric data at a much longer wavelength in the far-infrared. There is also possibility for it to be a weak line quasar (Leighly et al. 2007; Diamond-Stanic et al. 2009; Hryniewicz et al. 2010).

CQ 012813.63-120319.79 ($z = 1.4468$)

This target can't be found in the SDSS server, either. By identifying the broad emission feature around 7000 \AA with the Mg II emission line, with the influence from the B-band ($6860 - 6890 \text{ \AA}$) telluric line, we derive its redshift to be $z = 1.4468$ and classify it being a LoBAL quasar for the apparent blueshifted Mg II absorption line. The approximate amount of extinction is proposed to be $A_B = 0.2$, leaving the distinction between the template and observed spectrum which is similar to that of CQ 235544.91-192524.5. Moreover, this spectrum looks quite similar to the last one CQ 010339.41-132238.91, giving each other the evidence for their estimation of redshifts to be both correct (or wrong). Therefore, it's also possible for this object to be a weak line quasar.

CQ 015957.91-061052.2 ($z = 0.3555$)

With noticing the conspicuous $H\alpha$ line, we easily measure the redshift of this object to be $z = 0.3555$, making the other lines (e.g. $H\beta$; [O III]) in the model consistent with the emission features in the observed spectrum. The estimated dust extinction amount is derived to be $A_B = 2.0$, owing to the high flux in the infrared deduced from the photometry results, showing that this object is extremely dust-obscured, with the second greatest value of A_B among our samples. This target is labeled as a star by the SDSS, while we provisionally set its flag to be a normal quasar due to the lack of observations of the high and low ionization lines in our spectrum.

CQ 000049.99-044426.6 ($z = 1.61$)

We determine the redshift of this object to be $z = 1.61$ by fitting the obvious emission line near 7300 \AA with the Mg II emission, making other emission lines well-fitted as well. After assuming the extinction coefficient to be $A_B = 0.5$, we success in fitting the spectrum and photometry simultaneously. Because there are no noticeable blueshifted absorption lines connected to the present species, we tag it to be a normal quasar, while it's marked to be a star by the SDSS.

CQ 000337.27-004228.9 ($z = 1.93$)

The spectrum of this object looks very similar to the last one, thus we easily locate the C III] emission line at around 5600 \AA and fit others accurately by assuming the redshift to be $z = 1.93$. Spotting the absorption lines blueward of C IV and C III] lines, this object ought to be a BAL quasar, despite the 'STAR' type from the SDSS. Likewise, we fit the entire continuum nicely, with the measured extinction to be $A_B = 0.9$.

CQ 000455.89-004515.1 ($z = 0$)

With the absence of any clear broad emission lines plus the stellar black body radiation curve inferred from the photometry, we presume it to be a star, with more evidence from the appearance of an apparent absorption line at around 5800 \AA , which is the sodium absorption line commonly seen in stars' spectrum. Thus, we fit it with the automatic stellar spectral classification tool, PyHammer, and confirm that it's an M5 star, identical to its classification in the SDSS. The result of PyHammer fitting is shown in Fig. 5.4.

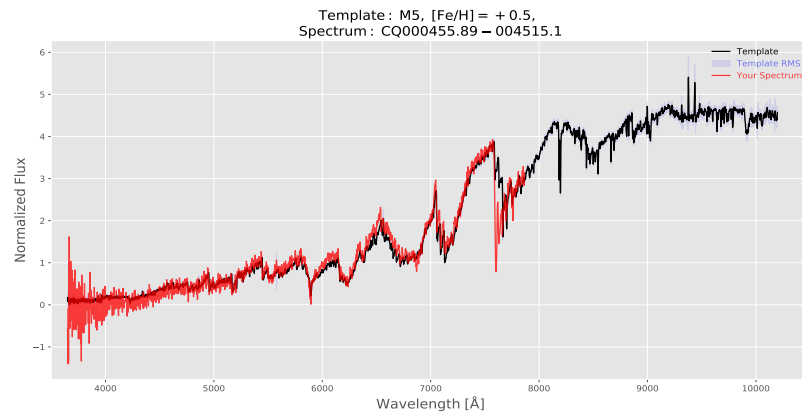


Figure 5.4: The PyHammer fitted spectrum of CQ 000455.89-004515.1, authenticating it to be an M5 star.

CQ 000625.41-041003.7 ($z = 1.195$)

By assuming the emission line at about 6100 \AA to be the Mg II line, we determine the redshift of this candidate to be $z = 1.195$, which can be verified by the existence of an emission line at the wavelength of the C III] line predicted by the template. The proposed amount of dust extinction is $A_B = 2.2$, implying this object suffers the most severe dust reddening, derived by fitting the template to the continuum of the spectrum

and the photometry. Due to the fact that no clear broad absorption lines are observed in this spectrum, we mark it as a normal star, different from its SDSS flag being a star.

CQ 000822.07-002302.7 ($z = 3.1$)

With an apparent indication of the presence of Ly α forest, it's very natural to fit the prominent emission line near 5000 Å with the Ly α line, setting the redshift of this object to be $z = 3.1$. The perfect match of Si IV and C IV lines with the emission features in the spectrum corroborates this redshift assumption. The template without any extinction precisely fits the entire wavelength range from UV to mid-infrared, so the dust extinction is supposed to be $A_B = 0$. We classify this object to be a normal quasar, although there seems to be an absorption line blueward of C III], which is not generated by the quasar. In fact, it's just the A-band telluric line always appears at 7600 - 7630 Å. This target is marked as a star by the SDSS.

CQ 003859.56+021008.2 ($z = 0$)

This object is also a star, although it suffers much more noise than the previous one, making the sodium absorption line not obvious. However, from the big troughs and the maximum of photometric values at a much larger wavelength than that of the quasars, we suppose that this target is a star, which is substantiated by the PyHammer fitting result showing it to be an M6 star, as displayed in Fig. 5.5. The peak of its radiation at a longer wavelength than that of CQ 000455.89-004515.1 also confirms that it's cooler than CQ 000455.89-004515.1, as described in Sect. 4.1.3. This classification is also the same as that from the SDSS.

CQ 132930.98+282538.3 ($z = 1.28$)

We fit the redshift of this object to be $z = 1.28$, by regarding the only apparent emission line in the spectrum as the Mg II line, which makes the model predicted C III] line match the shallow emission feature at around 4400 Å. As we don't see any broad absorption line in the spectrum, we categorize this target as a normal quasar, with a relatively high dust extinction amount $A_B = 1.2$, adapting the template to coincide with the spectrum in the blue and photometry in the red. Its SDSS type is 'STAR'.

CQ 133639.96+282502.2 ($z = 2.231$)

This is a very typical BAL quasar, with the appearance of broad absorption lines beside every high ionization emission line in this spectrum. Based on such features plus the

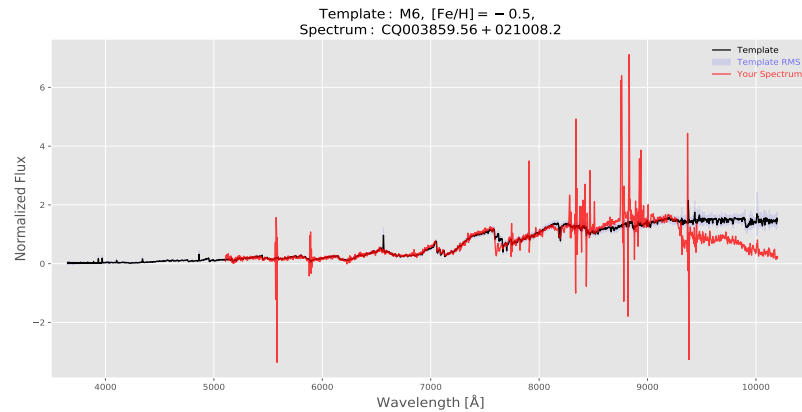


Figure 5.5: The PyHammer fitted spectrum of CQ 003859.56+021008.2, authenticating it to be an M6 star.

emission line with the highest intensity situated at the shortest wavelength (the one at around 4000 \AA), it's very reasonable to identify it as the $\text{Ly}\alpha$ line. As a result, we obtain the redshift being $z = 2.231$. After comparing the template with the infrared photometry, we estimate the dust extinction to be $A_B = 0.1$, which makes the template match the spectrum at the shorter wavelengths as well. It's flagged by the SDSS to be a star.

CQ 134053.89+145853.7 ($z = 1.73$)

The spectrum of this object is very similar to that of CQ 010339.41-132238.91, although there is a big difference in the consistency between their template and spectra. In the same manner, we fit the obvious emission feature at 7600 \AA with the Mg II line, embedded with the telluric line at the same wavelength. We obtain the redshift of this target to be $z = 1.73$, which is the same as that of CQ 010339.41-132238.91. However, the radiation from the intervening dust is much more significant in the near-infrared and mid-infrared for this object, which helps us to determine the total extinction at the B band to be $A_B = 0.8$, while there is a little mismatch between the model and the spectrum, which may be attributed to the same reasons as discussed in the note of CQ 235544.91-192524.5. It's a normal quasar since no broad absorption lines are present in the spectrum, although it's classified as a star by the SDSS.

CQ 140513.29+060902.2 ($z = 1.73$)

This spectrum looks very similar or even mostly the same as the last one, with a more apparent C IV emission line at around 4200 \AA , and it happens to have the same redshift

as the last object CQ 134053.89+145853.7 to be $z = 1.73$. What is more surprising is that even the overall continuums of them are extremely alike, so we get the same estimated amount of dust extinction being $A_B = 0.7$ for this object as well. Besides, it's also a normal quasar while its SDSS flag is "STAR".

CQ 230007.30-181651.6 ($z = 1.62$)

This object also has a similar spectrum to the previous targets, so it's very natural to fit the emission line at around 7400 \AA with the Mg II line, estimating the redshift to be $z = 1.62$. Such redshift measurement gives the rest emission lines (C III] and possibly C IV) in the template a good match to the emission features in the observed spectrum. The unusual infrared photometry rise in the continuum can also be explained by the redshifted Balmer lines falling in the corresponding filters. However, the relatively high intensities of mid-infrared photometry show that this object is somewhat highly dust reddened ($A_B = 1.2$). We label this object being a normal quasar for no clear signs of broad absorption lines, while it's a star in the SDSS server.

CQ 231242.04-083700.8 ($z = 0.74$)

This candidate is a normal quasar obscured by a bit high dust extinction ($A_B = 0.7$), situated at $z = 0.74$ by locating the Mg II emission line at the wavelength around 4800 \AA . The tiny emission lines in the model also fit different emission spikes in the spectrum quite precisely, making the redshift guess credible. We tentatively categorize it to be a normal quasar although the spectrum showing high ionization lines are not included. It's marked as a star in the SDSS object explorer.

CQ 231423.51-094732.6 ($z = 2.05$)

The SNR of this spectrum is not very ideal, making it a little cluttered. However, the main emission features are still clear, from which we can easily find the indication of a sequence of UV emission lines in the rest-frame template. By fitting the broad emission line at approximately 5800 \AA with the C III] line, we derive the redshift being $z = 2.05$. The Ly α line in this spectrum is quite blurred, which may be due to the bad spectral quality of the CCD in the very blue end, but the overall emission shape is present. We measure the amount of extinction to be $A_B = 0.35$ by fitting the infrared photometry and the observed spectrum in the blue consistently at the same time. Because we don't see any plausible evidence for the appearance of broad absorption lines associated with

the emission features, we tag it to be a normal quasar, while it's classified as a galaxy by the SDSS surprisingly.

CQ 232821.99-063025.2 ($z = 1.7?$)

It's also a galaxy in the SDSS database, and we admit that there isn't any very clear emission feature in the spectrum. However, we suppose that there is a possible broad emission line at around 7600 \AA , unfortunately, embedded with the A-band telluric line, making it not palpable anymore. We speculative fit it with the Mg II line to determine the tentative redshift being $z = 1.7$, making the absorption troughs in the spectrum located at the wavelengths where the C IV and C III] should be. Moreover, if we are correct, the absorption line blueward of the Mg II signalizes the BAL quasar nature of this object. In addition, the dust extinction is measured to be $A_B = 0.95$, fitting the infrared photometry.

CQ 234610.32-014557.5 ($z = 0$)

With a noticeable sodium absorption feature in the spectrum and the stellar photometry configuration, we consider the possibility for it to be a star and then fit it using the PyHammer scripts, which categorizes it to be an M3 star, as illustrated in Fig. 5.6, agreeing with the SDSS type.

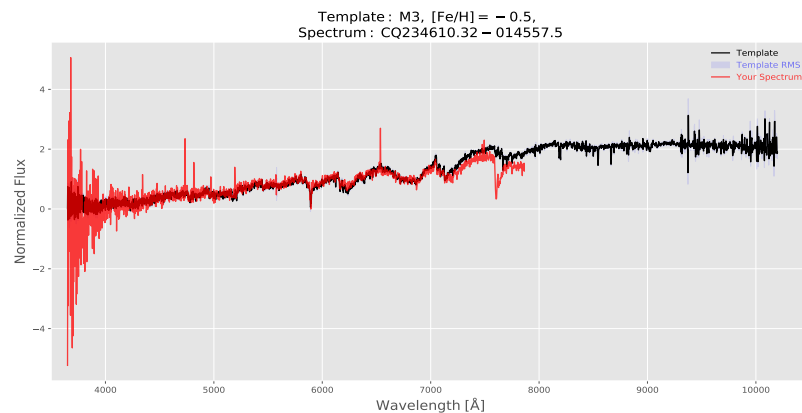


Figure 5.6: The PyHammer fitted spectrum of CQ 234610.32-014557.5, authenticating it to be an M3 star.

CQ 234744.54-104255.8 ($z = 0$)

With similar signatures to the last object, we quickly recognize it as a star, which is verified by the PyHammer to be an M5 star, with annoying noise in the red wavelengths. The fitted spectrum is given in Fig. 5.7, confirming the classification from the SDSS.

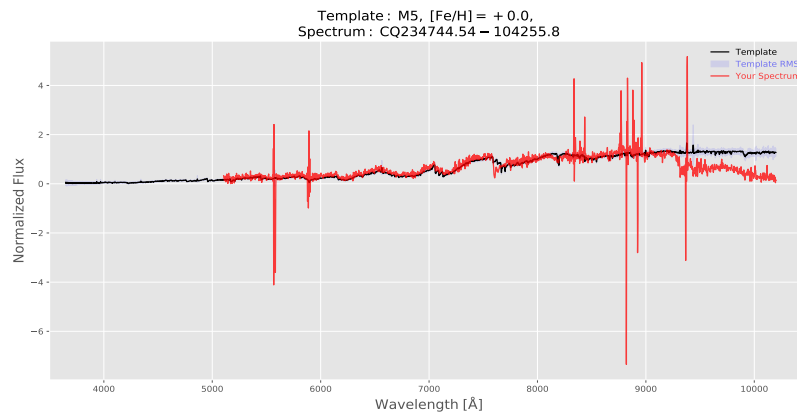


Figure 5.7: The PyHammer fitted spectrum of CQ 234744.54-104255.8, authenticating it to be an M5 star.

CQ 234930.46-053817.7 ($z = 2.15$)

The spectrum shows the very representative absorption features of a BAL quasar, easing our attempt to identify the emission lines. We calculate the redshift to be $z = 2.15$, by placing the Ly α line at the emission around 4000 Å. We also fit the entire continuum from the UV to infrared fairly well with the assumed extinction $A_B = 0.3$. It's labeled as a star by the SDSS.

CQ 235140.03-011330.5 ($z = 0$)

This object's spectrum actually seems very special since the feature at around 5700 Å is very likely to be a broad emission line. However, we can't match it with any existing emission spike in our template to make sure the rest emissions are fitted well with the other spectral characteristics in the observed spectrum. Therefore, based on the possible sodium absorption line at 5800 Å and the black-body alike photometry, we come up with an idea that this target is a star, which is later confirmed by the PyHammer fitted spectrum, showing it to be the potential binary stars composed of a K3 star and an M0 star. The output of the program is presented in Fig. 5.8, proving it to be the hottest star among the stars we observed. The SDSS also sorts it correctly as a star.

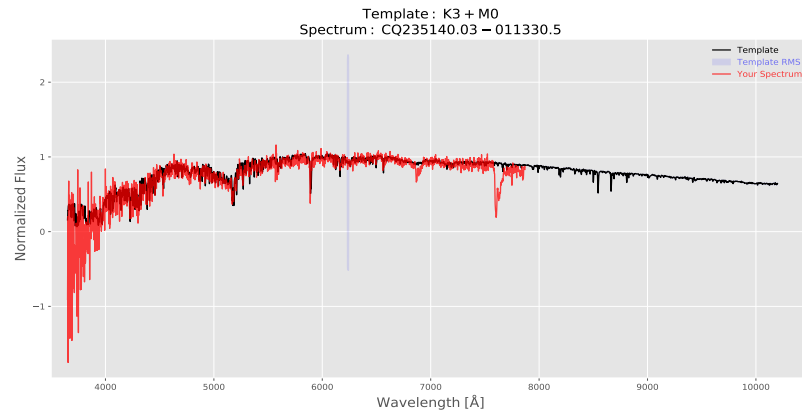


Figure 5.8: The PyHammer fitted spectrum of CQ 235140.03-011330.5, authenticating it to be binary stars, which consist of a K3 star and an M0 star.

CQ 235807.91-011943.3 ($z = 3.71$)

The Ly α forest is very manifest in our optical spectrum, suggesting that the redshift of this quasar is at least $z = 3$. We determine its redshift more precisely to be $z = 3.71$ by fitting the emission spire at the onset of the Ly α forest near 6000 Å with the Ly α line. Besides, the existence of a damped Ly α system at $z = 2.29$ along the line of sight from the object to us is hinted by the probable big trough at around 4000 Å. We obtain the amount of dust reddening to be $A_B = 0.2$, matching the template with the spectrum and photometry perfectly both in the blue and the red wavelengths. There isn't an absorption line associated with the C IV line, so we mark this quasar as a normal one, different from its 'STAR' tag in the SDSS database.

CQ 005406.43-100002.6 ($z = 2.38$)

Again, this is a very classic BAL quasar, with the apparent presence of broad absorption troughs blueward of emission lines. The redshift of this object is $z = 2.38$, by connecting the emission line at around 6500 Å with the C III] line. With an estimated dust extinction coefficient $A_B = 0.4$, we can fit the spectrum and photometry simultaneously with our template. It's a star in the SDSS server.

CQ 010002.00-030856.7 ($z = 1.24$)

This target has a very similar spectrum to that of CQ 003635.12-140917.41, while we can fit the spectrum and infrared photometry quite well with our template for this

object, with the supposed relatively large amount of dust extinction ($A_B = 1.1$). Identifying the emission line at about 6500 \AA as the Mg II, we can derive the redshift of this object to be $z = 1.24$. It's a normal quasar since no intrinsic broad absorption lines from the quasar itself exist in the spectrum. The type of it is the 'STAR' in the SDSS object explorer.

CQ 231904.59-073841.6 ($z = 2.08$)

With spotting the emission line at approximately 6000 \AA as the C III], we easily obtain the redshift of this quasar to be $z = 2.08$. Despite the relatively large noise in this spectrum, we can see the absorption troughs blueward of the C IV and C III], showing that this is a BAL quasar. After attempts to match the photometry with our template, we find out the dust extinction is close to $A_B = 1.1$, and get a nice match to the optical spectrum at the same time. The SDSS classifies it as a star.

CQ 234530.36-135743.3 ($z = 2.325$)

The spectrum of this object is a combination of spectra in three bands, from the UV to the near-infrared, with the optical spectra (in grism 4 and grism 19) obtained by us in the summer school and the infrared spectrum observed by my supervisor, Johan. Due to the bad quality of the two spectra in the optical, we can hardly determine what the redshift of this object is supposed to be, although there seems to be an emission line near 4000 \AA . Nevertheless, Johan got the chance to observe it with the instrument [EMIR](#) of the GTC in the near-infrared and we find the H α line successfully at the wavelength beyond $2 \mu\text{m}$, with the help of which we obtain its redshift to be $z = 2.325$. We also success in matching the entire spectrum with our template by assuming the degree of dust reddening to be $A_B = 0.85$. We think it's a BAL quasar due to the multiple big troughs near the high ionization lines after we have finished fitting the redshift. This object can't be found in the SDSS.

CQ 003634.82-081425.8 ($z = 1.788$)

We recognize the three emission lines close to each other starting from 4000 \AA as the Si IV, C IV, and C III] with increasing wavelengths respectively, deriving the redshift of this object to be $z = 1.788$. Although there seems to be an absorption line blueward of the Mg II, it's merely the A-band telluric line, plus the fact that there isn't any absorption feature of the high ionization lines. Thus, we flag it as a normal quasar, with

the estimated amount of dust extinction to be $A_B = 0.5$, though it's a star in the SDSS server.

CQ 005258.35-052240.2 ($z = 0.161$)

This is a nearby quasar with a low redshift at $z = 0.161$, based on the appearance of the $H\alpha$ line at around 7800 \AA , while it's diminished a bit by the coupled telluric line at the same wavelength. The emission from the [O III] is oddly high, indicating a much larger amount of oxygen near this quasar than in common cases. The flat photometry shows that it's greatly reddened by the interstellar dust, with an estimated amount being $A_B = 1.5$. It's a bit surprising for a quasar at the low redshift to have such a large amount of dust extinction. Because the high and low ionization lines are not included in this spectrum, we tentatively mark it as a normal quasar, while it's thought to be a galaxy by the SDSS.

CQ 021725.85-144057.31 ($z = 2.07$)

It's a little difficult to determine the redshift for this object at first because there is only one obvious emission line in the spectrum. However, when we fit the only broad emission feature at around 3900 \AA with the *Lyalpha* line, we happen to find that the other emission lines in the template match quite well with most of the spectral characteristics which look like P Cygni profiles in the observed spectrum, making this quasar to be a BAL quasar with very shallow high ionization emission lines as well as low ionization emission lines at redshift $z = 2.07$. This target is slightly reddened by the dust ($A_B = 0.4$), assuming which can help us to fit the entire continuum well. This object is not included in the SDSS catalog.

CQ 115341.57+060815.5 ($z = 0.425$)

This object and CQ 005258.35-052240.2 look alike, so we can easily obtain the redshift of it to be $z = 0.425$ in the same way, by identifying the protuberant emission line at about 9400 \AA as the $H\alpha$ line. The rest appearing at the same place as other emission spikes in the spectrum verify such redshift estimation. We set the dust extinction to $A_B = 2.0$, with fitting this low-redshift quasar with the template from [Selsing et al. \(2016\)](#) though, because it matches the entire continuum better than that from [Vanden Berk et al. \(2001\)](#). It may indicate that this quasar at the low redshift doesn't have the contamination from its host galaxy, which is not normal for low-redshift quasars, while it's heavily dust reddened, possibly showing a quenched galaxy as discussed in the note

of CQ 235544.91-192524.5. We categorize it to be a normal quasar provisional for no observation of the carbon and magnesium lines, while it's a star in the SDSS SkyServer.

CQ 121020.98+142958.5 ($z = 1.49?$)

We estimate the redshift of this object to be $z = 1.49$, but we don't think it's really solid, for no clear sign of the appearance of broad emission lines. However, we exclude the possibility for it to be a star since it can't be fitted with any given spectrum of different stars in the PyHammer. Besides, it actually looks very similar to the spectrum of CQ 010339.41-132238.91. Therefore, we preliminarily fit the potential emission line at 7000 \AA with the Mg II line. Moreover, it seems that there is a small bump at the wavelength of the C III] line. Assuming our estimation is correct, we label it to be a BAL quasar for the P Cygni profile of the C III] line, without any dust extinction according to the presented photometry, although it might have the unrevealed dust emission for the same reason discussed in the note of CQ 010339.41-132238.91. After all, the blue light of it is indeed absorbed. It's classified as a star by the SDSS. Besides, we think this target can be a weak line quasar as well.

CQ 124154.87+255632.5 ($z = 1.313$)

The spectrum is similar to that of CQ 003635.12-140917.41, with a much more significant C III] emission though. Thus, the redshift is determined to be $z = 1.313$ by identifying the Mg II line at around 6500 \AA . We flag it being a normal quasar, with an estimated amount of dust extinction to be $A_B = 1.0$, matching the complete continuum quite well, maybe with a little discrepancy in the blue end, as described in CQ 000404.29-135905.43. Its type is 'STAR' in the SDSS database.

CQ 130022.82+241136.1 ($z = 2.698$)

We notice the conspicuous sign of the Ly α forest in the blue, so we naturally tag the emission line at approximately 4600 \AA to be the Ly α line, deriving the redshift being $z = 2.698$, without any extinction ($A_B = 0$) according to the photometry. Other emission lines in the template also match the spires in the spectrum, substantiating our estimation. For the P Cygni configuration of the C IV line, we classify it as a BAL quasar, despite its SDSS flag being a star.

CQ 131117.99+314715.4 ($z = 2.172$)

Unfortunately, the infrared photometry for this object is not found. Therefore, we don't really fit the dust extinction parameter since we can't do it properly without the help of infrared photometry, as shown in many cases previously. As a result, this object is not included in the concluded color-color diagram Fig. 5.2 and its amount of dust extinction is also set to be $A_B = 0$. The emission features in this spectrum are also not so apparent, while we believe that the little crest at around 6000 \AA is attributed to C III] line, determining the redshift of this object to be $z = 2.172$. This assumption can be verified by the good match of other emission lines to the bumps or spikes in the observed spectrum. Due to the appearance of a broad absorption line blueward of the C IV, we categorize it being a BAL quasar, in contrast to its SDSS type as a star.

CQ 131919.56+115251.9 ($z = 2.51$)

This spectrum looks close to the last one, although with more obvious emission lines. By identifying the emission line at about 5400 \AA as the C IV line, we derive the redshift to be $z = 2.51$. For the relatively large noise in the spectrum, we don't think the little groove beside the C IV line is the absorption feature of it, while the deep trough blueward of the C III] line is the B-band telluric line. As a result, we tag this target to be a normal quasar and get its SDSS label to be a star.

CQ 235600.19-073716.0 ($z = 1.028?$)

This object has an extremely strange spectrum, and it's clearly not a star for the existence of emission lines. We find it hard to obtain the redshift of it for the abnormal boost of the flux near 4500 \AA . At first, we think it's a Ly α line, but there are no signs of Ly α forest beside it, making it exceptionally rare and unlikely. afterward, we fit it with the Mg II line, making the emission spire at about 3800 \AA seem to be the C III] line. Thus, we get the tentative redshift to be $z = 1.028$, and estimate the amount of dust extinction to be $A_B = 0.3$, based on the photometry at the longer wavelength. For the abnormal spectral features of this object, we mark it as a peculiar quasar, while it's shown as a star in the SDSS database.

CQ 235954.08-124150.58 ($z = 0.95?$)

This target has similar untypical spectral features to those of the last object. Thus, we provisional identify the same feature at around 5200 \AA as the Mg II line, supposing the

redshift to be $z = 0.95$. We don't find data on the photometry for this object, either. Thus, it's also not displayed in the color-color map Fig. 5.2. Likewise, we set the dust extinction at the B band A_B to be 0, for no supply from the infrared photometry. This object is not observed by the SDSS, while we label it to be a peculiar quasar.

PSS J0141+3334 ($z = 3.32$)

This quasar is one of the two detached BAL quasars in our observed candidates, with the other one to be CQ 010930.72-071931.1, while we have a much better fit to the optical spectrum of this object. It's a composite spectrum from the ones observed with grism 4, grism 19, and in the infrared. The details of redshift determination are discussed in Sect. 5.3, from which we calculate it to be $z = 3.32$. This object has a name different from others since we find it in the paper of Brunner et al. (2003), and we directly quote that name for consistency. It looks like a detached BAL quasar in the figure presented by Brunner et al. (2003), but it's not completely confirmed and has only been observed in a limited wavelength range. We are quite interested in such objects without apparent emission lines. Hence, we observed it again in a much wider wavelength range. However, for the lack of photometry in the J and K bands, unfortunately, we are unable to locate this target in the color-color plot Fig. 5.2. We measure the amount of dust reddening for it to be $A_B = 0.1$, according to its WISE colors. This target can't be found in the SDSS database.

5.3 Detached BAL Quasars

CQ 010930.72-071931.1 and PSS J0141+3334 are two objects in our observed samples that we are mostly interested in, due to their distinctive spectral characteristics. We first notice them because they look like GQ 1309+2904, which was found by Fynbo et al. (2020), as displayed in Fig. 5.9, showing extremely high-speed outflows (with the lowest velocity to be 20,000 km/s and can reach 13% of the light speed for high ionization absorption) containing highly ionized species while no apparent emission lines of them are found in the spectra if the redshift estimation is correct. According to the obvious separation between the absorption lines and the model-predicted emission lines of the corresponding species at the specific redshift, these quasars are called detached BAL quasars, for the velocity of the observed outflows not starting from 0 km/s.

Moreover, the most mysterious feature is the disappearance of high ionization emission lines, or there is also a possibility that they are blueshifted but still become much weaker than predicted. We find such missing high ionization emission lines very similar to what

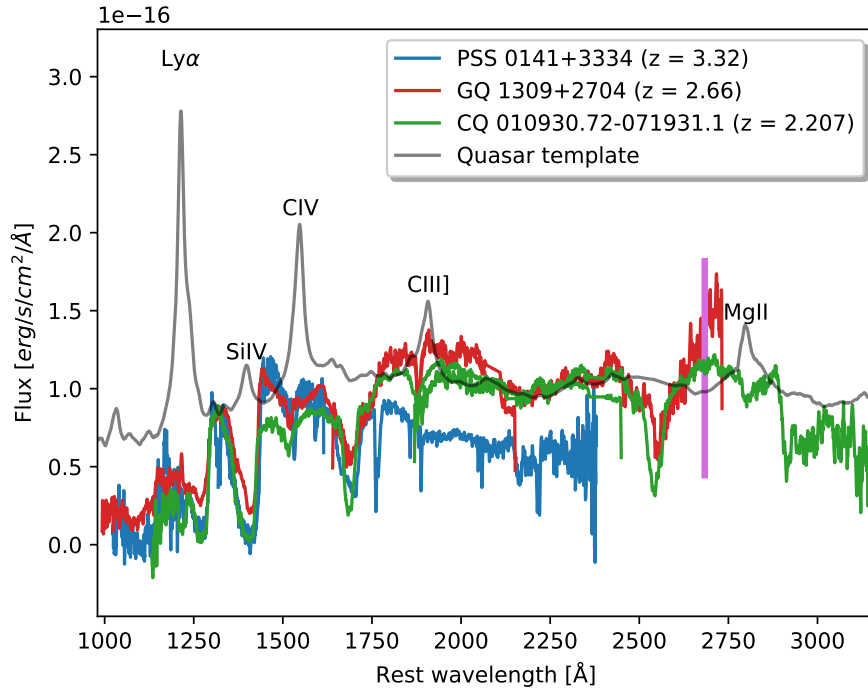


Figure 5.9: Comparison of spectra of three objects PSS J0141+3334 ($z = 3.32$), GQ 1309+2904 ($z = 2.66$), and CQ 010930.72-071931.1 ($z = 2.207$), with the spectrum GQ 1309+2904 received from Johan and the other two observed by us in the thesis. All the spectra are shifted to the rest frame according to their estimated redshifts determined using the method described in Sect. 5.3.1, normalized based on their blue parts, and overplotted with the quasar template reddened by $A_B = 0.5$ to fit the spectra in the UV, as estimated by Fynbo et al. (2020). We can easily tell that their spectra are astonishingly identical in their characteristics, implying they are experiencing a similar physical process. Although PSS J0141+3334 has a slightly different continuum to others, we think it's because it endures more extinction in the blue. The purple bar indicates the possibly blueshifted weak Mg II line of CQ 010930.72-071931.1.

appears in those weak line quasars ((Leighly et al. 2007; Diamond-Stanic et al. 2009; Hryniewicz et al. 2010)), but we think they are intrinsically different. In the weak lines quasars, the high ionization lines are generally weaker than normal quasars, but they are still there. Although Hryniewicz et al. 2010 found a special weak line quasar that doesn't have any high ionization emission line, there are no absorption lines of the highly ionized species as well, indicating the absence of highly ionized species near that quasar possibly.

However, for the detached BAL quasars, there are indeed highly ionized species in the outflows for the appearance of high ionization broad absorption lines. We propose a potential explanation of the disappearing high ionization emission lines in Sect. 5.3.2, which has something to do with the view angle. The detached BAL quasars can be good examples for unveiling the inner structure of the outflows around quasars and potential evidence of the disk wind model (Elitzur & Shlosman 2006), but all the statements should be based on the fact that we have determined their redshifts correctly. This is what we elaborate in Sect. 5.3.1, and we are pretty sure we have done the right things.

5.3.1 Quantitative redshift determination

Fynbo et al. (2020) is the first case to measure the systemic redshift of these detached BAL quasars according to the extended Ly α emission of GQ 1309+2904, which was inspired by the contradiction between the onset of the Lyman- α forest and the hypothetical Lyman- α emission.

The redshift measurement of GQ 1309+2904 is more or less verified by parts of the possible Mg II and H α lines observed in the spectrum given by Fynbo et al. (2020). However, it's not 100% credible because the possible Mg II and H α lines were not observed completely, which are located outside the observable wavelength range of the used telescopes. Besides, the expected Mg II line is not observed in the spectrum of CQ 010930.72-071931.1 very obviously, although we suspect that it can be blueshifted and obscured to be very weak, which is discussed in Sect. 5.3.2 while the existence of H α line in GQ 1309+2904 is very likely to be true. Unfortunately, the Mg II line in PSS J0141+3334 plus H α lines in CQ 010930.72-071931.1 and PSS J0141+3334 are unobservable with the ground-based telescopes as well, due to the observable wavelengths windows restricted by the atmosphere (Thorne et al. 1999). We may be able to observe them utilizing space telescopes, but it's hard to get access to them. Therefore, we will follow the same method as what has been used by Fynbo et al. (2020), investigating the onset of the Lyman- α forest, in a more quantitative way.

As what has been done in Fynbo et al. (2020), we can restrict the systemic redshift by checking the wavelength relationship between the Ly α forest and the Ly α crest. It's based on the fact that the Ly α forest lines are usually found blueward of the Ly α 's peak and it's easy to understand this feature because only the neutral gas between the clouds radiating the Ly α emission and us can act as the Ly α absorber, which is usually at lower redshift than the Ly α emitters. Nevertheless, the Ly α forest can sometimes be present at the red wings of Ly α spikes, as seen in Becker et al. (2004). It's simply because the Ly α emission lines can occasionally be blueshifted when the emitters happen to move towards us or they are just emitted by the outflows facing us, with a mean velocity shifts up to -1770 km/s (7 \AA shortwards of the Ly α line at 1215 \AA), where the negative sign refers to that the motion is towards us (Tytler & Fan 1992).

Despite the blueshifted Ly α emission line, the Ly α forest lines are very unlikely to have the rest wavelengths longer than 1222 \AA ($1215 + 7$), not to mention the possibility for them to be located outside the red wings of Ly α lines. This is the key to our quantitative method for estimating the systemic redshift of detached BAL quasars, which is to quantitatively distinguish the Ly α forest lines from the random noise from intervening

clouds in the spectra. This is a big improvement from the work of [Fynbo et al. \(2020\)](#), in which they just qualitatively said they found Ly α forest lines much redward of the Ly α line at their first assumed redshift $z = 2.41$, and ruled out this assumption to confirm the final estimation $z = 2.66$. By spotting Ly α forest lines quantitatively, we can make such exclusion much more trustworthy.

We take PSS J0141+3334 for an example to show how we derive the redshift of the detached BAL quasars quantitatively since it has been researched by [Brunner et al. \(2003\)](#) and they determined its redshift to be $z = 3.005$, while we found a larger redshift at $z = 3.32$. The comparison between two redshifts is given in Fig. 5.10.

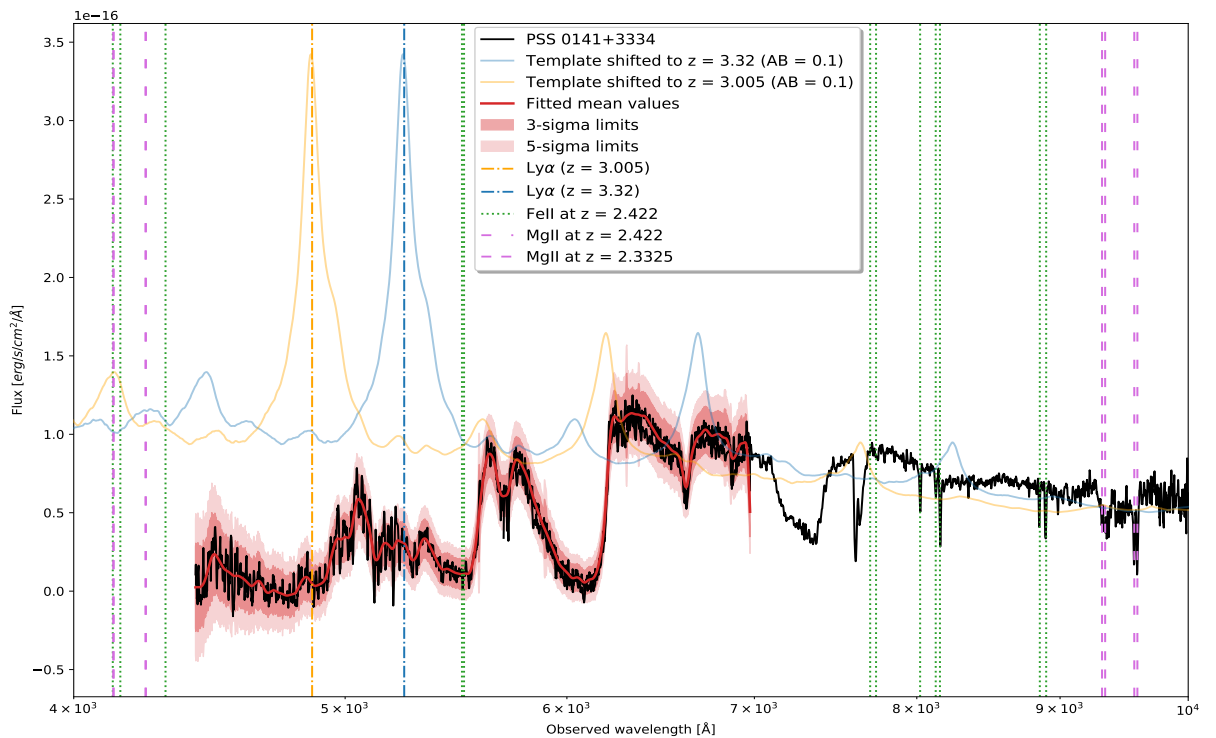


Figure 5.10: The spectra of PSS J0141+3334 in black observed with the NOT in grism 4 and grism 19, fitted with the quasar templates shifted to $z = 3.005$ (orange) and $z = 3.32$ (blue) with estimated amount of dust extinction $A_B = 0.1$. We plot the shaded 3-sigma and 5-sigma areas over the spectrum in red, with the sigma determined in the way demonstrated in Sect. 3.2.4. Besides, we overplot the intervening Fe II absorption at $z = 2.422$ and Mg II absorption at $z = 2.3325$, which are given by [Brunner et al. \(2003\)](#). In addition, we also find Mg II absorption at $z = 2.422$.

It's actually quite hard to tell which estimation is better at first glance and one may even think $z = 3.005$ is more plausible. After all, when there isn't any obvious emission line present in the spectra, people tend to derive the redshift intuitively by assuming that we can establish the systemic redshift based on the red edge of the BAL troughs ([Fynbo et al. 2020](#)) since it's generally the case of the P Cygni profile in the BAL quasars.

However, it's no longer valid for the detached BAL quasars, in the spectra of which the absorption lines are usually thought to be dissociated from the corresponding emission

lines due to their large blueshifts caused by the high-speed outflows. Thus, with the surprising similarity between the spectrum of PSS J0141+3334 and that of GQ 1309+2904 as one can easily find in Fig. 5.9, we assume PSS J0141+3334 is a detached BAL quasar as well, with the same outflow velocity as that of GQ 1309+2904, causing the C IV absorption line happens to overlap the Si IV spire and estimate the systemic redshift of PSS J0141+3334 to be $z = 3.32$.

Now we need to check which measurement is more credible, with the help of Ly α forest. If we find Ly α forest lines appearing redward of the peak of the Ly α line, we need to be cautious about the redshift estimation, though it may due to the blueshift of the Ly α line, while if Ly α forest lines have the wavelengths much longer than that of the Ly α spike, the redshift determination is much unlikely to be true. This is the case of the measurement ($z = 3.005$) by Brunner et al. (2003), where we find the Ly α forest lines present far after the Ly α crest, giving the solid evidence to exclude such measurement, as shown in Fig. 5.11.

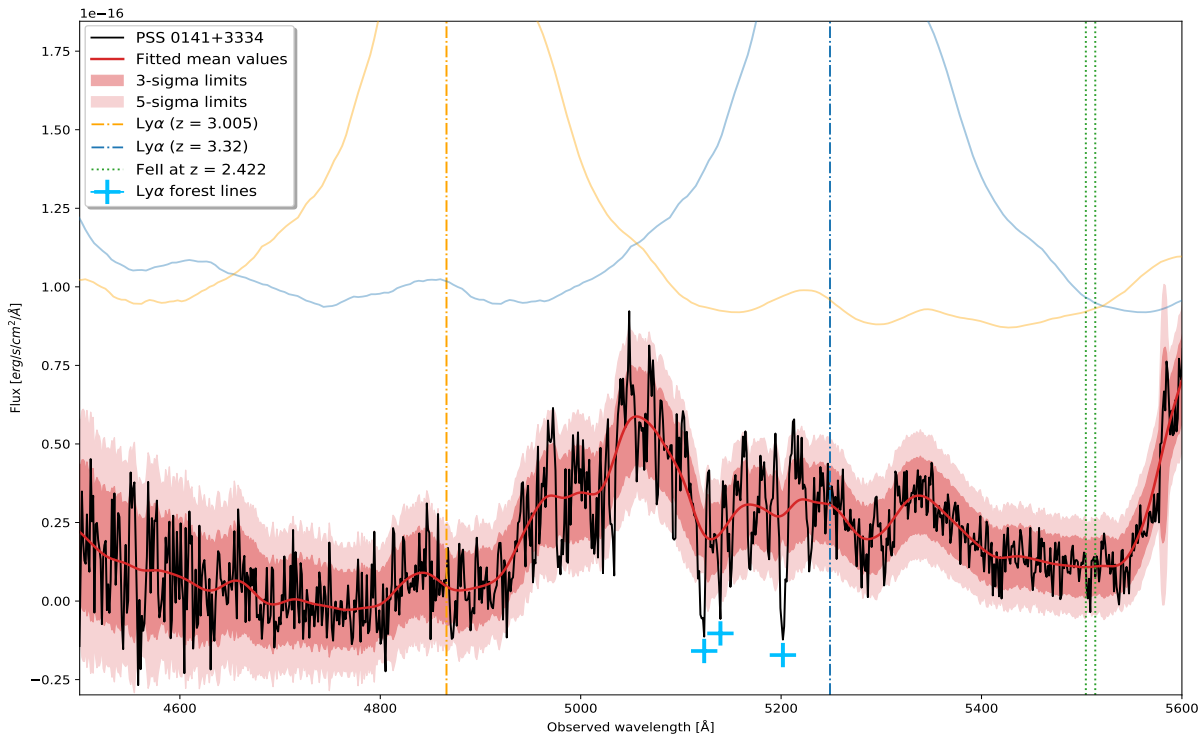


Figure 5.11: The zoomed-in spectrum of PSS J0141+3334 between 4500 Å to 5800 Å. We overplot the red-shaded 3-sigma and 5-sigma regions on the spectrum, to bring out the spectral features which are not produced by the noise. The intervening Fe II absorption at $z = 2.422$ is plotted in the green dotted line while other lines are not even included in this wavelength range. Thus, we mark the confirmed Ly α forest lines in blue crosses. One can easily see their appearance after the peak of Ly α emission shifted to $z = 3.005$ in orange and shortwards of the Ly α line at $z = 3.32$.

In Fig. 5.11, we display how we find the Ly α forest lines quantitatively, marked with blue crosses. It's based on a very simple principle but widely used in particle physics, which is the 5-sigma rule that only the result with the value 5 sigmas away from the

mean value has the possibility to be considered to be a discovery by particle physicists. It's because if only the random noise is included and considered in a physical process, 99.73% of the data points are believed to be located within a 3-sigma deviation from the mean value, while 99.99994% of the data points will be embraced by the mean value with a 5-sigma error tolerance. In other words, the outlier found outside the 3-sigma region is thought to be 0.27% likely to be produced by the statistical fluctuations while the likelihood of finding a noise-induced result 5-sigma apart from the mean value is merely 0.00006%, showing the result to be real, which means that it's very likely to be generated by other processes than the noise, for instance, a real physical process. Besides, 3-sigma results can be evidence for discovery, but they're not as convincing as 5-sigma observations.

This rule can also be utilized in our measurement. If we can find the spectral features which exceed the 5-sigma limit around the fitted mean values of the spectrum, we can make sure they're very possible to be created by absorption or emission. Therefore, we apply this 5-sigma principle to distinguish the Ly α forest lines from the random noise fluctuating the spectrum.

By overplotting the 5-sigma region on the spectrum, we easily find three conspicuous downwards outliers between 5100 Å and 5200 Å, which appear to be real absorption lines. After ruling out the possibility for them to be intervening absorption lines of other species like the discovered Fe II absorption at $z = 2.422$, we are pretty sure that the three lines marked with the blue cross are Ly α forest lines.

As a result, the $z = 3.005$ estimation is very implausible to be true, since the Ly α forest lines are located even beyond the red end of the hypothesis Ly α line. In addition, it makes our redshift measurement $z = 3.32$ more reliable because the Ly α forest lines are set blueward our estimated Ly α line. The discrepancy between the emission crest at 5050 Å and our estimated Ly α line at 5250 Å (assuming $z = 3.32$) can be interpreted as the Ly α emission from the outflows, with a velocity near 11000 km/s, much less than the lowest velocity of absorption outflows found in [Fynbo et al. \(2020\)](#) to be 20000 km/s. Such emission is possibly from the outflows much closer to the quasar core and accretion disk, which can make sense as demonstrated in Sect. 5.3.2.

We also implement such determination to the other two objects. However, their Ly α emission lines and hence the forest lines are not really located at the wavelengths where our facilities have the best performance, due to their relatively lower redshift (GQ 1309+2904 at $z = 2.66$ and CQ 010930.72-071931.1 at $z = 2.207$).

Indeed, we think the quantitative identification of Ly α forest lines is only able to set the

lower limit of the redshift, but it's very efficient and useful to rule out several redshift estimations. Besides, with the validation from the signs of existence of Mg II and H α lines at the predicted wavelengths in [Fynbo et al. \(2020\)](#), we think these measurements are quite dependable. In addition, even if the redshift is higher, indicating the outflows to be much stronger, it will make things more interesting.

5.3.2 Possible interpretation of the peculiar spectra features

In addition to the redshift determination, another aspect that we are the most fascinated by the detached BAL quasars is their peculiar spectral features. With our measurements of the redshifts, the three detached BAL quasars we find show surprisingly similar spectral energy distributions, as shown in [Fig. 5.9](#). After shifting them all to the rest frame, the absorption troughs look indistinguishable with similar widths, which indicates the outflows of them are also possibly identical, with alike velocity distribution. Moreover, the disappearing high ionization emission lines are the most astonishing and puzzling, with the fact that there are highly ionized species along the lines of sight producing broad absorption lines. Furthermore, there are implications for the existence of low ionization emission lines at the same time in the spectrum of GQ 1309+2904 from [Fynbo et al. \(2020\)](#), although the Mg II line isn't observed at the predicted wavelength in the spectrum of CQ 010930.72-071931.1. However, it can be slightly blueshifted and has a much lower intensity.

In a word, the high similarity of the spectra of the detached BAL quasars indicates that they must be caused by an identical process, because of which we can only see high ionization and low ionization absorbing outflows with very large ejection velocities (nearly 20,000 - 40,000 km/s), possible low ionization emission clouds with some ejection velocities (around 0 - 20,000 km/s from the potential weak Mg II line in CQ 010930.72-071931.1), and no or very weak blue-shifted high ionization emission clouds.

We were first inspired by [Fig. 8¹](#) of [Lamy & Hutsemékers \(2004\)](#), in which they showed a schematic illustration that the detached BAL quasars and BAL quasars are seen from different viewing angles through the disk wind. The P Cygni profiles (named after P Cygni, which spectrum shows special features that the emission lines are connected with corresponding blueshifted absorption lines) of normal BAL quasars are obtained when we observe the edge-on quasars since we can see the outflows near the disk in this scenario, which usually have lower velocities, enabling us to detect absorption at

¹Links to cited figures or equations may open the pertinent page via ADS (but macOS Preview may shunt to the start page).

all velocities. As for the detached BAL quasars, they are observed along less inclined lines of sight and we can just see the top parts of the disk wind, which makes us miss the low-speed components. Thus, the observed velocity difference of outflows between the detached BAL quasars and normal BAL quasars can be attributed to the orientations of quasars.

However, the absence of high ionization emission lines can't be explained by such a model. They discussed a two-component wind model with clumps of electrons in the polar regions of quasars which can scatter radiation from the central regions to explain the anti-correlation between the polarization degree (p , describing how severe the radiation is polarized) and the detachment index (DI, measuring the onset of the C IV trough; for more details see [Lamy & Hutsemékers \(2004\)](#)). They claimed that the high polarization degree of P Cygni BAL quasars with low detachment index shows that they endure more absorption than the detached BAL quasars. Nonetheless, if we can detect the scattered radiation from regions near the black hole by the electron clouds in the polar region of the detached BAL quasars, we should definitely see the broad emission lines of highly ionized species. Besides, their data showing the anti-correlation are not really convincing because there are just two samples with high DI and low p , plus four objects with low DI and high p , which don't have good statistics. Therefore, we don't really trust their two-component wind model with scattering electron clouds but the suggestion for different view angles of the detached BAL quasars and P Cygni BAL quasars is truly solid.

The next question we are trying to answer is then why the high ionization emission lines disappear when we observe the BAL quasars from different angles, while we can still see the low ionization emission lines (possibly). The very first guess would naturally be that there are no highly ionized species in the detached BAL quasars, which is easily excluded since we indeed detect the high ionization absorption lines in the detached BAL quasars. As a result, there must be some distinction between clouds that emit or absorb high/low ionization lines.

The inner structure of the outflows illustrated by [Elvis \(2000\)](#) in [Fig. 5](#) enlightened us. [Elvis \(2000\)](#) suggested that the broad-line regions can be located inside the disk wind, while the different distances from the clouds to the central continuum source generate their different roles in the spectra. The closer the clouds are to the central regions, the hotter they are and hence higher ionized, which is also shown by [Emmering et al. \(1992\)](#). Besides, the further they are from the center, the more likely they will absorb the radiation. In short, the tail of the outflow (closer to the disk) emits the radiation, while the head of the outflow absorbs it. This can be understood intuitively since the

clouds located in outer space are colder and they tend to stay at a lower energy level. In addition, the low ionization clouds are set at larger radii because the full ionizing continuum from the X-ray corona surrounding the black hole is partly shielded by the inner high ionization broad emission line regions. This assumption is very instructive for the separation of high/low ionization broad emission/absorption line (BEL/BAL) regions.

Unfortunately, this model still can't explain the disappearance of high ionization emission lines since no matter how we change the view angles (while we need to keep it near the direction of the outflows), there are no reasons for the high ionization BEL to vanish in our field of view. This problem isn't solved until we see the dusty wind model by [Elitzur & Shlosman \(2006\)](#).

[Elitzur & Shlosman \(2006\)](#) suggested an innovative model that denies the existence of the dusty torus encircling the black hole and the accretion disk in the unified model of AGN, which has been discussed in Sect. 1.1.4. They argued that the seen torus is just a region in the disk wind, appearing to generate the observed toroidal obscuration since the disk wind is also thought to be circular. They made such an assumption because the hydrostatic doughnut-like dusty torus can't account for the vertical motions that help to keep the clouds sustaining their heights when their radii increase (the height and radius of the torus are considered to follow the rule $H/R \sim 1$, for more details, see [Schmitt et al. 2001](#) and [Davies et al. 2006](#)). The torus clouds in the disk wind are distributed from the dust sublimation radius R_s to 5 - 10 R_s . The dusty wind model is further substantiated by [Hönig & Kishimoto \(2017\)](#). Besides, according to the difference between Type 1 quasars and Type 2 quasars and the origin of it mentioned in Sect. 1.1.5, the torus is capable of removing broad emission lines, certainly including broad high ionization emission lines, from the spectra.

Therefore, we come up with a new detailed dusty wind model showing the inner structure of the outflows, which is able to explain all the peculiar features found in the spectra of the detached quasars, displayed in Fig. 5.12.

The combined effect of viewing angles and the outflows' specific inner structure creates the peculiar spectral features of the detached BAL quasars. In the thick disk wind, the radiation with lower energy can penetrate further while the full ionizing continuum tends to be absorbed completely by the clouds at inner radii, plus the accretion disk generally becomes cooler at larger radii, so the clouds emit high/low ionization lines are supposed to be closer to the center and the high ionization BEL regions are the innermost ([Elvis 2000](#)). However, such a rule can not only apply to clouds along the

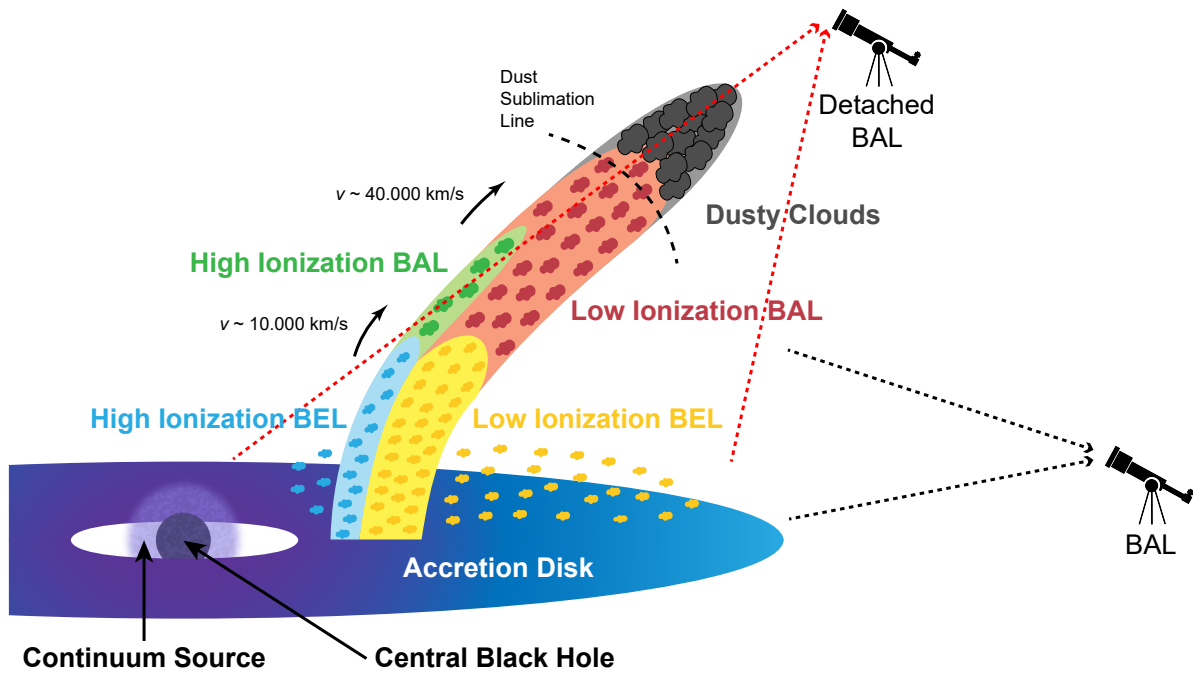


Figure 5.12: A schematic illustration for the new dusty wind model demonstrating the inner structure of the disk wind. We propose that the high/low ionization broad emission/absorption lines (BEL/BAL) are located in the different regions in the outflows, attributed to their different distances to the central continuum source and hence the optical depth is different. High ionization BEL regions are colored in blue, high ionization BAL regions are colored in green, low ionization BEL regions are plotted in yellow, and low ionization BAL regions are plotted in red, with the outermost regions containing dusty clouds, colored in grey beyond the dust sublimation line. The accretion disk is schemed from the innermost regions to the outer edge of the disk with color gradients from purple to blue, based on the fact that the inner disk is much hotter while the outer part is cooler. We set the inclination of the outflow being nearly 45 degrees to the disk plane according to the rule that the height and radius of the torus are comparable ($H/R \sim 1$ from [Schmitt et al. 2001](#)). This magnificent illustration is created with the greatest help of my wonderful friend Shangcheng Yan.

disk plane, where the gas clumps are very thick, but it's also applicable to the clouds moving along with the outflows.

When the outflows are ejected outwards, the clouds in the outflows are thought to be comoving with them, Besides, the clouds are generally considered to be diluted by the increasing sizes at the same time due to thermal expansion. However, [Elitzur & Shlosman \(2006\)](#) argued that magnetic effects can always confine the thermal expansion, keeping clouds small and dense. Thus, the outflows ought to be thick as well in their moving direction, generating a shielding effect to high energy radiations, but we have to clarify that the clouds along the outflows are not as thick as those closer to the disk plane. Such density difference makes the absorption coefficients dissimilar in different directions, causing clouds with lower density to absorb less radiation which can produce highly ionized species.

As a result, the high ionization BEL regions degenerate to low ionization BEL regions (since clouds have higher density near the disk plane) or high ionization BAL regions

(because the clouds moving along with the outflows are in lower density) at larger spherical radii. Furthermore, as the radiation penetrates deeper into the outflows, it becomes weaker and weaker and can only energize atoms to low ionization states. In addition, the clouds' density keeps dropping with increasing radii. Therefore, the clouds there are supposed to be at the low ionization ground states, mainly giving rise to low ionization broad absorption lines.

Moreover, the gas clouds can be cooled down enough when the outflows pass through the dust sublimation line and form the dusty clouds. According to what has been found by [He et al. \(2022\)](#), the acceleration of outflows can happen at a scale of 10 parsecs, so the dusty clouds should still be highly collimated and constrained inside the shock wave. Such confinement can keep the density of dusty clouds at a relatively higher level, enabling them to absorb high/low ionization emission lines. We also speculate that a few low ionization BAL clouds with the highest velocity can penetrate further beyond the dust sublimation line and keep in the gas phase. Furthermore, the BAL regions have larger velocities than the BEL regions in general, as predicted by the model, and can be verified by the observations very well. As the outflows keep accelerating to the space very far away, the BAL clouds situated in the outer regions are certainly faster.

However, low ionization radiation is supposed to be obscured less by the dust compared to the high ionization counterpart, due to the fact that low ionization emissions generally have less energy and hereby longer wavelength. Besides, it's possible for low ionization BEL regions to exist in the outer disk since the outflows shroud the outer disk from the full ionizing continuum while the cooler outer disk is only capable of producing low ionized species. Therefore, the disappearance of high ionization emission lines and the potential existence of low ionization emission lines in the spectra can be expected.

We validate the physical possibility of the existence of the newly-proposed dusty wind model with inner components, which can result in the special features in the spectra we observe in the detached BAL quasars.

By constraining the quasars within a certain range of orientation, based on the theory of [Lamy & Hutsemékers \(2004\)](#), we propose that the detached BAL quasars are found when we happen to observe the quasars along the moving direction of their outflows. Due to the special inner structure of the outflow as shown in [Fig. 5.12](#), the dusty clouds are set at the front of the outflow, absorbing the radiation from the interior, especially all of the high ionization emissions carrying greater energy and lots of the low ionization emissions. Despite the dust attenuation, a few low ionization emissions can still escape

from the dusty clouds due to their lower wavelengths and be detected by our telescopes. Besides, there may be a few low ionization BEL residing in the outer disk regions since the disk at larger radii is still hot but not as hot as that near the central engine which can generate a full ionizing continuum.

As a consequence, we don't see any high ionization emission line at the wavelength predicted by the template at the estimated redshift in the spectra, but we can indeed see the low ionization emissions at the expected wavelengths (at least the existence of the prominent $H\alpha$ line is somewhat convincing in [Fynbo et al. 2020](#)), since the low ionization BEL clouds in the outer disk that are not covered by the outflows entirely and some low ionization emissions generated at the bottom of the outflows can also escape from the depletion caused by the dusty clouds. These low ionization BEL clouds are not moving towards us, so they can account for the low ionization emission lines at the systemic redshift.

In addition, there also seem to be some blueshifted low ionization emission lines in the spectra, such as the possible blueshifted Mg II line in the spectrum of CQ 010930.72-071931.1, which can be attributed to those low ionization BEL clouds at larger heights moving towards us. Such emission lines can partly penetrate the dusty torus in the disk wind and reach us due to their relatively low energy compared to the high ionization emissions.

Furthermore, as shown by the red sightlines in [Fig. 5.12](#), we can detect the entire velocity range of broad absorption line regions since we are observing against their movement direction. The BAL clouds are not generated close to the disk, and they are rather created at higher latitudes when the outflows have been accelerated for a while by the radiation pressure. Thus, the broad absorption lines we see in the spectra are well detached from the expected emission lines as their origins, the BAL clouds, have velocities much larger than zero.

The spectral features of normal BAL quasars can also be interpreted by this model. When we observe the edge-on quasars, our sightlines are not blocked by the dusty clouds in the head of the outflows (the part away from the quasars). As a result, we can see the high/low ionization BEL/BAL completely, while some lines of sight that are perpendicular to the outflows can produce the broad absorption lines with zero velocities, creating the P Cygni profiles in the BAL quasars.

We admit that the new dusty wind model containing the inner structure of the outflows is very tentative, merely proposed according to the spectral features of the detached BAL quasars and P Cygni BAL quasars. Besides, the transition between different regions with

different ionization states or electronic states may be continuous, but we just display them clearly separated in Fig. 5.12 for a more conspicuous illustration. In addition, the nature of the similar velocity distributions of the outflows is not well understood. It's very unlikely that we happened to observe three detached BAL quasars with the same properties such as the central black hole mass or the accretion rate. Otherwise, it may imply they are in the same evolution phase, which may constrain the central black holes to a certain stage and make the quasars appear as the detached BAL quasars.

In the future, we will try to obtain the spectra of these three detached BAL quasars including the possible Mg II and H α lines within the wavelength range, to corroborate our estimation of their redshifts and further our proposed detailed model of the dusty disk wind. In addition, we can estimate the mass of the central black hole (Wang et al. 2009) plus its corresponding bolometric luminosity and hereby Eddington ratio (Netzer & Trakhtenbrot 2014) by getting the spectra of MgII lines, with the help of their full width at half maximum (FWHM).

Chapter 6

Conclusions and Outlook

In this work, we selected 50 quasar candidates with abnormal colors, with most of them (30 out of 50) being red quasar candidates. To find out why they are dissociated from normal stellar locus and quasar clump in the color-color diagram, we observed them with the Nordic Optical Telescope and the Gran Telescopio Canarias. The details of observations in the Nordic Optical Telescope are presented in Chapter 2. As for obtained spectra, we elaborate how we process, analyze, and classify them in Chapter 3, Chapter 4, and Chapter 5 respectively.

We find 23 normal quasars, 18 BAL quasars, 2 detached BAL quasars, 2 peculiar quasars, and 5 stars in total. With the fact that 45 out of 50 candidates in peculiar colors are indeed quasars, not to mention that we picked 4 candidates which are very close to the stellar locus, the incompleteness of the quasar population selected based on commonly used color criteria is unveiled conspicuously.

Moreover, 16 BAL quasars are discovered in 30 randomly selected red quasar candidates, while we are unable to attain the photometry of 3 BAL quasars. Such a surprisingly high proportion of BAL quasars in the red quasars indicates that we may overlook a large amount of BAL quasars, especially those appearing much redder, making their widely agreed population of 10% of the entire quasar group be too small since the majority of current unearthed quasars are blue quasars. The large number of BAL quasars among red quasars can be interpreted as their possibly more dusty nature or it's simply because we happen to observe them along the line of sight not only with more dense gas clouds but also containing more dust.

Furthermore, we notice two anomalous detached BAL quasars with extremely high-speed outflows among our observed red samples, in which the high ionization outflows

have the lowest velocity to be 20,000 km/s and can be accelerated to 13% of the light speed. What's more peculiar is that there isn't any high ionization emission line in the spectra. We proposed a quantitative way to determine their redshifts without the help of any emission lines, based on the onset of the Ly α forest. Lastly, a potential interpretation of their strange spectral features is suggested, showing restricted viewing angles and the inner structure of outflows, which can support the dusty disk wind model. Again, we can neglect special quasars which may help to enrich our knowledge of quasars if we persist in selecting quasars based on their colors.

The color criteria have intrinsic shortcomings caused by the inherent inaccuracy of photometry because it integrates the radiation in a relatively large wavelength range and omits detailed spectral features. Besides, the finite samples used to generate color criteria can be biased either by being not statistically representative or by unknowns, engendering the created selection rules biased to certain groups. In addition, the selection rules tend to sacrifice completeness for high selection efficiency. It's very likely that the more precise the criteria are, the more patchy results they will produce.

Therefore, it's time to step forward for a complete census of quasars, with the upcoming 4-metre Multi-Object Spectroscopic Telescope ([4MOST](#)) operated by ESO in two years (hopefully). The powerful facility enables us to acquire spectra of around 2400 objects simultaneously, which lowers the cost of getting spectra very significantly. As a result, it makes us capable of selecting quasars out of stars based on their spectra, not their colors, which is much more accurate. By obtaining the spectra of all the point sources with zero proper motions and parallaxes in an acceptable time frame, we can get a complete census of quasars for the first time (of course within the observable sky of the 4MOST), and hence attain a more thorough view of the universe. We are really looking forward to it.

Bibliography

- Allen, J. T., Hewett, P. C., Maddox, N., Richards, G. T., & Belokurov, V. 2011, MNRAS, 410, 860, doi: [10.1111/j.1365-2966.2010.17489.x](https://doi.org/10.1111/j.1365-2966.2010.17489.x)
- Antonucci, R. R. J., & Miller, J. S. 1985, ApJ, 297, 621, doi: [10.1086/163559](https://doi.org/10.1086/163559)
- Barmby, P., Alonso-Herrero, A., Donley, J. L., et al. 2006, ApJ, 642, 126, doi: [10.1086/500823](https://doi.org/10.1086/500823)
- Becker, G. D., Sargent, W. L. W., & Rauch, M. 2004, ApJ, 613, 61, doi: [10.1086/422870](https://doi.org/10.1086/422870)
- Becker, R. H., Fan, X., White, R. L., et al. 2001, AJ, 122, 2850, doi: [10.1086/324231](https://doi.org/10.1086/324231)
- Beckmann, V., & Shrader, C. R. 2012, Active Galactic Nuclei
- Bell, M. B., & Comeau, S. P. 2010, Ap&SS, 326, 11, doi: [10.1007/s10509-009-0232-2](https://doi.org/10.1007/s10509-009-0232-2)
- Bessell, M. S. 1990, PASP, 102, 1181, doi: [10.1086/132749](https://doi.org/10.1086/132749)
- Blanton, M. R., Bershad, M. A., Abolfathi, B., et al. 2017, AJ, 154, 28, doi: [10.3847/1538-3881/aa7567](https://doi.org/10.3847/1538-3881/aa7567)
- Bolton, J. G. 1948, Nature, 162, 141, doi: [10.1038/162141a0](https://doi.org/10.1038/162141a0)
- Bongiorno, A., Zamorani, G., Gavignaud, I., et al. 2007, A&A, 472, 443, doi: [10.1051/0004-6361:20077611](https://doi.org/10.1051/0004-6361:20077611)
- Boroson, T. A., & Green, R. F. 1992, ApJS, 80, 109, doi: [10.1086/191661](https://doi.org/10.1086/191661)
- Boroson, T. A., & Oke, J. B. 1982, Nature, 296, 397, doi: [10.1038/296397a0](https://doi.org/10.1038/296397a0)
- Bovy, J., Hennawi, J. F., Hogg, D. W., et al. 2011, ApJ, 729, 141, doi: [10.1088/0004-637X/729/2/141](https://doi.org/10.1088/0004-637X/729/2/141)
- Brotherton, M. S., Tran, H. D., Becker, R. H., et al. 2001, ApJ, 546, 775, doi: [10.1086/318309](https://doi.org/10.1086/318309)
- Brunner, R. J., Hall, P. B., Djorgovski, S. G., et al. 2003, AJ, 126, 53, doi: [10.1086/375763](https://doi.org/10.1086/375763)
- Brusa, M., Fiore, F., Santini, P., et al. 2009, A&A, 507, 1277, doi: [10.1051/0004-6361/200912261](https://doi.org/10.1051/0004-6361/200912261)
- Buser, R., & Kurucz, R. L. 1992, A&A, 264, 557
- Cardelli, J. A., Clayton, G. C., & Mathis, J. S. 1989, ApJ, 345, 245, doi: [10.1086/167900](https://doi.org/10.1086/167900)

- Cherchneff, I. 2010, in *Astronomical Society of the Pacific Conference Series*, Vol. 425, *Hot and Cool: Bridging Gaps in Massive Star Evolution*, ed. C. Leitherer, P. D. Bennett, P. W. Morris, & J. T. Van Loon, 237. <https://arxiv.org/abs/0909.0164>
- Chiu, H.-Y. 1964, *Physics Today*, 17, 21, doi: [10.1063/1.3051610](https://doi.org/10.1063/1.3051610)
- Christensen, L. B., Vestergaard, M., & Christa, G. 2019, *Course literature of Astronomical Data Processing in University of Copenhagen*
- Clowes, R. 1981, *MNRAS*, 197, 731, doi: [10.1093/mnras/197.3.731](https://doi.org/10.1093/mnras/197.3.731)
- Crenshaw, D. M., Kraemer, S. B., Bruhweiler, F. C., & Ruiz, J. R. 2001, *ApJ*, 555, 633, doi: [10.1086/321522](https://doi.org/10.1086/321522)
- Crenshaw, D. M., Kraemer, S. B., Turner, T. J., et al. 2002, *ApJ*, 566, 187, doi: [10.1086/338058](https://doi.org/10.1086/338058)
- Cutri, R. M., Wright, E. L., Conrow, T., et al. 2013, *Explanatory Supplement to the AllWISE Data Release Products*
- Czerny, B., Li, J., Loska, Z., & Szczerba, R. 2004, *MNRAS*, 348, L54, doi: [10.1111/j.1365-2966.2004.07590.x](https://doi.org/10.1111/j.1365-2966.2004.07590.x)
- Davies, R. I., Thomas, J., Genzel, R., et al. 2006, *ApJ*, 646, 754, doi: [10.1086/504963](https://doi.org/10.1086/504963)
- Diamond-Stanic, A. M., Fan, X., Brandt, W. N., et al. 2009, *ApJ*, 699, 782, doi: [10.1088/0004-637X/699/1/782](https://doi.org/10.1088/0004-637X/699/1/782)
- Donley, J. L., Koekemoer, A. M., Brusa, M., et al. 2012, *ApJ*, 748, 142, doi: [10.1088/0004-637X/748/2/142](https://doi.org/10.1088/0004-637X/748/2/142)
- Draine, B. T. 2011, *Physics of the Interstellar and Intergalactic Medium*
- Draine, B. T., & Li, A. 2007, *ApJ*, 657, 810, doi: [10.1086/511055](https://doi.org/10.1086/511055)
- Eilers, A.-C., Davies, F. B., Hennawi, J. F., et al. 2017, *ApJ*, 840, 24, doi: [10.3847/1538-4357/aa6c60](https://doi.org/10.3847/1538-4357/aa6c60)
- Elitzur, M., & Shlosman, I. 2006, *ApJ*, 648, L101, doi: [10.1086/508158](https://doi.org/10.1086/508158)
- Elvis, M. 2000, *ApJ*, 545, 63, doi: [10.1086/317778](https://doi.org/10.1086/317778)
- Emerson, D. 1999, *Interpreting Astronomical Spectra*
- Emmering, R. T., Blandford, R. D., & Shlosman, I. 1992, *ApJ*, 385, 460, doi: [10.1086/170955](https://doi.org/10.1086/170955)
- Fan, X. 1999, *AJ*, 117, 2528, doi: [10.1086/300848](https://doi.org/10.1086/300848)
- Fitzpatrick, E. L. 1985, *ApJ*, 299, 219, doi: [10.1086/163694](https://doi.org/10.1086/163694)
- Florentin-Nielsen, R., Andersen, M. J., & Nielsen, S. P. 1995, in *New Developments in Array Technology and Applications*, ed. A. G. D. Philip, K. Janes, & A. R. Upgren, Vol. 167, 207
- Francis, P. J., Hewett, P. C., Foltz, C. B., et al. 1991, *ApJ*, 373, 465, doi: [10.1086/170066](https://doi.org/10.1086/170066)

- Fynbo, J. P. U., Krogager, J. K., Venemans, B., et al. 2013, *ApJS*, 204, 6, doi: [10.1088/0067-0049/204/1/6](https://doi.org/10.1088/0067-0049/204/1/6)
- Fynbo, J. P. U., Krühler, T., Leighly, K., et al. 2014, *A&A*, 572, A12, doi: [10.1051/0004-6361/201424726](https://doi.org/10.1051/0004-6361/201424726)
- Fynbo, J. P. U., Møller, P., Heintz, K. E., et al. 2020, *A&A*, 634, A111, doi: [10.1051/0004-6361/201936957](https://doi.org/10.1051/0004-6361/201936957)
- Gavignaud, I., Bongiorno, A., Paltani, S., et al. 2006, *A&A*, 457, 79, doi: [10.1051/0004-6361:20065376](https://doi.org/10.1051/0004-6361:20065376)
- Gibson, R. R., Jiang, L., Brandt, W. N., et al. 2009, *ApJ*, 692, 758, doi: [10.1088/0004-637X/692/1/758](https://doi.org/10.1088/0004-637X/692/1/758)
- Gilliland, R. L. 1992, in *Astronomical Society of the Pacific Conference Series*, Vol. 23, *Astronomical CCD Observing and Reduction Techniques*, ed. S. B. Howell, 68
- Glikman, E., Helfand, D. J., & White, R. L. 2006, *ApJ*, 640, 579, doi: [10.1086/500098](https://doi.org/10.1086/500098)
- Gordon, K. D., & Clayton, G. C. 1998, *ApJ*, 500, 816, doi: [10.1086/305774](https://doi.org/10.1086/305774)
- Gordon, K. D., Clayton, G. C., Misselt, K. A., Landolt, A. U., & Wolff, M. J. 2003, *ApJ*, 594, 279, doi: [10.1086/376774](https://doi.org/10.1086/376774)
- Greenstein, J. L., & Matthews, T. A. 1963, *Nature*, 197, 1041, doi: [10.1038/1971041a0](https://doi.org/10.1038/1971041a0)
- Greenstein, J. L., & Schmidt, M. 1964, *ApJ*, 140, 1, doi: [10.1086/147889](https://doi.org/10.1086/147889)
- Gunn, J. E., & Peterson, B. A. 1965, *ApJ*, 142, 1633, doi: [10.1086/148444](https://doi.org/10.1086/148444)
- Hall, P. B., Anderson, S. F., Strauss, M. A., et al. 2002, *ApJS*, 141, 267, doi: [10.1086/340546](https://doi.org/10.1086/340546)
- Hazard, C., Mackey, M. B., & Shimmins, A. J. 1963, *Nature*, 197, 1037, doi: [10.1038/1971037a0](https://doi.org/10.1038/1971037a0)
- He, Z., Liu, G., Wang, T., et al. 2022, *Science Advances*, 8, eabk3291, doi: [10.1126/sciadv.abk3291](https://doi.org/10.1126/sciadv.abk3291)
- Heintz, K. E., Fynbo, J. P. U., & Høg, E. 2015, *A&A*, 578, A91, doi: [10.1051/0004-6361/201526038](https://doi.org/10.1051/0004-6361/201526038)
- Heintz, K. E., Fynbo, J. P. U., Høg, E., et al. 2018, *A&A*, 615, L8, doi: [10.1051/0004-6361/201833396](https://doi.org/10.1051/0004-6361/201833396)
- Heintz, K. E., Fynbo, J. P. U., Møller, P., et al. 2016, *A&A*, 595, A13, doi: [10.1051/0004-6361/201628836](https://doi.org/10.1051/0004-6361/201628836)
- Heintz, K. E., Fynbo, J. P. U., Jakobsson, P., et al. 2017, *A&A*, 601, A83, doi: [10.1051/0004-6361/201730702](https://doi.org/10.1051/0004-6361/201730702)
- Heintz, K. E., Fynbo, J. P. U., Geier, S. J., et al. 2020, *A&A*, 644, A17, doi: [10.1051/0004-6361/202039262](https://doi.org/10.1051/0004-6361/202039262)
- Hönig, S. F., & Kishimoto, M. 2017, *ApJ*, 838, L20, doi: [10.3847/2041-8213/aa6838](https://doi.org/10.3847/2041-8213/aa6838)
- Hopkins, P. F., Strauss, M. A., Hall, P. B., et al. 2004, *AJ*, 128, 1112, doi: [10.1086/423291](https://doi.org/10.1086/423291)
- Howell, S. B. 2006, *Handbook of CCD Astronomy*, Vol. 5
- Hryniewicz, K., Czerny, B., Nikolajuk, M., & Kuraszkiewicz, J. 2010, *MNRAS*, 404, 2028, doi: [10.1111/j.1365-2966.2010.16418.x](https://doi.org/10.1111/j.1365-2966.2010.16418.x)

- Jakobsen, P. 2013, *An Astronomical Introduction to Poisson Statistics*
- Janesick, J. R., Elliott, T., Collins, S., Blouke, M. M., & Freeman, J. 1987, *Optical Engineering*, 26, 692, doi: [10.1117/12.7974139](https://doi.org/10.1117/12.7974139)
- Jansky, K. G. 1933, *Nature*, 132, 66, doi: [10.1038/132066a0](https://doi.org/10.1038/132066a0)
- Johnson, H. L., & Morgan, W. W. 1953, *ApJ*, 117, 313, doi: [10.1086/145697](https://doi.org/10.1086/145697)
- Kirkpatrick, J. A., Schlegel, D. J., Ross, N. P., et al. 2011, *ApJ*, 743, 125, doi: [10.1088/0004-637X/743/2/125](https://doi.org/10.1088/0004-637X/743/2/125)
- Krawczyk, C. M., Richards, G. T., Gallagher, S. C., et al. 2015, *AJ*, 149, 203, doi: [10.1088/0004-6256/149/6/203](https://doi.org/10.1088/0004-6256/149/6/203)
- Krogager, J.-K., Fynbo, J. P. U., Møller, P., et al. 2019, *MNRAS*, 486, 4377, doi: [10.1093/mnras/stz1120](https://doi.org/10.1093/mnras/stz1120)
- Krogager, J. K., Geier, S., Fynbo, J. P. U., et al. 2015, *ApJS*, 217, 5, doi: [10.1088/0067-0049/217/1/5](https://doi.org/10.1088/0067-0049/217/1/5)
- Kurucz, R. L. 1979, *ApJS*, 40, 1, doi: [10.1086/190589](https://doi.org/10.1086/190589)
- Lambourne, R. J. A. 2010, *Relativity, Gravitation and Cosmology*
- Lamy, H., & Hutsemékers, D. 2004, *A&A*, 427, 107, doi: [10.1051/0004-6361:20041066](https://doi.org/10.1051/0004-6361:20041066)
- Lawrence, A., Warren, S. J., Almaini, O., et al. 2007, *MNRAS*, 379, 1599, doi: [10.1111/j.1365-2966.2007.12040.x](https://doi.org/10.1111/j.1365-2966.2007.12040.x)
- Leighly, K. M., Halpern, J. P., Jenkins, E. B., & Casebeer, D. 2007, *ApJS*, 173, 1, doi: [10.1086/519768](https://doi.org/10.1086/519768)
- Leighly, K. M., Terndrup, D. M., Gallagher, S. C., & Lucy, A. B. 2016, *ApJ*, 829, 4, doi: [10.3847/0004-637X/829/1/4](https://doi.org/10.3847/0004-637X/829/1/4)
- Low, J., & Kleinmann, D. E. 1968, *AJ*, 73, 868, doi: [10.1086/110722](https://doi.org/10.1086/110722)
- Lu, L., Sargent, W. L. W., Barlow, T. A., Churchill, C. W., & Vogt, S. S. 1996, *ApJS*, 107, 475, doi: [10.1086/192373](https://doi.org/10.1086/192373)
- Mannucci, F., Cresci, G., Maiolino, R., Marconi, A., & Gnerucci, A. 2010, *MNRAS*, 408, 2115, doi: [10.1111/j.1365-2966.2010.17291.x](https://doi.org/10.1111/j.1365-2966.2010.17291.x)
- Massa, D., Savage, B. D., & Fitzpatrick, E. L. 1983, *ApJ*, 266, 662, doi: [10.1086/160813](https://doi.org/10.1086/160813)
- Mathis, J. S., Ruml, W., & Nordsieck, K. H. 1977, *ApJ*, 217, 425, doi: [10.1086/155591](https://doi.org/10.1086/155591)
- Matthews, T. A., & Sandage, A. 1962, *PASP*, 74, 406, doi: [10.1086/127886](https://doi.org/10.1086/127886)
- Matthews, T. A., & Sandage, A. R. 1963, *ApJ*, 138, 30, doi: [10.1086/147615](https://doi.org/10.1086/147615)
- Merline, W. J., & Howell, S. B. 1995, *Experimental Astronomy*, 6, 163, doi: [10.1007/BF00421131](https://doi.org/10.1007/BF00421131)
- Misselt, K. A., Clayton, G. C., & Gordon, K. D. 1999, *ApJ*, 515, 128, doi: [10.1086/307010](https://doi.org/10.1086/307010)

- Molster, F. J., Waters, L. B. F. M., & Kemper, F. 2010, in *Lecture Notes in Physics*, Berlin Springer Verlag, ed. T. Henning, Vol. 815, 143–201, doi: [10.1007/978-3-642-13259-9_3](https://doi.org/10.1007/978-3-642-13259-9_3)
- Muzzin, A., Marchesini, D., Stefanon, M., et al. 2013, *ApJ*, 777, 18, doi: [10.1088/0004-637X/777/1/18](https://doi.org/10.1088/0004-637X/777/1/18)
- Myers, A. D., Palanque-Delabrouille, N., Prakash, A., et al. 2015, *ApJS*, 221, 27, doi: [10.1088/0067-0049/221/2/27](https://doi.org/10.1088/0067-0049/221/2/27)
- Netzer, H., & Trakhtenbrot, B. 2014, *MNRAS*, 438, 672, doi: [10.1093/mnras/stt2238](https://doi.org/10.1093/mnras/stt2238)
- Nikutta, R., Hunt-Walker, N., Nenkova, M., Ivezić, Ž., & Elitzur, M. 2014, *MNRAS*, 442, 3361, doi: [10.1093/mnras/stu1087](https://doi.org/10.1093/mnras/stu1087)
- Noterdaeme, P., Petitjean, P., Ledoux, C., & Srianand, R. 2009, *A&A*, 505, 1087, doi: [10.1051/0004-6361/200912768](https://doi.org/10.1051/0004-6361/200912768)
- Oke, J. B. 1963, *Nature*, 197, 1040, doi: [10.1038/1971040b0](https://doi.org/10.1038/1971040b0)
- Oke, J. B., & Schmidt, M. 1963, *AJ*, 68, 288, doi: [10.1086/109103](https://doi.org/10.1086/109103)
- Park, S. Q., Barmby, P., Willner, S. P., et al. 2010, *ApJ*, 717, 1181, doi: [10.1088/0004-637X/717/2/1181](https://doi.org/10.1088/0004-637X/717/2/1181)
- Pei, Y. C. 1992, *ApJ*, 395, 130, doi: [10.1086/171637](https://doi.org/10.1086/171637)
- Perlmutter, S., Aldering, G., Goldhaber, G., et al. 1999, *ApJ*, 517, 565, doi: [10.1086/307221](https://doi.org/10.1086/307221)
- Peterson, B. M. 1997, *An Introduction to Active Galactic Nuclei*
- Pettini, M., Smith, L. J., Hunstead, R. W., & King, D. L. 1994, *ApJ*, 426, 79, doi: [10.1086/174041](https://doi.org/10.1086/174041)
- Prevot, M. L., Lequeux, J., Maurice, E., Prevot, L., & Rocca-Volmerange, B. 1984, *A&A*, 132, 389
- Prochaska, J. X., Herbert-Fort, S., & Wolfe, A. M. 2005, *ApJ*, 635, 123, doi: [10.1086/497287](https://doi.org/10.1086/497287)
- Rauch, M. 1998, *ARA&A*, 36, 267, doi: [10.1146/annurev.astro.36.1.267](https://doi.org/10.1146/annurev.astro.36.1.267)
- Richards, G. T., Fan, X., Newberg, H. J., et al. 2002, *AJ*, 123, 2945, doi: [10.1086/340187](https://doi.org/10.1086/340187)
- Richards, G. T., Hall, P. B., Vanden Berk, D. E., et al. 2003, *AJ*, 126, 1131, doi: [10.1086/377014](https://doi.org/10.1086/377014)
- Richards, G. T., Lacy, M., Storrie-Lombardi, L. J., et al. 2006, *ApJS*, 166, 470, doi: [10.1086/506525](https://doi.org/10.1086/506525)
- Richards, G. T., Myers, A. D., Gray, A. G., et al. 2009, *ApJS*, 180, 67, doi: [10.1088/0067-0049/180/1/67](https://doi.org/10.1088/0067-0049/180/1/67)
- Riess, A. G., Filippenko, A. V., Challis, P., et al. 1998, *AJ*, 116, 1009, doi: [10.1086/300499](https://doi.org/10.1086/300499)
- Ross, N. P., Myers, A. D., Sheldon, E. S., et al. 2012, *ApJS*, 199, 3, doi: [10.1088/0067-0049/199/1/3](https://doi.org/10.1088/0067-0049/199/1/3)
- Roulston, B. R., Green, P. J., & Kesseli, A. Y. 2020, *ApJS*, 249, 34, doi: [10.3847/1538-4365/aba1e7](https://doi.org/10.3847/1538-4365/aba1e7)
- Ryle, M., & Vonberg, D. D. 1946, *Nature*, 158, 339, doi: [10.1038/158339b0](https://doi.org/10.1038/158339b0)
- Salpeter, E. E. 1964, *ApJ*, 140, 796, doi: [10.1086/147973](https://doi.org/10.1086/147973)

- Sandage, A. 1965, ApJ, 141, 1560, doi: [10.1086/148245](https://doi.org/10.1086/148245)
- Sanders, D. B., Soifer, B. T., Elias, J. H., Neugebauer, G., & Matthews, K. 1988, ApJ, 328, L35, doi: [10.1086/185155](https://doi.org/10.1086/185155)
- Sanders, D. B., Salvato, M., Aussel, H., et al. 2007, ApJS, 172, 86, doi: [10.1086/517885](https://doi.org/10.1086/517885)
- Sarangi, A., Matsuura, M., & Micelotta, E. R. 2018, Space Sci. Rev., 214, 63, doi: [10.1007/s11214-018-0492-7](https://doi.org/10.1007/s11214-018-0492-7)
- Savage, B. D., & Mathis, J. S. 1979, ARA&A, 17, 73, doi: [10.1146/annurev.aa.17.090179.000445](https://doi.org/10.1146/annurev.aa.17.090179.000445)
- Schmidt, M. 1963, Nature, 197, 1040, doi: [10.1038/1971040a0](https://doi.org/10.1038/1971040a0)
- Schmidt, M., & Green, R. F. 1983, ApJ, 269, 352, doi: [10.1086/161048](https://doi.org/10.1086/161048)
- Schmitt, H. R., Antonucci, R. R. J., Ulvestad, J. S., et al. 2001, ApJ, 555, 663, doi: [10.1086/321505](https://doi.org/10.1086/321505)
- Seaton, M. J. 1979, MNRAS, 187, 73, doi: [10.1093/mnras/187.1.73P](https://doi.org/10.1093/mnras/187.1.73P)
- Secrest, N. J., von Hausegger, S., Rameez, M., et al. 2021, ApJ, 908, L51, doi: [10.3847/2041-8213/abdd40](https://doi.org/10.3847/2041-8213/abdd40)
- Selsing, J., Fynbo, J. P. U., Christensen, L., & Krogager, J. K. 2016, A&A, 585, A87, doi: [10.1051/0004-6361/201527096](https://doi.org/10.1051/0004-6361/201527096)
- Siegel, R., & Howell, J. R. 1981, Thermal radiation heat transfer
- Skrutskie, M. F., Cutri, R. M., Stiening, R., et al. 2006, AJ, 131, 1163, doi: [10.1086/498708](https://doi.org/10.1086/498708)
- Somerville, R. S., Primack, J. R., & Faber, S. M. 2001, MNRAS, 320, 504, doi: [10.1046/j.1365-8711.2001.03975.x](https://doi.org/10.1046/j.1365-8711.2001.03975.x)
- Stern, D., Eisenhardt, P., Gorjian, V., et al. 2005, ApJ, 631, 163, doi: [10.1086/432523](https://doi.org/10.1086/432523)
- Stern, D., Assef, R. J., Benford, D. J., et al. 2012, ApJ, 753, 30, doi: [10.1088/0004-637X/753/1/30](https://doi.org/10.1088/0004-637X/753/1/30)
- STScI Development Team. 2018, synphot: Synthetic photometry using Astropy. <http://ascl.net/1811.001>
- Thorne, A. P., Litzen, U., & Johansson, S. 1999, Spectrophysics : principles and applications
- Trump, J. R., Hall, P. B., Reichard, T. A., et al. 2006, ApJS, 165, 1, doi: [10.1086/503834](https://doi.org/10.1086/503834)
- Trumpler, R. J. 1930a, PASP
- . 1930b, PASP
- Turnshek, D. A. 1984, ApJ, 280, 51, doi: [10.1086/161967](https://doi.org/10.1086/161967)
- Tytler, D., & Fan, X.-M. 1992, ApJS, 79, 1, doi: [10.1086/191642](https://doi.org/10.1086/191642)
- Urry, C. M., & Padovani, P. 1995, PASP, 107, 803, doi: [10.1086/133630](https://doi.org/10.1086/133630)

- Usher, P. D. 1978, ApJ, 222, 40, doi: [10.1086/156119](https://doi.org/10.1086/156119)
- Usher, P. D., & Mitchell, K. J. 1978, ApJ, 223, 1, doi: [10.1086/156230](https://doi.org/10.1086/156230)
- Vanden Berk, D. E., Richards, G. T., Bauer, A., et al. 2001, AJ, 122, 549, doi: [10.1086/321167](https://doi.org/10.1086/321167)
- Voit, G. M., Weymann, R. J., & Korista, K. T. 1993, ApJ, 413, 95, doi: [10.1086/172980](https://doi.org/10.1086/172980)
- Wang, F., Yang, J., Fan, X., et al. 2021, ApJ, 907, L1, doi: [10.3847/2041-8213/abd8c6](https://doi.org/10.3847/2041-8213/abd8c6)
- Wang, J.-G., Dong, X.-B., Wang, T.-G., et al. 2009, ApJ, 707, 1334, doi: [10.1088/0004-637X/707/2/1334](https://doi.org/10.1088/0004-637X/707/2/1334)
- Warren, S. J., Hewett, P. C., & Foltz, C. B. 2000, MNRAS, 312, 827, doi: [10.1046/j.1365-8711.2000.03206.x](https://doi.org/10.1046/j.1365-8711.2000.03206.x)
- Weymann, R. J., Carswell, R. F., & Smith, M. G. 1981, ARA&A, 19, 41, doi: [10.1146/annurev.aa.19.090181.000353](https://doi.org/10.1146/annurev.aa.19.090181.000353)
- Willott, C. J. 2005, ApJ, 627, L101, doi: [10.1086/432091](https://doi.org/10.1086/432091)
- Witt, A. N., Bohlin, R. C., & Stecher, T. P. 1984, ApJ, 279, 698, doi: [10.1086/161934](https://doi.org/10.1086/161934)
- Wolfe, A. M., Gawiser, E., & Prochaska, J. X. 2005, ARA&A, 43, 861, doi: [10.1146/annurev.astro.42.053102.133950](https://doi.org/10.1146/annurev.astro.42.053102.133950)
- Wolfe, A. M., Turnshek, D. A., Smith, H. E., & Cohen, R. D. 1986, ApJS, 61, 249, doi: [10.1086/191114](https://doi.org/10.1086/191114)
- Wolfire, M. G., McKee, C. F., Hollenbach, D., & Tielens, A. G. G. M. 2003, ApJ, 587, 278, doi: [10.1086/368016](https://doi.org/10.1086/368016)
- Wright, E. L., Eisenhardt, P. R. M., Mainzer, A. K., et al. 2010, AJ, 140, 1868, doi: [10.1088/0004-6256/140/6/1868](https://doi.org/10.1088/0004-6256/140/6/1868)
- Yang, J., Wang, F., Fan, X., et al. 2020, ApJ, 897, L14, doi: [10.3847/2041-8213/ab9c26](https://doi.org/10.3847/2041-8213/ab9c26)
- Yèche, C., Petitjean, P., Rich, J., et al. 2010, A&A, 523, A14, doi: [10.1051/0004-6361/200913508](https://doi.org/10.1051/0004-6361/200913508)
- Zakamska, N. L., Strauss, M. A., Krolik, J. H., et al. 2003, AJ, 126, 2125, doi: [10.1086/378610](https://doi.org/10.1086/378610)
- Zel'dovich, Y. B., & Novikov, I. D. 1967, Soviet Ast., 10, 602
- Zhu, Y., Becker, G. D., Bosman, S. E. I., et al. 2021, ApJ, 923, 223, doi: [10.3847/1538-4357/ac26c2](https://doi.org/10.3847/1538-4357/ac26c2)
- Zombeck, M. 2007, Handbook of Space Astronomy and Astrophysics: Third Edition